Fractional Order Cardiovascular System Model with Baroreflex Control - An Optimization Approach

A thesis submitted

in partial fulfillment for the award of the degree of

Doctor of Philosophy

by

Resmi V L

Department of Avionics

Indian Institute of Space Science and Technology

Thiruvananthapuram, India

January 2024

Certificate

This is to certify that the thesis titled ***Fractional Order Cardiovascular System Model with Baroreflex Control - An Optimization Approach*** submitted by **Resmi V L**, to the Indian Institute of Space Science and Technology, Thiruvananthapuram, in partial fulfillment for the award of the degree of **Doctor of Philosophy** is a bonafide record of the original work carried out by her under my supervision. The contents of this thesis, in full or in parts, have not been submitted to any other Institute or University for the award of any degree or diploma.

Dr. N. Selvaganesan
Supervisor
Professor and Head
Department of Avionics
IIST.

Place: Thiruvananthapuram
Date: January 2024

Declaration

I declare that this thesis titled ***Fractional Order Cardiovascular System Model with Baroreflex Control - An Optimization Approach*** submitted in partial fulfillment for the award of the degree of **Doctor of Philosophy** is a record of the original work carried out by me under the supervision of **Dr. N. Selvaganesan**, and has not formed the basis for the award of any degree, diploma, associateship, fellowship, or other titles in this or any other Institution or University of higher learning. In keeping with the ethical practice in reporting scientific information, due acknowledgments have been made wherever the findings of others have been cited.

Place: Thiruvananthapuram
Date: January 2024

Resmi V L
(SC19D003)

This thesis is dedicated to my beloved parents for their constant love and support. I love you both and I appreciate everything that you have done for me. I miss you, my dad.

Acknowledgements

The work presented in this thesis would not have been possible without my close association with many people. I take this opportunity to extend my sincere gratitude and appreciation to all those who made this Ph.D. thesis possible.

First and foremost, I would like to express my sincere gratitude towards my research supervisor ***Dr. N. Selvaganesan***, for giving me the opportunity to work under his guidance. I am very thankful to him for his continuous support, advice, motivation and guidance throughout my Ph.D. research in moulding me into a better researcher and also helping me to complete this project successfully. His technical and editorial advice is very important for the completion of this thesis.

I gratefully acknowledge the doctoral committee chairman, ***Dr. Deepak Mishra***, Professor, Department of Avionics, IIST and extend my sincere thanks to the other members of my doctoral committee ***Dr. Priyadarsanam***, Professor, Department of Avionics, IIST, ***Dr. Anup***, Associate Professor, Department of Avionics, IIST and ***Dr. N. Sabu***, Professor, Department of Mathematics, IIST for their periodic assessments of my research work.

I am also thankful to my institute, the especially Department of Avionics, for picking me up as a doctoral student and providing me an excellent research environment. I would like to express my sincere gratitude to all faculties and staff for their encouragement and continuous support.

It would be a great injustice if I do not acknowledge some great souls who have made my life in IIST as exciting as it was. First of all, a huge thanks to all the fellow Ph.D, Master and B.Tech students, whom I worked together. Interactions with you have always been knowledgeable and enjoyable. Special thanks to my senior Dr. P. Sathishkumar, Meera, Anjana, Anjitha and Sriya for for all the knowledgeable talks we had. A big thanks to my friends Gopika, Nikhil, Sriram, Chithra, Vijay, Krishnanunni, Abhijith, Ritwik, Pavanam, Prabith, Anjuna, Namitha, Shihas and James for making my life in IIST a memorable one and helping me in both academic and non-academic fields. No words can justify the love and support given by my friends Pramod, Sanketa and Pragya. A very special thanks to Renjith and Manu for listening to me when things got stressful and for being my food, travel and fun buddies. You have always been by my side, even during the difficult times.

I am extremely grateful to my parents for your lessons of perseverance, I thank you

with every cell in my body. Finally, I am eternally grateful to my dearest brother Nithin, my sister Remya and my brother-in-law for always been my pillars of support all my life.

-Resmi V L

Abstract

The Cardiovascular System (CVS) is an intricate and essential part of human physiology which maintains oxygen transport, blood flow and homeostasis throughout the body. Understanding the dynamics and regulation of the CVS is important in clinical medicine, biomedical research and healthcare innovation. Experimentation with the human body to understand physiology is a challenging research area in the modern world. The mechanisms postulated to explain the human system can be easily studied using mathematical expressions in computer simulation due to the extremely complex structure of the human system. These mathematical representations involve creating dynamical equations and computational simulations to describe the physiological process of the human system.

During the initial phase of the research work, a lumped parameter model for CVS is developed using the pressure voltage analogy. In the existing arterial Windkessel models, the viscoelasticity characteristics are not considered, leading to error in the model and hence false prediction is unavoidable. To incorporate this characteristic, improved Fractional Order (FO) Windkessel models are developed by introducing fractionality in the existing 2-element, 3-element and 4-element Windkessel models (Wk4). The MATLAB function fmincon() is used to optimize the model parameters and fractionality of the differential equation by minimizing the error between the clinical data and the model output considered as an objective function. The simulation results indicate that the FO models provide least error index than the existing Integer Order (IO) Windkessel models. In specific, the FO Wk4 model provides better closeness to the clinical data than other FO Windkessel models. Hence, FO Wk4 model is further used to study the behavior of system subjected to abnormalities like atherosclerosis and arterial stiffness.

The Windkessel model is a single compartment representation which simplifies the complex arterial system into a series of resistive and compliant elements, neglecting the intricate branching and geometry of the chambers and the valve functionality. A more complex model is required to address the limitations of Windkessel model for specific applications or studies which need better accuracy. Hence, a FO geometric model is presented which includes four chambers of the heart, systemic and pulmonary circulation. The heart chambers are modeled based on the geometry and systemic and pulmonary circulation are modeled using the Windkessel approach. To include the viscoelastic property, a fractionality is included in the dynamics of the chambers. An optimization method is presented to

obtain the fractionality of different chambers by minimizing the error index between clinical data of healthy human and model output using heuristic algorithms such as Cuckoo search, Firefly and Accelerated particle swarm optimization.

Baroreflex dysfunction is one of the common causes associated with the CVS. The buffering capability and baroreflex gain influence large variation in blood pressure for short term control. For regulating the blood pressure, a model with the baroreflex control is proposed to study the complex interactions between the autonomic nervous system and CVS. Initially, baroreflex control is designed for the IO extended windkessel model which handles the distribution of total blood volume changes under the influence of postural changes by means of short term baroreflex control utilizing the sympathetic and parasympathetic nerve activities. To show the efficiency of the proposed model, the simulation is carried out further for orthostatic hypotension and hypertension conditions. The existing IO model will not consider the viscoelastic property of CVS. Hence to get the realistic anatomy and better accuracy, the baroreflex control is designed for the proposed FO geometric model and validated with clinical data. Also, the proposed model is studied for different abnormality conditions like orthostatic intolerance, hemorrhage, atherosclerosis and arterial stiffness.

Contents

List of Figures

List of Tables

List of Algorithms

Abbreviations

ANS	Autonomic Nervous System
APSO	Accelerated Particle Swarm Optimization
AV	Aortic Valve
CS	Cuckoo Search
CVS	Cardiovascular System
FA	Firefly Algorithm
FO	Fractional Order
HR	Heart Rate
IO	Integer Order
ISE	Integral Square Error
LA	Left Atrium
LV	Left Ventricle
MAP	Mean Arterial Pressure
MV	Mitral Valve
OI	Orthostatic Intolerence
PV	Pulmonary Valve
RA	Right Atrium
RV	Right Ventricle
TV	Tricuspid Valve

Nomenclature

J^n	$n-$fold Integration
$\mathbb{R}^+, \mathbb{R}_{>0}$	Set of Positive Real Numbers
J^α_{RL}	Riemann-Liouville Fractional Integral
$\Gamma(\alpha)$	Gamma Function
D^n	n^{th} Order Derivative
D^α_{RL}	Riemann-Liouville Fractional Derivative
$\mathbb{N}$	Set of Natural Numbers
D^α_C	Caputo Fractional Derivative
D^α_{GL}	Grunwald-Letnikov derivative
J^α_{GL}	Grunwald-Letnikov Integral
$\mathbb{R}$	Set of Real Numbers
$\mathcal{L}\{\cdot\}$	Laplace Transform
$f^{(k)}(t)$	k^{th} Derivative of $f(t)$
τ_H	Time constant for heart rate
τ_{C_v}	Time constant for compliance of veins
τ_c	Time constant for contractility of heart
τ_R	Time constant for Resistance
$\tau_{V_{str}}$	Time constant for stroke volume
$\tau_{E_{rv}}$	Time constant for elastance of right ventricle
$\tau_{E_{lv}}$	Time constant for elastance of left ventricle
α_H	Constant for sympathetic tone for heart rate
β_H	Constant for parasympathetic tone for heart rate
β_{C_v}	Constant for parasympathetic tone compliance of veins
α_c	Constant for sympathetic tone for contractility of heart
α_R	Constant for sympathetic tone for Resistance
$\alpha_{V_{str}}$	Constant for sympathetic tone for stroke volume
$\alpha_{E_{rv}}$	Constant for sympathetic tone for elastance of right ventricle

Chapter 1

Introduction

1.1 Introduction

Experimentation with human system is one of the challenging research areas in the modern world. The mechanisms postulated to explain human system can be easily studied with the use of computer simulations due to the extremely complex model of the human system. For example, when the astronauts have to fly from high-g to zero-g and vice versa, they have to encounter various problems like dizziness, lightheadedness, diaphoresis, nausea, visual disturbances etc,. For analyzing these issues, direct experimentation in human system may lead to serious health consequences. In this scenario, modeling and simulation of biological systems is important and it plays a vital role. These mathematical models can be used to detect diseases in the early stage itself.

1.2 Literature Survey

Human system is a highly complex system that performs complex functions and needs immense knowledge in this area to understand the behavior. Doing experimentation in the human system to study the complex working and interaction of the different systems inside the human body is difficult. The complex behavior can be studied with the help of mathematical modeling and computer simulations that mimic the behavior of human system. Like other systems in human body, Cardiovascular System (CVS) is unique for its complex, dispersed anatomical structure, physical properties and dynamic activity.

Heart disease is the main cause of death worldwide. Such diseases can be diagnosed and treated using various forms, like following diets which is a simplest method to very complex and high risk such as heart transplantation. Due to their important roles in pump-

ing blood into the circulation system, heart models have been paid more attention. Modern engineering technology is allowing opportunities to find improved technologies for diagnosis and prevention of such diseases which are considered as dreadful diseases in the olden days. New medical assist devices or predictive medical instruments can help to get awareness of the risky situations to occur in due time to our health. To realize such goals, various mathematical modeling of human heart has been studied using physical models.

For representing CVS, the electrical analogy of CVS is used. To explain the arterial pressure decay during diastole, a single lumped Windkessel model is developed which gives a mathematical description of the arterial system. In [1], authors developed a model which improves the characteristics at high frequency by placing a resistance in series with the 2-element Windkessel model (Wk2) and known as the 3-element Windkessel model (Wk3). This provides a better pressure profile compared to Wk2. However, the parameters estimated do not match the values derived using Poiseuille's law [5]. To overcome this issue, an inductor is introduced to represent the inertia of the blood flow [6]. There are two ways of including the inductor (i) parallel to the series resistance [7] and (ii) series with resistance [8]. Due to physiological interpretation, an inductor in series with resistance is widely used and named as 4-element Windkessel model (Wk4) [2]. The performance of these models are analyzed by fitting the pressure profile with data collected from healthy subjects of different age groups [9]. The estimated model parameters are compared with the theoretical values and found that the Windkessel model with series inertance performs better than other models.

To get better performance, more characteristics need to be added which make the model complex. In [10], Wk4 is extended by adding diodes as valves. Over the years, circuit modeling become complex since the models developed are the combination of many lumped segments. The level of complexity further increases with the introduction of complex control loops. As the computer era started, the complexity in analyzing the mathematical model in simulation platform is dramatically reduced [11].

On the other hand, distributed parameter models are used for representing the blood flow relations using the Navier-Stokes equation [12]. However, lumped parameter models are commonly used in literature due to their simple representation and easy analysis. In [13], the mitral valve and tricuspid valves are modeled using resistors that vary with the pressure gradient across them. This assures unidirectional flow and can be further used for disease diagnosis. In order to simulate the CVS including the baroreceptor model, a mathematical and physical analogy model of the total artificial heart is developed [14]. From the literature, it is noted that a complete heart model is obtained by adding all four chambers

and valves. The complete artery structure of the CVS along with the pulmonary circulation is modeled which is complex and hence difficult to analyze [2], [12]. The control mechanism to regulate the blood pressure of the artery also be included to get a realizable model.

The rhythmic contraction and relaxation of the cardiac muscles eject blood from the Left Ventricle (LV) and the pressure exerted by the blood on the wall of arteries is known as Mean Arterial Pressure (MAP). This is influenced by four key factors (i) cardiac output (ii) blood volume (iii) peripheral resistance and (iv) viscosity [15]. The sudden variation in MAP can lead to the dysfunction of the different body parts and organs. On changing the position from supine to standing, blood pools towards the lower body due to gravity, which changes the distribution of the blood volume in the body, leading to change in venous pressure. The Baroreceptors fire action and this information is processed in the medulla oblongata and its cardioinhibitory and vasomotor centers then create sympathetic and parasympathetic nerve activities respectively [16]. The efferent pathways transmit these activities in the form of impulses to the various parts of the CVS which affects the blood pressure by changing the peripheral resistance, compliance, stroke volume and contractility. Hence baroreceptor control plays an important role in modeling of CVS [16].

A model of the heart including ventricular pressure as a function of change in heart rate is given in [17]. In [18] and [19], heart rate data is directly given to the model and does not include the cardio-pulmonary circuit. These models use sigmoidal relationships for the control parameters with respect to the pressure and use differential equations similar to [20]. The heart models along with the baroreflex mechanism presented in [21] use non-pulsatile (linear) models whereas [19] and [20] deal with pulsatile model (non-linear). When compared with the experimental data, the nonlinear model provides better result than the linear model. In [22], change in heart rate is modeled, however other parameters like peripheral resistance, contractility, compliance and stroke volume are not taken into consideration. However, this model does not include the cardio-pulmonary circuit which leads to inaccuracy.

In [23], 0D-3D model combination is used to analyze the baroreflex control, but the effect of the pulmonary circuit and right heart is not taken into consideration. The effect of respiration is considered in [24], but instead of compartment modeling, the systolic and diastolic phase modeling approach is used. The parameters used in the models are predicted using experimental or optimization methods. Kalman filtering method can also be used for the prediction of parameters in the modeling of baroreflex control [25]. The mechanisms of baroreflex are extensively studied through experimental procedures on animals and found

nonlinear behavior of the control mechanisms [26] - [27]. The statistical analysis of the data has been done to analyze the relation between heartbeat and pressure due to the head up tilt position and postural changes [28] - [29].

Orthostatic Intolerance (OI) is common in elderly and post flight in astronauts and is hard to diagnose and treat [30] - [31]. The ability of the CVS to regulate the blood pressure (i.e. baroreceptor mechanism) will be compromised after the return from microgravity conditions for astronauts. During space travel, the loss of hydrostatic force due to microgravity causes reduction in intravascular volume. To understand the diagnosis and treatment, it is crucial to study the underlying mechanism of short-term blood pressure management. This is aided by pressure sensors called baroreceptors found in the walls of major arteries in the thorax and neck [32]. Experimentation with human body is difficult and is done in controlled conditions [33]. Studies show that after returning from space, astronauts are provided with medical assistance in the ground station to avoid the problems related to OI [34]. The effect of microgravity conditions can be mathematically modeled and studied by altering the baroreceptor control mechanism which can be used to analyze health of astronauts [35].

Fractional Order (FO) calculus is a generalization of classical calculus that extends the concept of differentiation and integration to non-integer orders. In the real-world problem, processes exhibit non-integer order behavior that cannot be captured using traditional Integer Order (IO) calculus. Hence, FO calculus can be used to model complex systems more accurately. Fractional calculus has gained increasing attention in recent years for its potential to provide more accurate and flexible mathematical models of physical systems. One of the significant contributions of FO in modeling is its ability to capture the complex dynamics of physical systems that cannot be described by IO models. In many fields of science and engineering, researchers have used FO models to improve the accuracy of their predictions. In [36], a study on the behavior of a mass-spring system subjected to a FO damping force is presented, which uses a novel approach to accelerate the system's response by introducing an external force expressed using FO that acts on the system's mass. The introduced external force allows the system to overcome the damping effect and reach a steady-state response more quickly.

Fractional calculus has also been used in the modeling of biological systems. A recent study has proposed a mathematical model for simulating the behavior of the human liver using the Caputo-Fabrizio fractional derivative to describe the memory effects of the liver's behavior [37]. The viscoelasticity of the arterial wall is one of the important factors which controls the pressure-flow relation of the arterial system. This property is incorpo-

rated in the Windkessel models by introducing fractionality to the capacitor. A two-stage algorithm based on modulating functions is used for the parameter estimation and validated using clinical data [38]. This indicates that transitions between viscosity and elasticity are modeled accurately. In [39], FO derivatives in the lumped circulation models are used for diagnosing different types of heart abnormalities using pressure-volume loops. In [40], the arterial stiffness is analyzed using the FO based paradigm of arterial compliance.

Many studies over the last decade show the feasibility of adopting fractional modeling to represent artery wall viscoelasticity [41]. FO viscoelastic models for one-dimensional blood flow are presented in [42]. The viscoelasticity of the arterial wall is one of the important factors that control the arterial system's pressure-flow relation. This property is incorporated in the Windkessel models by introducing fractionality to the capacitor. The importance of the FO Windkessel model lies in its ability to capture the complex dynamics of the arterial system, which cannot be fully explained by the classical model. The arterial system exhibits viscoelastic and nonlinear behavior which can account more accurately using FO Windkessel models than IO models. This makes it a valuable tool for studying the pathophysiology of various cardiovascular diseases such as hypertension, atherosclerosis etc., and for designing interventions/treatments for these diseases. Studies show that fractionality is introduced to Wk3 model [43]. However, the effect of inertance of the flow of blood and the effect of diseased conditions are not modeled. Its potential applications in medical device development and non-invasive diagnostics further emphasize its importance.

Different methods like Oustaloop approximation, Charef method, etc., are used to approximate FO systems for simulation [44]. Adams-Bashforth-Moulton predictor-corrector method is widely used for numerical solution of FO systems [45]. The basic Windkessel model is used for these FO models which only considers the arterial model of CVS. FO approach is introduced to a cardiovascular circulatory system and left carotid model which includes the left atrium, left ventricle and aorta [46]. Determining the FO of a model is an important step when dealing with systems that exhibit non-integer order dynamics.

Several methods and techniques can be employed to find the fractionality of a model. One of the common methods is to fit experimental data to a FO transfer function model in which fractionality is obtained by adjusting the FO and other model parameters, the best fit to the real-world data can be obtained [47]. The slope of the Bode plot in the low-frequency region can be an indicative of FO system representation [48]. Hence, the order of fractional dynamical equation are obtained by analyzing the frequency response of a system. Similarly, the step response of a system can also help in determining the FO by receiving the

the rate at which the system approaches a steady state response. Other methods like least squares fitting, system identification techniques, recursive identification, machine learning and data driven approaches are also available and used in real time systems like induction motor, magnetic levitation, inverted pendulum [49], [50], [51].

In practice, most of the real time control problems cannot be solved analytically and hence, optimization techniques are widely applied. A wide range of optimization techniques exist like traditional and constrained optimization. Many of literature shows that the fmincon() solver in MATLAB which includes sequential quadratic programming, interior point etc,. are used for solving optimization problems [52]. The traditional optimization fails when dealing with complex systems, systems in which mathematical modeling is difficult and models which have large datasets. Hence, the optimization problems can be solved only using heuristic algorithms.

Heuristic optimization methods have gained popularity due to their ability to efficiently find near-optimal solutions for complex problems, especially in cases where traditional mathematical optimization techniques may be impractical or computationally expensive. Unlike some traditional optimization techniques that rely on derivatives of the objective function, heuristic methods do not require derivatives. This makes them suitable for problems where derivatives are difficult to obtain or are not available. Nature-inspired metaheuristic algorithms like Particle Swarm Optimization (PSO) [53], Genetic Algorithm (GA), Cuckoo Search (CS), ant colony optimization, Firefly Algorithm (FA) [4], honey bee mating optimization, Accelerated Particle Swarm Optimization (APSO), artificial bee colony algorithm, etc., are introduced to find the optimal parameters of the system model. Later different modifications are introduced to improve the accuracy and convergence of these algorithms [54]. The intelligent optimization method for designing FO controller based on GA is presented in [55]. Hence, heuristic optimization can be used to find the fractionality of the complex optimization problem of CVS model.

1.3 Motivation

The above literature show that the issues related to human system can be easily analyzed with the help of mathematical model and in turn helps in avoiding the risk caused. Mathematical modeling of the CVS holds significant importance for various aspects of medical research, clinical practices and healthcare innovation. Mathematical models help in understanding physiology, clinical decision support, risk assessment, surgical planning etc., in a cost effective manner. Many physical systems exhibit behaviors that cannot be accurately

represented by IO models. FO models, with their ability to capture non-integer order dynamics, can better represent the behavior of these systems. For CVS model, the viscoelastic property is ignored while modeling using IO approach. The FO modeling can incorporate the viscoelastic property and memory dependent characteristic.

Also, the modeling is not complete without adding the control loop to the system. Hence, a perfect model with an accurate baroreflex control is important for the easy analysis of human health. This motivates to propose FO models with baroreflex control which mimics the CVS and further can be useful for analysing the abnormalities.

1.4 Research Contributions

Overall, this research work presents the modeling of CVS using (i) FO Windkessel and (ii) FO geometric model with baroreflex control. The obtained CVS model using optimization methods is further studied for various abnormality conditions. The research contributions of the thesis are summarized as follows:

- A partial CVS model along with baroreflex is developed using the extended IO Windkessel model. This is validated for normal and postural change conditions. Further, the simulation is performed for OI conditions
- FO Windkessel and FO geometric models are developed and fractionalities are obtained using heuristic optimization methods like CS, FA and APSO algorithms. The proposed models are validated and studied in detail by introducing different abnormality conditions
- Baroreflex control mechanism is developed for the proposed FO geometric CVS model. To validate the model, simulation is conducted for (i) normal (ii) postural changes and (iii) various abnormality conditions

1.5 Organisation of Thesis

- Chapter 2 discusses the anatomy of heart and the mathematical models of CVS which includes Windkessel and geometrical model
- In Chapter 3, the detailed description about baroreflex control for CVS is given which includes a simplified extended IO Windkessel model. Simulations are done for postural changes and OI to show the performance of baroreflex control

- Chapter 4 presents the FO modeling of Windkessel and geometric model using different heuristic optimisation techniques like CS, FA and APSO
- Chapter 5 presents the integrated design which consistS of baroreceptor control mechanism and the FO geometric model
- Chapter 6 provide the conclusion and future directions of this research work

Chapter 2

Modeling of CVS

2.1 Introduction

Mathematical modeling involves using mathematical equations and computational techniques to simulate and analyze the behavior of CVS to understand the complex interactions between the various components such as the heart, blood vessels and blood flow. CVS is a highly dynamic and intricate system and mathematical modeling provides a quantitative framework to investigate its physiological processes. There are many different modeling methods available. One common approach is to model CVS as a network of interconnected compartments, representing different anatomical regions or physiological components. For example, the heart can be represented by a set of differential equations that describe its electrical activity and mechanical pumping function. The blood vessels can be represented as a network of resistances and capacitances that determine blood flow and pressure distribution. Other methods like modeling based on Navier Stokes equation and partial differential equations are also available. For this study, Windkessel model and geometric model are considered. To model the behavior of heart and its interaction with the blood vessels, it is important to know the anatomy and physiological theories behind the mechanisms. In this chapter a brief description about the anatomy and physiology of the heart and circulation system is provided.

2.2 Anatomy of CVS

CVS is a system that circulates blood through vessels between the heart and different parts of the body, carrying nutrients and oxygen to tissues and removing carbon dioxide and other wastes from the tissues. CVS mainly consists of the heart and circulation. The

heart includes four chambers and four valves and the circulation includes pulmonary and systemic vasculature which consists of arteries, veins and capillaries as shown in Figure 2.1.

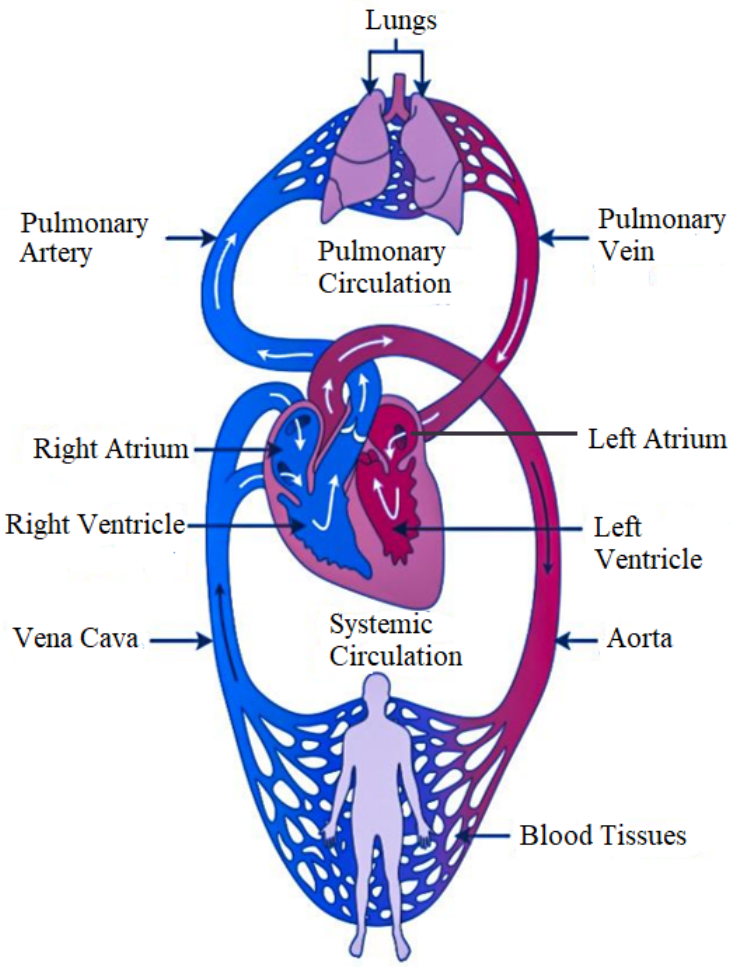

Figure 2.1: Schematic of CVS [1]

The primary function of the heart is to serve as a muscular pump propelling blood through vessels to and from all parts of the body. The pressure and velocity of the arteries which receive blood from heart is high and have thick walls that are composed of elastic fibrous tissue and muscle cell. The arterial tree terminates in short, narrow, muscular vessels called arterioles, from which blood enters simple endothelial tubes known as capillaries. These thin microscopic capillaries are permeable to vital cellular nutrients and waste products that they receive and distribute. From the capillaries, the deoxygenated

[1] https://www.vedantu.com/question-sets/7563f5e3-60cc-4d37-97c6-a8421820106b8206685272555919929.png

blood with impurities moves more slowly and under low pressure to vessels called venules that converge to form veins and guide the blood back to the heart.

Figure 2.2 shows the block diagram of different compartments of CVS and the flow of blood. This consists of (i) heart (ii) systemic and (iii) pulmonary circulation.

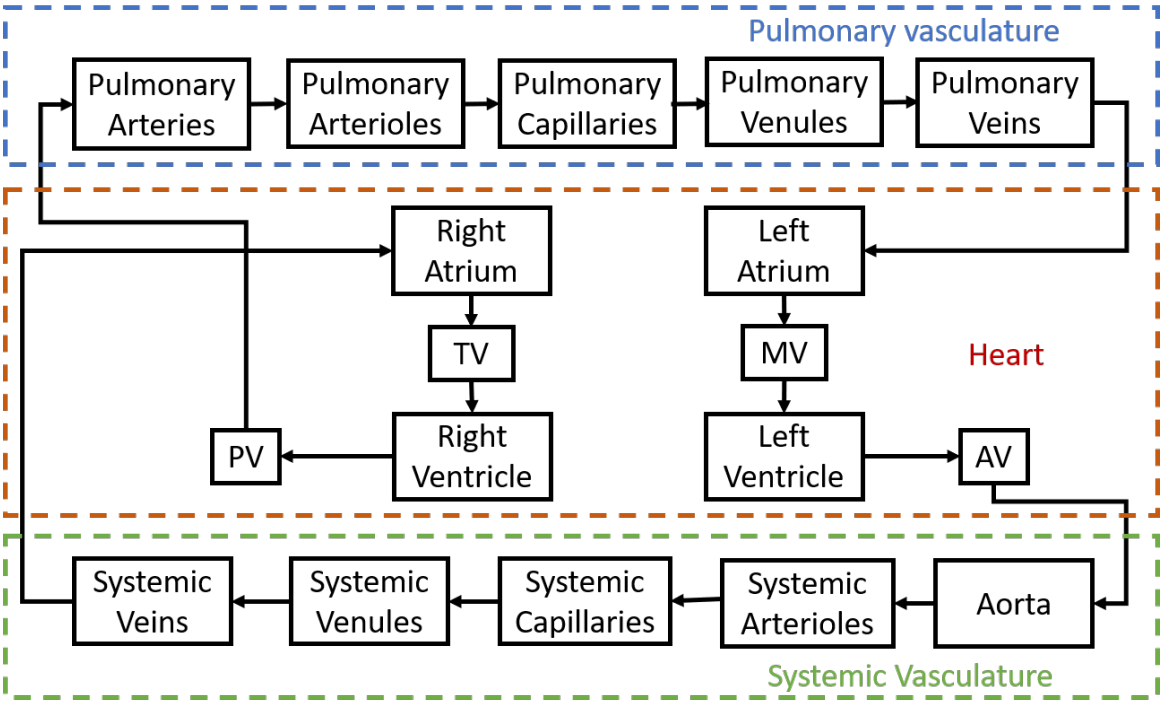

Figure 2.2: Compartmental representation of CVS

2.2.1 Heart

The heart is made up of cardiac muscle cells. It consists of four chambers Left Ventricle (LV), Left Atrium (LA), Right Atrium (RA) and Right Ventricle (RV). The blood flow between these chambers are controlled by four valves namely Mitral Valve (MV), Tricuspid Valve (TV), Pulmonary Valve (PV) and Aortic Valve(AV) as shown in Figure 2.3. They allow one-directional flow of blood in the chambers.

The RA and LA are the higher chambers and the RV and LV are the lower chambers. The septum is a wall that separates the right and left atria as well as the right and left ventricles. The largest chamber is the LV. It transports oxygen rich blood from the pulmonary veins to the body via the aorta. The RV receives the deoxygenated blood from the veins. Deoxygenated blood enters the RA through superior and inferior vena cava and the TV allows the flow only into the RV, from where the blood is directed by the pulmonary valve

towards lungs for purification via pulmonary arteries. The oxygenated blood then enters the LA through pulmonary veins from the lungs and the MV directs the blood into the LV, from where the blood is pumped via aorta regulated by AV.

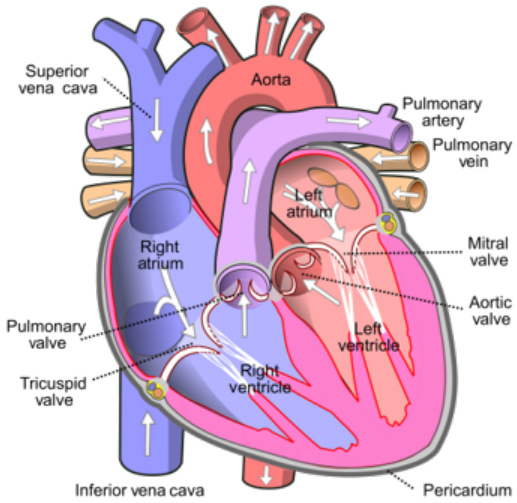

Figure 2.3: Schematic of Heart [2]

2.2.2 Circulation

Blood is carried from the heart to the rest of the body and back to the heart via a complex network of arteries, arterioles and capillaries, venules and veins and comes back to the heart is known as systemic circulation. Systemic vasculature consists of the aorta, systemic arterioles, systemic capillaries, systemic venules and systemic veins. Aorta carries oxygenated blood to the different part of the body and the deoxygenated blood reach RA through systemic veins. The oxygenated blood is pumped by LV of the heart via aorta and is distributed throughout the body via arteries. Further, blood percolates into the tissues via capillaries, which are branches of arteries, where the body cells use oxygen and nutrients. The deoxygenated blood received from different parts of the body is given to the RV of the heart is purified by the lungs and given back to the LA of the heart through the pulmonary circulation. The pulmonary vasculature consists of pulmonary arteries, arterioles, capillaries, venules and veins. Pulmonary arteries carry impure blood from RV to pulmonary arterioles of the lungs and the oxygenated blood returns to LA through pulmonary veins.

[2] https://www.vedantu.com/question-answer/blood-vessels-are-attached-to-the-heart-are-class-10-biology-cbse-5f62c960bc188a784311250b

2.3 Windkessel Models

The Windkessel model is the basic mathematical model that describes the behavior of the cardiovascular arterial system in specific the arterial circulation. The model consists of a simple electrical circuit that represents the arterial system as a hydraulic network as shown in Figure 2.4. The circuit consists of a capacitor which represents the compliance or elasticity of the arteries and a resistor which represents the resistance of the arterial system.

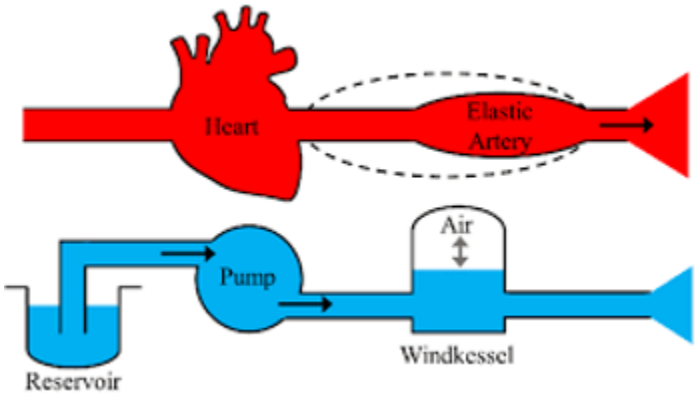

Figure 2.4: Hydraulic analogy of arterial system [3]

In Windkessel models, the heart pumps blood into the arterial system during systole causing the arterial pressure to rise. During diastole, when the heart is relaxed, the pressure falls as blood flows through the arterial system and into the smaller vessels. The capacitor in the circuit represents the ability of the arteries to store energy during systole and release it during diastole, which helps to maintain a relatively constant blood flow. The resistor represents the resistance offered by the arterial system to blood flow which is determined by factors such as the diameter of the blood vessels, their length and the viscosity of the blood. The mathematical modeling of the arterial system is based on the lumped parameter approach in which the pressure-volume relationships are analytically represented in the form of an ordinary differential equation.

2.3.1 2-element Windkessel model

In Wk2 model, the relation between pressure and flow rate can be represented using an IO differential equation obtained from the electrical circuit given in Figure 2.5. In this

[3] https://www.google.com/gasearch?q=Windkessel%20Effect&source=sh/x/gs/m2/5vhid=qdyFIngaVhkD_M&vssid=l

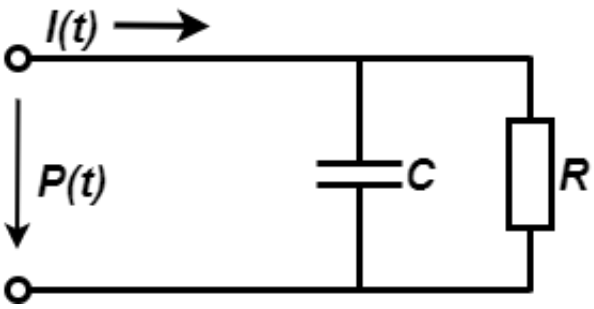

Figure 2.5: Circuit diagram of Wk2 model [1]

figure, the voltage represents pressure inside the artery and the current represents the flow rate of blood through the artery. The circuit resistance corresponds to resistance of the blood flow and the capacitor corresponds to compliance of the arterial system. By applying Kirchhoff's law:

$$I(t) = C\frac{dP(t)}{dt} + \frac{P(t)}{R} \tag{2.1}$$

where, $P(t)$ is the blood pressure in the aorta in mmHg, $I(t)$ is the flow rate, modeled as a time-varying current source, R is the peripheral resistance of aorta to the flow of blood in $mmHgs/cm^3$ and C is the compliance in $cm^3/mmHg$.
From (2.1), the change in pressure of WK2 is written as:

$$\frac{dP(t)}{dt} = \frac{1}{C}\left(I(t) - \frac{P(t)}{R}\right) \tag{2.2}$$

2.3.2 3-element Windkessel model

To include the resistance offered by the aortic valve to the blood flow, Wk3 is introduced which includes the impedance of the aortic valve (r) in series with the Wk2 model as shown in Figure 2.6.

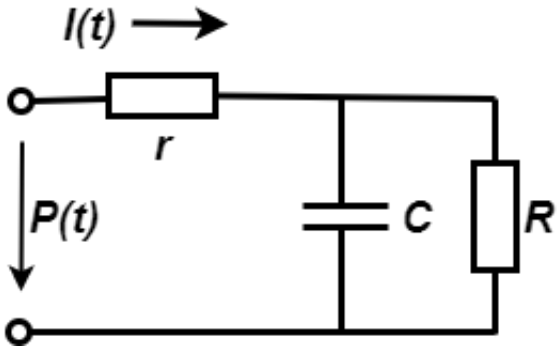

Figure 2.6: Circuit diagram of Wk3 model [1]

By applying Kirchhoff's law:

$$I(t) = C\frac{d}{dt}(P(t) - I(t)r) + \frac{P(t) - I(t)r}{R} \tag{2.3}$$

By rearranging (2.3):

$$I(t)\left(1 + \frac{r}{R}\right) = C\frac{dP(t)}{dt} - Cr\frac{dI(t)}{dt} + \frac{P(t)}{R} \tag{2.4}$$

Hence, the change in pressure for Wk3 is given as:

$$\frac{dP(t)}{dt} = \frac{1}{C}\left[\left(1 + \frac{r}{R}\right)I(t) + Cr\frac{dI(t)}{dt} - \frac{P(t)}{R}\right] \tag{2.5}$$

2.3.3 4-element Windkessel model

The effect of inertia on the blood flow through the blood vessel is not included in Wk2 and Wk3. Hence, Wk4 model is developed in which the total arterial inertance is added as the fourth element [6]. Here, an inductor (L) is added in series to the circuit in an account of inertia as shown in Figure 2.7. This model provides an accurate representation of the

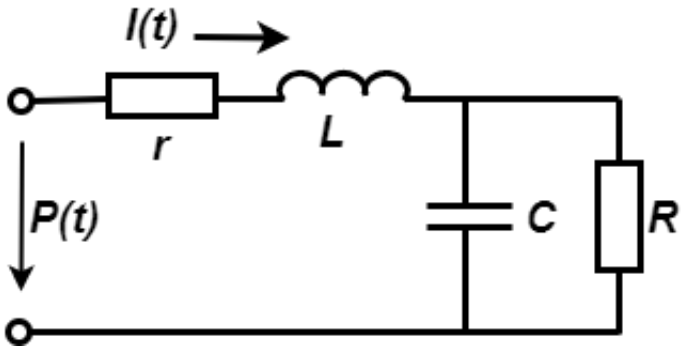

Figure 2.7: Circuit diagram of Wk4 model [1]

arterial blood flow when compared to Wk2 and Wk3. By applying Kirchhoff 's Law:

$$I(t) = C\frac{d}{dt}\left(P(t) - I(t)r - L\frac{dI(t)}{dt}\right) + \frac{P(t) - I(t)r - L\frac{dI(t)}{dt}}{R} \tag{2.6}$$

By rearranging (2.6):

$$I(t)\left(1 + \frac{r}{R}\right) = C\frac{dP(t)}{dt} - \left(Cr + \frac{L}{R}\right)\frac{dI(t)}{dt} - LC\frac{d^2I(t)}{dt^2} + \frac{P(t)}{R} \tag{2.7}$$

Hence, the change in pressure for Wk4 is obtained as:

$$\frac{dP(t)}{dt} = \frac{1}{C}\left[\left(1+\frac{r}{R}\right)I(t) + \left(Cr+\frac{L}{R}\right)\frac{dI(t)}{dt} + LC\frac{d^2I(t)}{dt^2} - \frac{P(t)}{R}\right] \tag{2.8}$$

The equations (2.2), (2.5) and (2.8) are used for generating the pressure profile of the Windkessel models.

2.4 Geometrical Model

Windkessel model includes only the arterial part of the CVS with which acquiring complete information of the system is not possible. The compartment model of CVS is a simplified representation that divides the system into discrete compartments, each representing a specific region or component of the CVS. This model is widely used in cardiovascular physiology to analyze and understand the dynamics of blood flow, pressure, and other relevant variables. In the compartment model, the CVS is divided into several interconnected compartments, and the flow of blood between these compartments is described using mathematical equations. Each compartment represents a specific anatomical or physiological region, such as the heart, arteries, veins, or capillaries. The connections between the compartments represent the blood vessels and their interactions. These connections can be modeled using resistances which determine the resistance of blood flow between compartments and capacitances which represent the ability of blood vessels to store and release blood.

In this model, the heart chambers are modeled based on the geometry and the valves are modeled analogous to diodes [3]. The systemic and pulmonary vasculature are modeled based on the arterial Windkessel model. All the chambers are included along with pulmonary and systemic lumped parameter models.

2.4.1 Modeling of heart

The four chambers of the heart LV, LA, RA and RV are modeled based on geometry. The geometry of LV and RV are shown in Figure 2.8. It is assumed that the geometry of RV is larger and more complicated compared to LV. Ellipsoidal shape and a lobulated cross-section with a triangular side view are used for representing the LV and RV of the heart respectively.

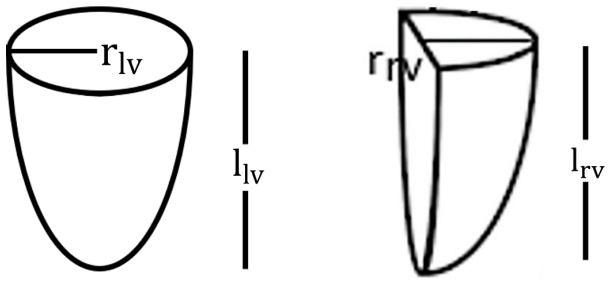

Figure 2.8: Geometry of LV and RV

2.4.1.1 LV modeling

The mathematical model describes the relationship between the pressure and radius in the heart chambers. Left ventricular geometry resembles a truncated ellipsoid [3] and hence, an ellipsoidal geometry is used for the modeling of LV. The LV volume (V_{lv}) is expressed using the LV radius (r_{lv}), long axis length (l_{lv}) and an additional coefficient (K_{lv}) which allows to include effects of the contraction in the long axis and scales the proportion between the LV radius and volume over a cardiac cycle. It is expressed as:

$$V_{lv} = K_{lv} \frac{\frac{4}{3}\pi r_{lv}^2 l_{lv}}{2} \tag{2.9}$$

The radius (r_{lv}) will be changing over a cycle, where as the long axis length remains the same. The change in radius is given by:

$$\frac{dr_{lv}}{dt} = \frac{3\frac{dV_{lv}}{dt}}{4\pi K_{lv} l_{lv}} \left(\frac{6V_{lv}}{4\pi K_{lv} l_{lv}} \right)^{-\frac{1}{2}} \tag{2.10}$$

The rate of change in volume is the change in the flow rate which is given by, $Q_{mv} - Q_{av}$. Hence, by using the relation between the radius and volume bounded by the ellipsoid, the change in radius of LV is expressed as:

$$\frac{dr_{lv}}{dt} = \frac{3(Q_{mv} - Q_{av})}{4\pi K_{lv} l_{lv}} \left(\frac{6V_{lv}}{4\pi K_{lv} l_{lv}} \right)^{-\frac{1}{2}} \tag{2.11}$$

where, (i) r_{lv}, l_{lv} and V_{lv} are the radius, length and volume of LV respectively (ii) K_{lv} is the constant which incorporates contraction along the long axis and (iii) Q_{mv} and Q_{av} are flowrates of MV and AV respectively.

When the volume and flow rate change, the radius of the chambers changes which in turn changes the pressure inside the chambers. The pressure inside the chambers are the

sum of active and passive pressures. The relation between pressure and radius of LV is expressed as:

$$\begin{aligned} P_{lv}(t) = E_{es-lv}\left[\frac{2}{3}\pi K_{lv} l_{lv}\left(r_{lv}^2 - r_{lv-0}^2\right)\right] f_{act-lv}(t) \\ + \left[\left(Ae^{\frac{1}{6}B\pi K_{lv} r_{lv}(t)^2 l_{lv}}\right) - 1\right] \end{aligned} \tag{2.12}$$

where, (i) E_{es-lv} is the end systolic elastance (ii) r_{lv-0} is the radius at zero pressure of LV (iii) f_{act-lv} is the cosine activation function for LV and (iv) A and B are constants.

The activation function f_{act-lv} generates a bell-shaped curve that varies between 0 and 1. The activation function f_{act} is selected such that the mathematical description of the ventricle agrees with actual measured isovolumic ventricular pressure for different volumes. There are different types of activation functions are available in literature like Mulier's method, polynomial function, gamma distribution function, combined Exponential, Hill function, cosine function, sine function etc. For the geometrical model, the cosine function is used and is given as [17]:

$$f_{act,lv}(t) = \begin{cases} \frac{1-cos(t/T_1)\pi}{2} & 0 \le t \le T_1 \\ \frac{1+cos((t-T_1)/(T_2-T_1)\pi)}{2} & T_1 \le t \le T_2 \\ 0 & T_2 \le t \le T \end{cases} \tag{2.13}$$

where, t is the time over a cardiac cycle, T_1, T_2, and T are the times at the end of systole, end of the ventricular relaxation and duration of the cardiac cycle.

2.4.1.2 RV modeling

RV has a more complex shape with respect to LV and resembles a crescentic cross-section and a triangle from the side view. The crescentic cross-section of the RV is more extensive with respect to the circular cross-section of the LV and the triangular side view of RV seems like an ellipsoid which has a larger volume occupied by LV. Therefore, an ellipsoidal volume trimmed at the long axis and the basal axis of RV provides a quite good approximation to model the RV volume and is given by:

$$V_{rv} = K_{rv}\frac{\frac{4}{3}\pi r_{rv}^2 l_{rv}}{4} \tag{2.14}$$

Similarly the change in radius of RV is expressed as:

$$\frac{dr_{rv}}{dt} = \frac{3(Q_{tv} - Q_{pv})}{2\pi K_{rv} l_{rv}} \left(\frac{3V_{rv}}{\pi K_{rv} l_{rv}} \right)^{-\frac{1}{2}} \tag{2.15}$$

where, (i) r_{rv}, l_{rv} and V_{rv} are the radius, length and volume of RV respectively (ii) K_{rv} is the constant account for the contraction along the long axis of RV and (iii) Q_{tv} and Q_{pv} are flowrates of TV and PV respectively.

The relation between pressure and radius of RV is expressed as:

$$\begin{aligned} P_{rv}(t) = E_{es-rv} \left[\frac{1}{3} \pi K_{rv} l_{rv} \left(r_{rv}^2 - r_{rv-0}^2 \right) \right] f_{act-rv}(t) \\ + \left[\left(A e^{0.66 B \pi K_{rv} r_{rv}(t)^2 l_{rv}} \right) - 1 \right], \end{aligned} \tag{2.16}$$

where, (i) E_{es-rv} is the end systolic elastance (ii) r_{rv-0} is the radius at zero pressure and (iii) f_{act-rv} is the cosine activation function for RV.

2.4.1.3 Atria Modeling

The left and right atrial geometries are modeled using a similar model to the LV geometry. Therefore, the same relations for the left and right atrial volumes and radiuses are used as in the LV model with different parameter values. The atrial pressure radius relationship is modeled by adopting a time-varying elastance pressure volume and expressing the atrial volume as a truncated ellipsoidal shape.

In this model, the truncated ellipsoidal shape is used to represent the geometry of RA and LA. Hence the change in radius of LA is expressed as:

$$\frac{dr_{la}}{dt} = \frac{3(Q_{vp} - Q_{mv})}{4\pi K_{la} l_{la}} \left(\frac{3V_{la}}{2\pi K_{la} l_{la}} \right)^{-\frac{1}{2}} \tag{2.17}$$

where, (i) r_{la}, l_{la} and V_{la} are the radius, length and volume of LA respectively (ii) K_{la} is the constant account for the contraction along the long axis and (iii) Q_{mv} and Q_{vp} are flowrates of MV and pulmonary vein respectively.

Similarly, the rate of change in radius of RA is expressed as:

$$\frac{dr_{ra}}{dt} = \frac{3(Q_{vs} - Q_{tv})}{4\pi K_{ra} l_{ra}} \left(\frac{3V_{ra}}{2\pi K_{ra} l_{ra}} \right)^{-\frac{1}{2}} \tag{2.18}$$

where, (i) r_{ra}, l_{ra} V_{ra} are radius, long axis length and volume of RA respectively (ii) K_{ra} is the constant account for the contraction along the long axis and (iii) Q_{vs} and Q_{tv} are

flowrates of systemic veins and TV respectively.

The atrial pressure radius relationship is modeled by adopting a time-varying elastance pressure volume. The LA pressure is expressed as:

$$P_{la}(t) = \left[E_{min-la} + 0.5\left[E_{max-la} - E_{min-la}\right] f_{act-la}(t-D)\right] \left[\frac{2}{3}\pi K_{la} l_{la}\left(r_{la}^2 - r_{la-0}^2\right)\right] \tag{2.19}$$

where, (i) E_{min-la} and E_{max-la} are minimum and maximum elastance of LA (ii) r_{la-0} is the radius at zero pressure of LA (iii) f_{act-la} is the cosine activation function and (iv) D is the delay in activation function.

The pressure in RA is expressed as:

$$P_{ra}(t) = \left[E_{min-ra} + 0.5\left[E_{max-ra} - E_{min-ra}\right] f_{act-ra}(t-D)\right] \left[\frac{2}{3}\pi K_{ra} l_{ra}\left(r_{ra}^2 - r_{ra-0}^2\right)\right] \tag{2.20}$$

where, (i) E_{min-ra} and E_{max-ra} are the minimum and maximum elastance of RA, (ii) r_{ra-0} is the radius at zero pressure of RA and (iii) f_{act-ra} is the cosine activation function for RA.

Further, the four valves of the heart are modeled using diodes which ensures the unidirectional flow of blood between chambers. For MV, which is situated in between LA and LV, when the pressure inside LA is greater than LV, the valve opens and hence the blood flows from LA to LV. When the pressure inside LV is greater than LA, the valve closes and hence the blood stops flowing. This process is defined as:

$$Q_{mv} = \begin{cases} \frac{P_{la}(t) - P_{lv}(t)}{R_{mv}} & \text{if } P_{la}(t) > P_{lv}(t), \\ 0 & \text{otherwise,} \end{cases} \tag{2.21}$$

where, R_{mv} is the MV resistance.

Similarly, the other valves (TV, PV and AV) are modeled based on the pressure of the compartments to which it is connected.

2.4.2 Modeling of systemic and pulmonary vasculature

The vasculature system consists of systemic and pulmonary circuits. This is modeled using the arterial Windkessel model [1]. Figure 2.9 shows the Windkessel circuit representation of the aorta.

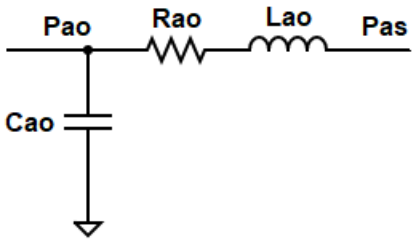

Figure 2.9: Windkessel circuit representation of Aorta [1]

The expressions for pressure and flow rate are obtained as:

$$P_{ao} = \frac{1}{C_{ao}} \int (Q_{as} - Q_{ao})\, dt, \tag{2.22}$$

$$Q_{ao} = \frac{1}{L_{ao}} \int (P_{ao} - R_{ao}Q_{ao} - P_{as})\, dt, \tag{2.23}$$

where, (i) C_{ao}, L_{ao}, R_{ao}, P_{ao} and Q_{ao} are capacitance, inductance, resistance, pressure and flow rate of the aorta and (ii) Q_{as} and P_{as} are flow rate and pressure of the systemic arteries.

Similarly, all the compartments of systemic and pulmonary vasculature are modeled [3].

2.5 Summary

In this chapter, the anatomy of CVS is explained in detail which includes heart, systemic and pulmonary vasculature. The development of methematical model is explained with the basic Windkessel model which includes resistance, inductance and capacitance. The clinical data for input flow rate and output pressure is used and the parameters are estimated. Further to include the complete compartment of CVS, a geometrical model is studied in which the chambers are modeled based on the geometry. Also the pulmonary and systemic circulation is modeled using the Windkessel model. This model is further used for FO modeling and abnormality analysis.

Chapter 3

Baroreflex control for CVS

3.1 Introduction

The baroreflex is a critical mechanism that helps to regulate blood pressure and maintain cardiovascular homeostasis in the human body. It operates through a negative feedback loop involving sensory receptors, control centers in the brain and effectors in the CVS. The afferent limb of the baroreflex refers to the sensory input and signaling that occur from peripheral receptors to the ANS, particularly in brainstem. The baroreflex control design includes the afferent dynamics, ANS and efferent dynamics. The afferent dynamics of baroreflex control illustrate a feedback loop that enables the body to respond rapidly to changes in blood pressure. This regulatory mechanism plays a crucial role in maintaining cardiovascular stability and preventing extreme fluctuations in blood pressure that could be harmful to the body [18]. The afferent nervous fibers attached to the aortic arch are activated due to changes in pressure. he ANS consists of the sympathetic and the parasympathetic nervous system which is responsible for modulating various physiological processes to maintain cardiovascular stability. The balance between sympathetic and parasympathetic influences on the heart and blood vessels, orchestrated by the ANS, is critical for maintaining blood pressure within a narrow and optimal range. The efferent dynamics in baroreflex mechanism is modulated by the ANS. This is essential for adapting to changes in physiological conditions and ensuring cardiovascular homeostasis. The efferent dynamics of the baroreflex are geared toward maintaining cardiovascular homeostasis by adjusting heart rate, cardiac output and vascular resistance in response to changes in blood pressure. This reflex mechanism ensures that blood pressure is kept within a narrow and optimal range to meet the metabolic demands of the body.

Orthostatic Intolerance (OI) is one of the abnormality conditions arises due to the malfunction of baroreflex control which is common in elderly and post flight in astronauts.

It is accompanied by dizziness, falling, syncope and hypotension and is complex to diagnose and treat. In elder people, sudden changes in pressure can cause falling down during postural change under gravity conditions. This is due to decreased baroreflex sensitivity, parasympathetic activity, renal salt water conservation and LV diastolic filling or increased vascular stiffness.

On the other hand, when the astronauts are exposed to microgravity conditions, there will be alterations in the behavior of the CVS which affects the OI of the human system when they return to Earth and get exposed to normal gravity conditions. The ability of the CVS to regulate the blood pressure (i.e. baroreceptor mechanism) will be compromised after the return from microgravity conditions. During space travel the loss of hydrostatic force due to microgravity causes reduction in intravascular volume. The nervous system adapts to these changes and hence this process weakens the baroreflex control under gravity conditions. Studies show that after returning from space, astronauts are provided with medical assistance in the ground station to avoid problems related to OI.

To understand the diagnosis and treatment of hypotension conditions, it is crucial to study the underlying mechanism of short-term blood pressure management. In general, OI happens when there is a change which affects the normal control process of baroreflex and related mechanisms. Experimenting such conditions in human system is difficult and is done in controlled conditions. Hence, it is necessary to develop a mathematical model with baroreflex control for studying the effect of OI in elderly people and microgravity conditions in addition to controlling MAP during disturbance conditions such as postural change, hemorrhage and certain abnormalities.

3.2 Mathematical Modeling

In this section, modeling of CVS using the extended Windkessel model and baroreflex control mechanism using afferent, ANS and efferent dynamics is presented. The integrated block diagram of CVS and baroreflex control is shown in Figure 3.1.

The red and blue arrows in Figure 3.1 indicate the flow of oxygenated blood and deoxygenated blood, respectively. The upper block represents cardiopulmonary system which includes the blood flow between heart and lungs. The middle block represents CVS which consists of heart and systemic vasculature. The heart block is characterized by contractility (c), heart rate (H) and stroke volume (V_{str}). The vasculature is characterized by arterial and venous pressures (Pa, Pv), compliances (Cv, Ca) and peripheral resistance (R). The lower block represents baroreflex control which consists of baroreceptors, medulla oblon-

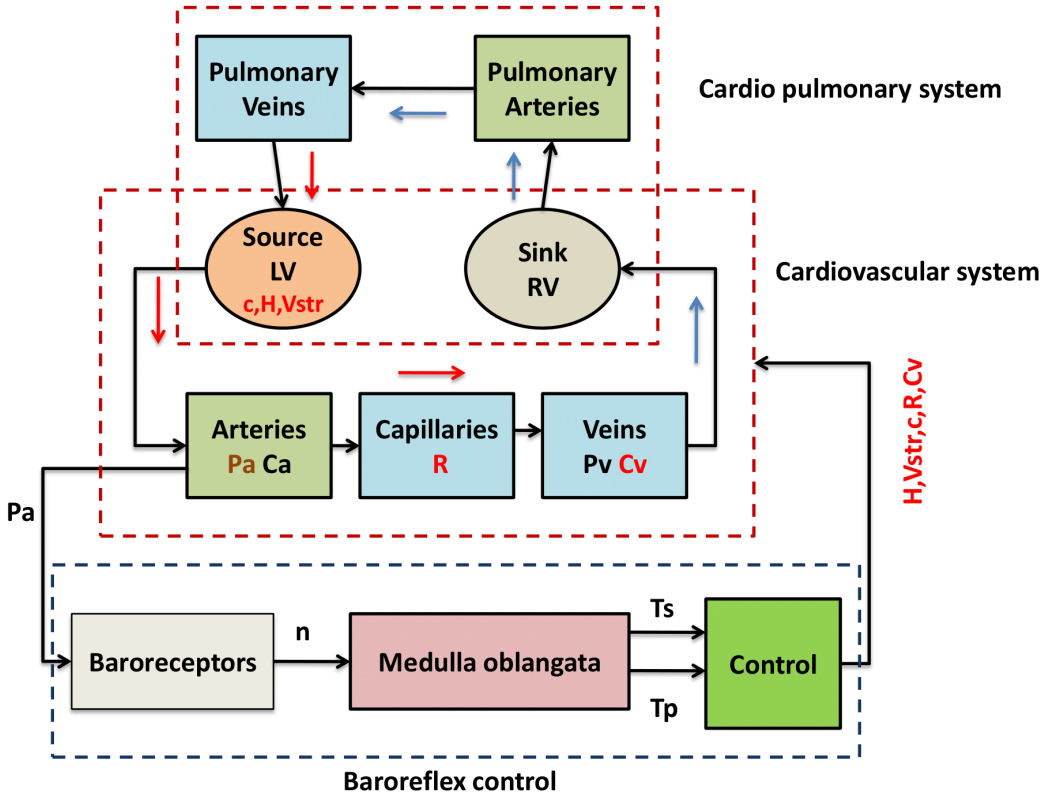

Figure 3.1: Block diagram representation for baroreflex control for CVS

gata, sympathetic and parasympathetic control. The baroreceptor takes MAP as the input and produces firing rates (n) which are given as information to the medulla oblongata. This produces chemical tones (Ts, Tp) which controls the heart and vascular characteristics.

3.2.1 Heart and circulation model

This model consists of LV and RV as source and sink for the circulation respectively. The valves of the LV (aortic and mitral valves) are modeled as diodes to ensure no backward flow of blood and the valves of the RV (tricuspid and pulmonary valves) are ignored. The LV is modeled as non-linear pulsatile pressure source [56], where the diastolic pressure $p_d(V_{lv})$ is given by:

$$p_d(V_{lv}) = a(V_{lv} - b)^2 \tag{3.1}$$

where, V_{lv} is the volume in the LV, a is the ventricular elastance during relaxation and b is the ventricular volume for zero diastolic pressure. Systolic LV pressure $p_s(V_{lv})$ is given by:

$$p_s(V_{lv}) = p_d(V_{lv}) + cV_{lv} - d \tag{3.2}$$

where, c and d represent the volume dependent and volume independent parts of the pressure respectively. Hence, the total isovolumetric ventricular pressure $p_{lv}(t, V_{lv})$ is given by:

$$p_{lv}(t, V_{lv}) = a(V_{lv} - b)^2 + c(V_{lv} - d)f(t) \tag{3.3}$$

where, f(t) is an activation function is a simple polynomial model and is given by [17]:

$$f(t) = \begin{cases} p_p(H)\frac{(t_a-\alpha)^n(\beta-t_a)^m}{n^n m^m[(\beta-\alpha)/(m+n)]^{m+n}}, & \alpha \leq t_a \leq \beta(H) \\ 0 & \beta(H) < t_a < t_h \end{cases} \tag{3.4}$$

$$t_a = mod(t, t_h) \tag{3.5}$$

$$t_p(H) = t_{p,min} + \left[\frac{\theta^v}{H^v + \theta^v}\right](t_{p,max} - t_{p,min}) \tag{3.6}$$

$$\beta(H) = \frac{n+m}{n}t_p(H) - \frac{\alpha m}{n} \tag{3.7}$$

$$p_p(H) = p_{p,min} + \left[\frac{H^\eta}{H^\eta + \phi^\eta}\right](p_{p,max} - p_{p,min}) \tag{3.8}$$

where $p_p(H)$ is the peak ventricular pressure, n and m characterize contraction and relaxation respectively, α represents onset of contraction, β is the time for end of force, t_h is the heart period ($t_h = 1/H$), H is the heart rate , $t_p(H)$ is the time for the peak pressure, θ and ϕ are medians of t_p and p_p respectively and v and η are the steepness of t_p and p_p curves respectively.

This will be coupled to the windkessel arterial load and it is fed by a constant venous pressure reservoir. In the proposed model, the arterial load is replaced with the systemic vasculature which includes arteries, veins and capillaries. For a non-pulsatile model of LV, the input to the systemic circuit is the outflow from LV and is given by:

$$q_{out} = HV_{str} \tag{3.9}$$

where, V_{str} is the stroke volume and H is the heart rate.

The blood is assumed to be an incompressible Newtonian fluid and arteries and veins as compartments characterized by compliance [57], [58]. The analytical expressions relating to the volume (V), pressure (P), compliance of the vessel (C), flow (q) and resistance (R) between two vessels are:

$$\frac{dV}{dt} = q_{in} - q_{out} \tag{3.10}$$

$$V = CP \tag{3.11}$$

$$q = \frac{P_{in} - P_{out}}{R} \tag{3.12}$$

$$\frac{dV}{dt} = C\frac{dP}{dt} \tag{3.13}$$

The main pressure drop occurs at capillaries which are modeled as a systemic/peripheral resistance to the flow between arteries and veins. Similarly, dynamical equations for pulmonary circuits can be derived. The outflow from the LV is the input to the arterial system, from where the blood flows into the veins via capillaries. From veins, it reaches RV (sink) and the blood will flow into LV through veins. This is considered as the inflow to the LV. The outflow and inflow rates are given by:

$$Q_{out}(t) = \begin{cases} \frac{P_{lv}(t) - P_a(t)}{R_{out}} & P_{lv}(t) > Pa(t) \\ 0 & otherwise \end{cases} \tag{3.14}$$

$$Q_{in}(t) = \begin{cases} \frac{P_r - P_{lv}(t)}{R_{in}} & P_r > P_{lv}(t) \\ 0 & otherwise \end{cases} \tag{3.15}$$

where, Q_{out}, Q_{in} are the out and inflows of the LV, R_{in} is the resistance to flow into the LV, R_{out} is the resistance to flow out of the LV, r is the resistance to the flow from veins to RV, P_{lv} is the left ventricular pressure and P_a is the pressure at arteries.

Using (3.1 - 3.15), the expressions of pressure for CVS are derived as follows:

$$\frac{d}{dt}P_a(t) = \frac{-1}{RC_a}P_a(t) + \frac{1}{RC_v}P_v(t) + \frac{Q_{out}(t)}{C_a} \tag{3.16}$$

$$\frac{d}{dt}P_v(t) = \frac{-1}{C_v}\left(\frac{1}{R} + \frac{1}{r}\right)P_v(t) + \frac{1}{RC_v}P_a(t) \tag{3.17}$$

where, P_a and C_a are the arterial pressure and compliance, P_v and C_v are the venous pressure and compliance respectively. R is the peripheral resistance and q is the blood flow between arteries and veins. The MAP $\bar{P}_a$ of the pulsatile model for a heart period is given by:

$$\frac{d\bar{P}_a}{dt} = \frac{1}{kH(t)}(P_a - \bar{P}_a) \tag{3.18}$$

where, k is a constant.

3.2.2 Model of baroreflex control

The cardiovascular model is non-linearly controlled by the baroreceptors and it consists of three parts (i) the afferent dynamics from baroreceptors to the ANS (ii) the processing unit to process firing rate into tones and (iii) the efferent dynamics from ANS to the control parameters [59], [60].

The process begins with specialized sensory receptors called baroreceptors, which are located near the carotid sinus in the carotid arteries and the aortic arch. When there is a change in blood pressure these baroreceptors are activated. The arterial walls will stretch more when there is a rise in blood pressure and they stretch less when there is a dip in blood pressure. The sensory neurons transmit the electrical signal generated by the baroreceptors to the brain and are known as afferent dynamics. The sympathetic and parasympathetic tones in the ANS are responsible for regulating many bodily functions, including heart rate and vascular tones.

In response to the brainstem's assessment, the ANS is activated to make necessary adjustments by stimulating vagus nerve for an increase in blood pressure and stimulating sympathetic nerve for a decrease in blood pressure. The heart and blood vessels are the primary effectors in the CVS. They respond to the signals from the ANS by adjusting heart rate, stroke volume and vascular resistance (the degree of constriction or dilation of blood vessels) and known as the effector dynamics. The baroreflex operates as a continuous feedback loop. As blood pressure returns to the desired set point, the baroreceptors detect this change and generate the brainstem signal to reduce the autonomic responses. This helps to maintain blood pressure within the allowable range.

3.2.2.1 Model of afferent dynamics

The baroreceptor is a mechanoreceptor and can be modeled as a spring-damper system [21], which deploys viscous nature of blood and elastic nature of the aortic wall. Strain applied to this model will be proportional to the pressure (MAP) sensed. The total stress produced will be transduced into the current $I(t)$ which in turn transmit as action potentials $V_m(t)$ by the Hodgkin-Huxley equivalent model across the nerves to the ANS [61] and [20]. This is expressed as:

$$I(t) = k_1 \bar{P}_a(t) + k_2 \frac{d}{dt} \bar{P}_a(t) \tag{3.19}$$

where, k_1 and k_2 are constants.

The action potentials $V_m(t)$ are given by:

$$C\frac{d}{dt}V_m(t) = I(t) - g_{leak}V_m(t) \tag{3.20}$$

where, C is the capacitance of the lipid layer and g_{leak} is the leak conductance.

A unified model for average firing rate is derived as [61]:

$$\frac{d}{dt}n_i(t) = k_i\frac{d}{dt}\bar{P}_a(t)\frac{n(M-n)}{(M/2)^2} - \frac{n_i}{\tau_i} \tag{3.21}$$

where, $i = L$-long, S-short and I-intermediate neuronal reflexes, $n = n_I+n_L+n_S+N$. Here, N and M are minimum and maximum firing rates respectively.

3.2.2.2 Model of ANS

The sympathetic (T_s) and parasympathetic (T_p) tones are sigmoidally related to firing rate as:

$$T_s(\bar{n}) = \frac{1}{1+\left(\frac{\bar{n}}{\mu_n}\right)^{v_n}} \tag{3.22}$$

$$T_p(\bar{n}) = \frac{1}{1+\left(\frac{\mu_n}{\bar{n}}\right)^{v_n}} \tag{3.23}$$

where, $\bar{n}$ is the firing rate, v_n is the constant that determines steepness and μ_n is the firing at which $T_s = T_p = 0.5$ [19].

3.2.2.3 Model of efferent dynamics

The efferent dynamics refers to how the parameters (H, R, V_{str}, c and C_v) are controlled by tones chemically [57]. The corresponding equations are:

$$\frac{d}{dt}H = \frac{1}{\tau_H}\left(-H + \alpha_H T_s - \beta_s T_p + \gamma_H\right) \tag{3.24}$$

$$\frac{d}{dt}R = \frac{1}{\tau_R}\left(-R + \alpha_R T_s + \gamma_R\right) \tag{3.25}$$

$$\frac{d}{dt}V_{str} = \frac{1}{\tau_{V_{str}}}\left(-V_{str} + \alpha_{V_{str}} T_s + \gamma_{V_{str}}\right) \tag{3.26}$$

$$\frac{d}{dt}c = \frac{1}{\tau_c}\left(-c + \alpha_c T_s + \gamma_c\right) \tag{3.27}$$

$$\frac{d}{dt}C_v = \frac{1}{\tau_{C_v}}\left(-C_v + \beta_{C_v}T_p + \gamma_{C_v}\right) \tag{3.28}$$

where, τ_H, τ_R, $\tau_{V_{str}}$, τ_c and τ_{C_v} are the time constants corresponding to the control parameters H, R, V_{str}, c, C_v respectively. α_H, α_R, $\alpha_{V_{str}}$ and α_c are parameters that determine the amount of control by the sympathetic tone. β_H and β_{C_v} are parameters that determine the amount of control by the parasympathetic tones. γ_H, γ_R, $\gamma_{V_{str}}$, γ_c and γ_{C_v} are the value of the control parameters under complete denervation [21].

3.3 Modeling of Postural Changes

To study the effect of baroreflex control in postural change, a supine to standing is introduced as a disturbance. The change in position of the veins from supine to standing is represented in Figure 3.2. The cylinders represent veins and the arrow indicates the change in orientation of vessels with respect to ground from supine to standing. This introduces the effect of gravity on venous pressure (increased from 5 mmHg to 150-200 mmHg) in turn decreases the MAP [19]. For the standing model, the supine position is taken as a

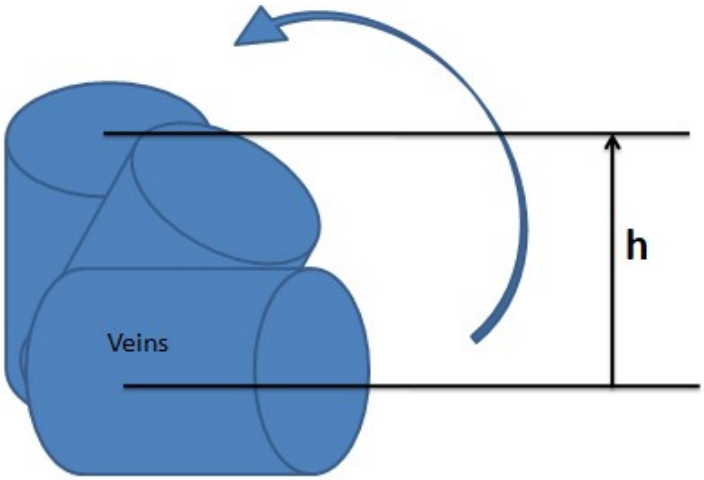

Figure 3.2: Vein under postural change

reference. The change in height is modeled by:

$$h(t) = \frac{h_{max}}{1 + exp\left(t - t_{st} - \delta\right)} \tag{3.29}$$

where, h_{max} is the maximum height, t_{st} is the time at which the subject stands and δ is the time taken to change the position from supine to standing. Hence, the change in venous

pressure $P_v(t)$ is [19]:

$$P_v(t) = P_v(t) + \rho g h(t) \tag{3.30}$$

where, ρ is the blood density, g is the acceleration due to gravity and h is the change in height.

3.4 Results and Discussion

The analytical expressions for representing the proposed model are solved using ODE45 in MATLAB. This model is validated under postural change (supine to standing) using the clinical data [22] for healthy condition. This model is used for further simulation studies (i) Positional change (supine to standing and vice-versa) for a healthy person and (ii) Supine to standing for orthostatic hypotension and hypertension condition.

The simulated result of MAP for pulsatile and non pulsatile model integrated with the baroreflex and pulmonary circuit along with clinical data [22] are presented in Figure 3.3. The validation of the proposed models are performed with the available clinical data which is limited from 50 sec to 90 sec only. At time t=60 sec, supine to standing position is introduced and it is observed that pressure is dropped from 93 mmHg (nominal) to 56 mmHg. Due to the baroreflex control mechanism, the pressure is driven back to the nominal value with a recovery time of 40 sec from the time of disturbance given. The corresponding effect due to postural change on contractility, peripheral resistance, compliance, stroke volume, firing activity and venous pressure is shown in Figures 3.4 and 3.5.

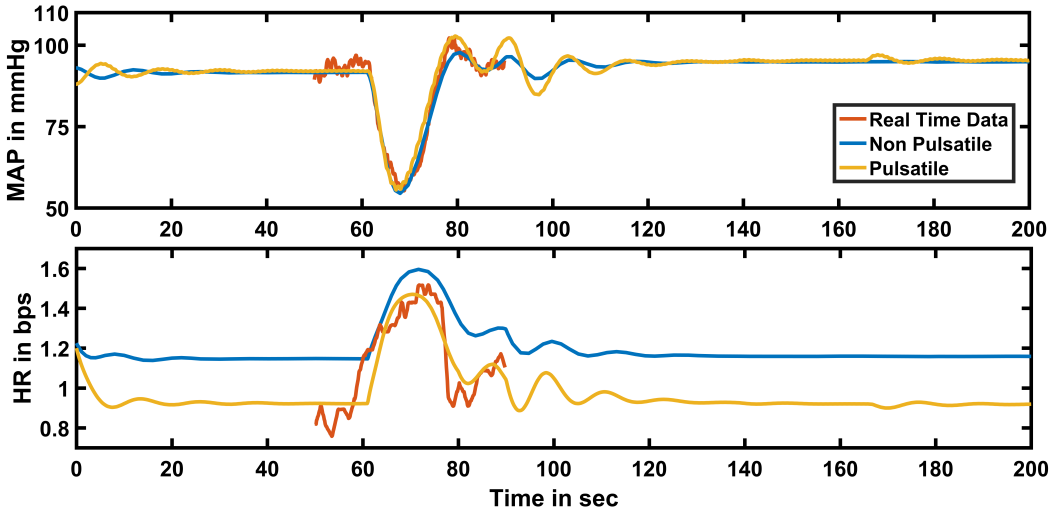

Figure 3.3: Responses of MAP and HR for supine to standing position at t=60 sec under normal condition

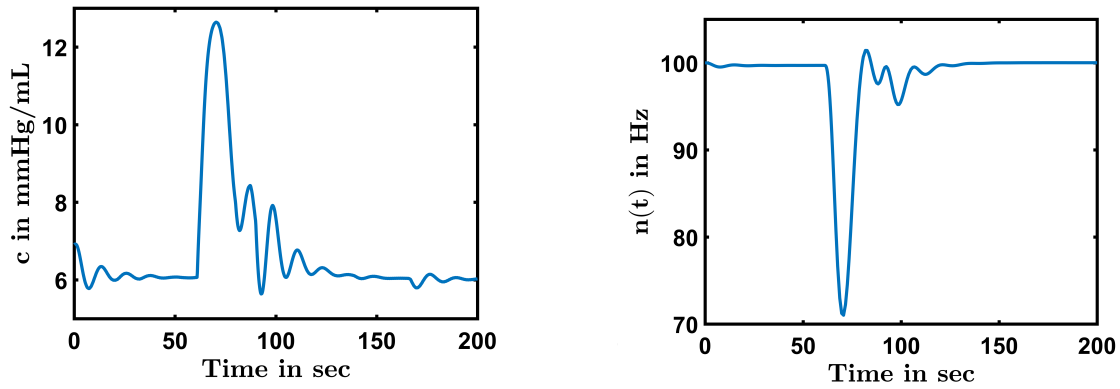

(a) **(b)**

Figure 3.4: Responses of LV contractility and firing rate for supine to standing at t=60 sec under normal conditions

It is observed that the venous pressure increases because of the increase in blood volume in the veins due to the effect of gravity which in turn reduces MAP as shown in Figure 3.3. The firing activity and venous compliance are also decreased as shown in Figure 3.4b and 3.5b . It is also observed that there is an increase in HR, peripheral resistance, stroke volume and contractility of the heart due to the dip in MAP as shown in Figures 3.4a, 3.5c and 3.5d.

The Root Mean Square Errors (RMSE) for non pulsatile and pulsatile models are computed by using 3.31 is shown in Table 3.1.

$$RMSE = \sqrt{\sum_{i=1}^{n} \frac{(x - \bar{x})^2}{n}} \tag{3.31}$$

where, x is the simulated output, $\bar{x}$ is the realtime data and n is the number of sample. From Table 3.1, it is observed that pulsatile model provides the least error compared to the non pulsatile model.

Table 3.1: RMSE for MAP and HR of non pulsatile and pulsatile model.

Model	RMSE	
	MAP	HR
Non Pulsatile model	6.3781	0.22119
Pulsatile model	4.7525	0.0931

For further analysis, the pulsatile model is only considered for simulation. The simulation is performed by introducing supine to standing at t=60 sec along with standing to

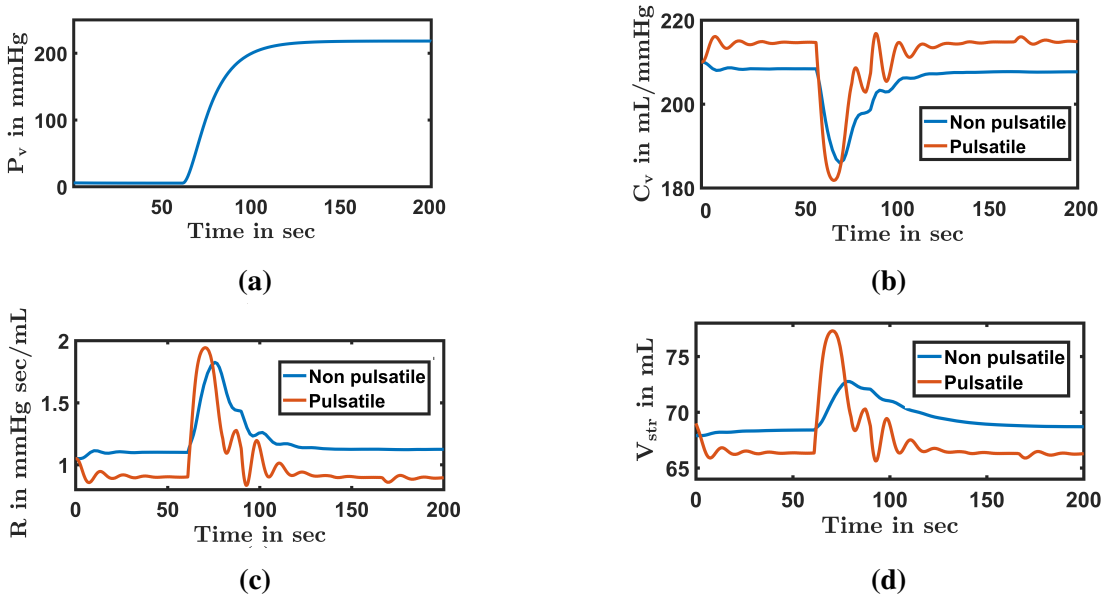

Figure 3.5: Responses of venous pressure, peripheral resistance, stroke volume, venous compliance for supine to standing at t=60 sec under normal condition

supine position at t=200 sec and the corresponding responses are shown in Figures 3.6 and 3.7. This results to increase in MAP, peripheral resistance, stroke volume and a decrease in compliance for supine to standing condition and vice versa for standing to supine condition.

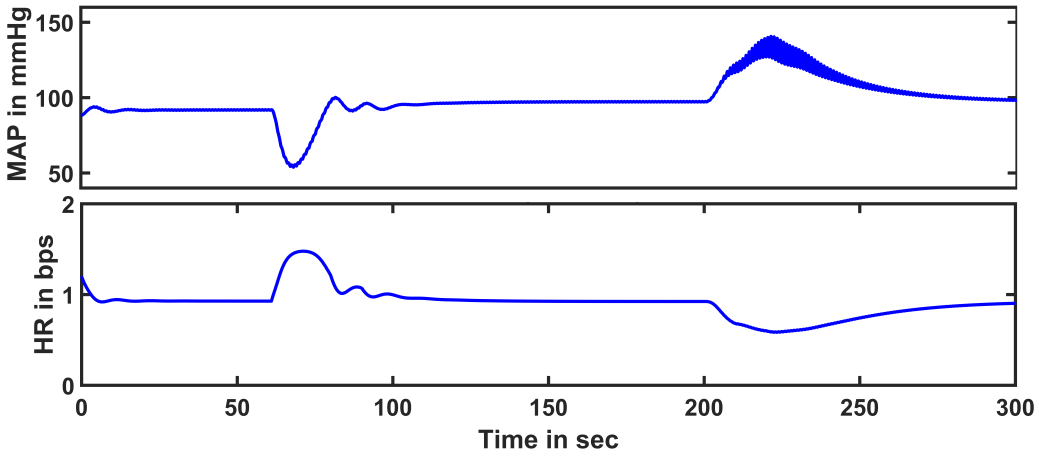

Figure 3.6: Responses of MAP and HR for supine to standing at t=60 sec and for standing to supine at t=200 sec under normal condition for pulsatile model

OI refers to a medical condition where the HR cannot be controlled by poor baroreflex efferent innervation of the heart. This is observed commonly in elderly and astronauts. This is modeled by changing the baroreflex parameter which in turn loses the ability to

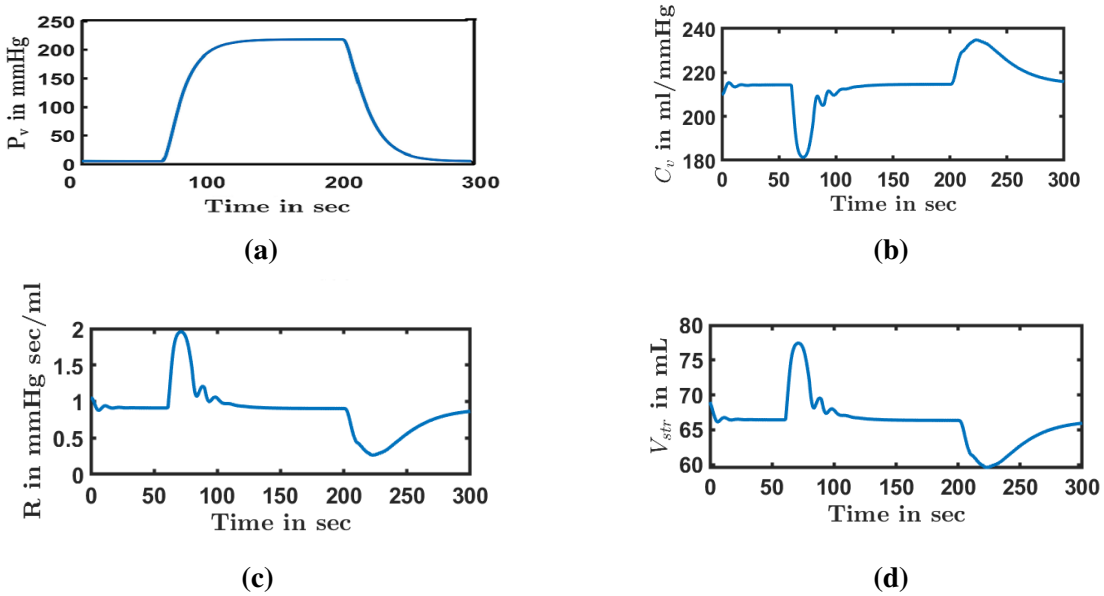

Figure 3.7: Responses of venous pressure, compliance, peripheral resistance and stroke volume for supine to standing of pulsatile model at t=60 sec and standing to supine at t=200 sec under normal condition

make the pressure to nominal value. Figure 3.8 show the simulated results for the effect of orthostatic hypotension and hypertension condition on MAP and HR. At t=60 sec a postural change from supine to standing is introduced along with reduced sympathetic gain. Due to the abnormalities in the vascular baroreceptors which happens due to postflight, age, brain stem stroke etc., the MAP and HR cannot attain its steady state value which leads to orthostatic hypotension as shown in Figure 3.8. At t=200 sec, postural change from standing to supine is introduced along with a change in parasympathetic baroreflex gain. Due to the poor control of parasympathetic nerve system, a higher pressure and lower HR is observed which leads to orthostatic hypertension.

The proposed model is further simulated for short-term variation in MAP which may occur due to other underlying issues along with postural change. To perform the simulation, a disturbance signal is introduced for different conditions like normal, supine to standing and standing to supine. Under normal conditions, the disturbance is introduced at t=20 sec. Further, disturbance is introduced along with supine to standing and standing to supine position at t=60 sec and t=100 sec respectively. It is observed that MAP and HR attain its steady state value which is due to the regulatory action taken by the baroreflex

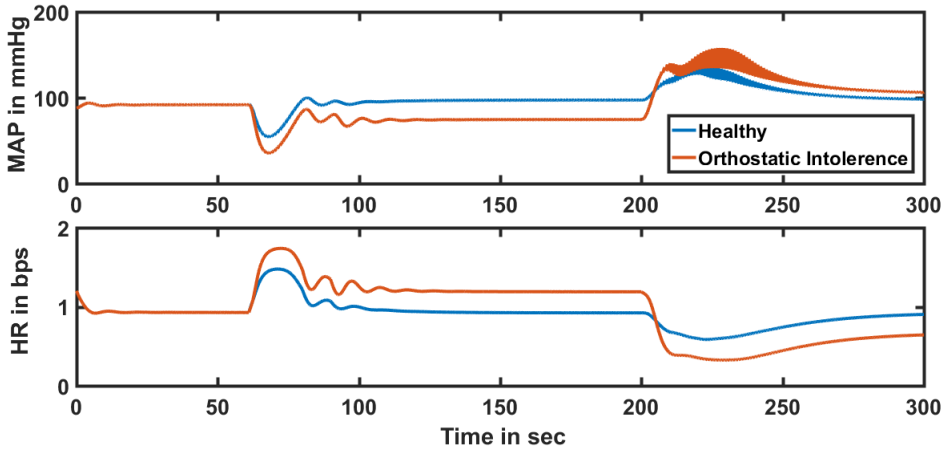

Figure 3.8: Responses of MAP and HR for individuals with OI (hypotensive at t=60 sec and hypertensive at t=200 sec) and healthy condition for Pulsatile model

mechanism. This is shown in Figure 3.9.

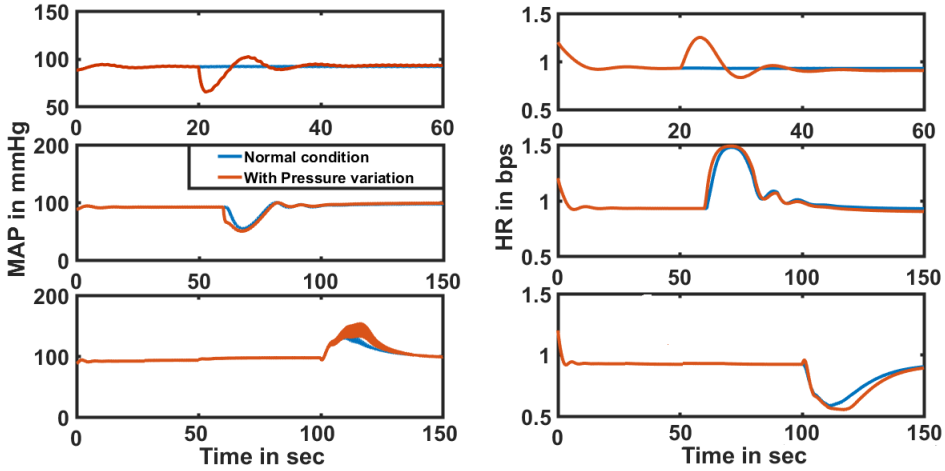

Figure 3.9: Responses of MAP and HR for individuals with pressure disturbance under normal condition (t=0-60 sec), supine to standing (t=60-200 sec) and standing to supine (t=100-150 sec)

3.5 Summary

A mathematical model for baroreflex control along with the CVS is proposed to study the complex interactions between ANS and CVS for healthy and orthostatic hypotension conditions. The simulation study indicates that the proposed integrated system with pulsatile model of heart is closer to the real time data compared to the non pulsatile model of the

heart. To show the efficiency of the pulsatile model, the simulation is carried out under (i) postural changes like supine to standing and standing to supine under normal conditions and (ii) Orthostatic hypotension condition for supine to standing.

Chapter 4

Fractional order Windkessel and Geometric Models

4.1 Introduction

The IO Windkessel and geometric models do not consider the viscoelastic behavior of the arterial system. To incorporate these behaviors, fractionality is introduced to Windkessel models (Wk2, Wk3 and Wk4) and geometric model. The capacitor which represents the arterial compliance of the blood vessel is modeled using the FO differential equation. Hence, the elastic and viscous nature of the aorta and other blood vessels are captured which increases the accuracy of arterial system modeling.

4.2 Preliminaries of Fractional Calculus

The following definitions are used to describe the fractional derivative and integration operation:

1. Riemann-Liouville Fractional Integral [62]

   This definition is derived directly from the traditional expression of repeated integration. For this purpose, it starts with the following Cauchy's formula for evaluating n^{th} integration (J^n) of the function $f(t)$:

$$J^n f(t) = \frac{1}{(n-1)!} \int_a^t (t-\tau)^{n-1} f(\tau) d\tau \tag{4.1}$$

The subscripts a and t denote the two limits (or terminals [63]) related to the operation. Since (4.1) contains factorial, it cannot be used for non-integer n. By replacing the factorial by its analytical expansion i.e. gamma function in order to generalize (4.1) for all $\alpha \in \mathbb{R}^+$, we obtain Riemann-Liouville fractional integral J^{α}_{RL} as follows:

$$J^{\alpha}_{RL} f(t) = \frac{1}{\Gamma(\alpha)} \int_{a}^{t} (t-\tau)^{\alpha-1} f(\tau) d\tau \tag{4.2}$$

where, the gamma function $\Gamma(\alpha)$ is defined by the integral

$$\Gamma(\alpha) = \int_{0}^{\infty} e^{-t} t^{\alpha-1} dt \tag{4.3}$$

Properties

(a) Integration of order, $\alpha = 0$

$$J^{0}_{RL} f(t) = f(t) \tag{4.4}$$

(b) Repeated Integration

$$J^{\alpha}_{RL} J^{\beta}_{RL} f(t) = J^{\alpha+\beta}_{RL} f(t) \tag{4.5}$$

where, $\alpha, \beta \in \mathbb{R}^+$.

(c) Convolution

Let the $\phi_{\alpha}(t)$ be defined as:

$$\phi_{\alpha}(t) = \frac{t^{\alpha-1}}{\Gamma(\alpha)} \tag{4.6}$$

Then, (4.2) can be expressed as the following convolution:

$$J^{\alpha}_{RL} f(t) = \phi_{\alpha}(t) * f(t) \tag{4.7}$$

2. Riemann-Liouville Fractional Derivative [64]

The fractional derivative D^{α}_{RL} is expressed as:

$$D^{\alpha}_{RL} := D^n D^{\alpha-n} = D^n J^{n-\alpha}_{RL} \tag{4.8}$$

where, D denotes derivative operation and $(n-1) < \alpha \leq n; (n \in \mathbb{N})$.

Therefore, from (4.2) and (4.8), the Riemann-Liouville fractional derivative is obtained as follows:

$$D^{\alpha}_{RL} f(t) = \frac{d^n}{dt^n} \left[\frac{1}{\Gamma(n-\alpha)} \int_a^t \frac{f(\tau)}{(t-\tau)^{\alpha-n+1}} d\tau \right] \tag{4.9}$$

3. Caputo Fractional Derivative [65]

   The fractional derivative D^{α}_{C} is expressed as:

$$D^{\alpha}_{C} := D^{\alpha-n} D^n = J^{n-\alpha}_{RL} D^n \tag{4.10}$$

   Therefore, from (4.2) and (4.10), the Caputo fractional derivative is obtained as follows:

$$D^{\alpha}_{C} f(t) = J^{n-\alpha}_{RL} f^n(t) = \frac{1}{\Gamma(n-\alpha)} \int_a^t \frac{f^n(\tau)}{(t-\tau)^{\alpha-n+1}} d\tau \tag{4.11}$$

4. Grunwald-Letnikov Derivative [66]

   We have the following fundamental definition of n^{th} order derivative $(n \in \mathbb{N})$:

$$D^n f(t) = \lim_{h \to 0} \frac{1}{h^n} \sum_{k=0}^{n} (-1)^k \binom{n}{k} f(t-kh) \tag{4.12}$$

   where,

$$\binom{n}{k} = \frac{n!}{(n-k)!k!} = \frac{\Gamma(n+1)}{\Gamma(n-k+1)\Gamma(k+1)}$$

   The generalization of (4.12) to α^{th} order $(\alpha \in \mathbb{R}^+)$ leads to the following Grunwald-Letnikov derivative (D^{α}_{GL}):

$$D^{\alpha}_{GL} f(t) = \lim_{h \to 0} \frac{1}{h^{\alpha}} \sum_{k=0}^{\left[\frac{t-a}{h}\right]} (-1)^k \binom{\alpha}{k} f(t-kh) \tag{4.13}$$

where,

$$\binom{\alpha}{k} = \frac{\Gamma(\alpha+1)}{\Gamma(\alpha-k+1)\Gamma(k+1)}$$

In (4.13), $f(t)$ is defined over $[a,t]$. Also, $\left[\frac{t-a}{h}\right]$ truncates $\left(\frac{t-a}{h}\right)$ to integer.

5. Grunwald-Letnikov Integral [62]

   Generalization of (4.12) to $(-\alpha)^{th}$ order $(\alpha \in \mathbb{R}^+)$ leads to the following Grunwald-Letnikov integral (J^{α}_{GL}):

$$J^{\alpha}_{GL} f(t) = D^{-\alpha} f(t) = \lim_{h\to 0} \frac{1}{h^{-\alpha}} \sum_{k=0}^{\left[\frac{t-a}{h}\right]} (-1)^k \binom{-\alpha}{k} f(t-kh) \tag{4.14}$$

   Using the identity $\binom{-\alpha}{k} = (-1)^k \frac{\Gamma(\alpha+k)}{\Gamma(\alpha)k!}$, we rewrite (4.14) as follows:

$$J^{\alpha}_{GL} f(t) = \lim_{h\to 0} h^{\alpha} \sum_{k=0}^{\left[\frac{t-a}{h}\right]} \frac{\Gamma(\alpha+k)}{\Gamma(\alpha)k!} f(t-kh) \tag{4.15}$$

6. Miller-Ross Sequential Fractional Derivative [64]

   It is defined as follows:

$$D^{\alpha} f(t) = D^{\alpha_1} D^{\alpha_2} \dots D^{\alpha_n} f(t) \tag{4.16}$$

   where,

$$\alpha = \sum_{k=1}^{n} \alpha_k, 0 < \alpha_k \leq 1 \tag{4.17}$$

   This definition is useful for obtaining fractional derivative of any arbitrary order. The derivative operator D^{α} can be Riemann-Liouville or Caputo.

7. Oldham and Spanier [44]

$$\frac{d^q f(\beta x)}{dx^q} = \beta^q \frac{d^q f(\beta x)}{d(\beta x)^q} \tag{4.18}$$

This makes it suitable for the study of scaling and scale invariance. There is connection between local-scaling, box-dimension of an irregular function and order of Local Fractional Derivative.

8. Kolwankar and Gangal [44]

   Local fractional derivative is defined by Kolwankar and Gangal to explain the behavior of *continuous but nowhere differentiable* function. For $0 < q < 1$, the local fractional derivative at point $x = y$, for $f : [0, 1] \to \mathbb{R}$ is:

$$D^q f(y) = \lim_{x \to y} \frac{d^q (f(x) - f(y))}{d(x - y)^q} \tag{4.19}$$

Some important observations

1. By virtue of its form, the definition (4.13) is utilized for the numerical evaluation of fractional derivatives. On the other hand, Riemann-Liouville (4.9) and Caputo (4.11) definitions are useful in finding the fractional derivatives analytically [62].

2. Grunwald-Letnikov derivative given in (4.13) can also be expressed as follows [64]:

$$D^{\alpha}_{GL} f(t) = \sum_{k=0}^{m} \frac{f^{(k)}(a)(t-a)^{-\alpha+k}}{\Gamma(-\alpha+k+1)} + \frac{1}{\Gamma(-\alpha+m+1)} \int_a^t (t-\tau)^{m-\alpha} f^{(m+1)}(\tau) d\tau \tag{4.20}$$

   This is true under the assumption that the derivatives $f^{(k)}(t), (k = 1, 2, \ldots, m+1)$ are continuous in the closed interval $[a, t]$ and m is an integer number satisfying the condition $m > \alpha - 1$. The smallest possible value for m is obtained by the inequality $m \leq \alpha < m + 1$.

   For the above assumptions, Riemann-Liouville fractional derivative given in (4.9) can also be expressed as follows:

$$D^{\alpha}_{RL} f(t) = \sum_{k=0}^{m} \frac{f^{(k)}(a)(t-a)^{-\alpha+k}}{\Gamma(-\alpha+k+1)} + \frac{1}{\Gamma(-\alpha+m+1)} \int_a^t (t-\tau)^{m-\alpha} f^{(m+1)}(\tau) d\tau \tag{4.21}$$

   Therefore, from (4.20) and (4.21), the Grunwald-Letnikov derivative definition (4.13) is equivalent to the Riemann-Liouville derivative definition (4.9) under the above discussed assumptions.

3. On substituting $n = m + 1$, Riemann-Lioville derivative definition (4.21) can be rewritten as:

$$D^{\alpha}_{RL}f(t) = \sum_{k=0}^{n-1} \frac{f^{(k)}(a)(t-a)^{-\alpha+k}}{\Gamma(-\alpha+k+1)} + \frac{1}{\Gamma(-\alpha+n)} \int_{a}^{t} (t-\tau)^{n-1-\alpha} f^{(n)}(\tau) d\tau$$

$$= \frac{1}{\Gamma(n-\alpha)} \int_{a}^{t} \frac{f^{(n)}(\tau)}{(t-\tau)^{\alpha-n+1}} d\tau + \sum_{k=0}^{n-1} \frac{f^{(k)}(a)(t-a)^{-\alpha+k}}{\Gamma(-\alpha+k+1)} \tag{4.22}$$

Therefore, using (4.6), (4.11), and (4.22), we get:

$$D^{\alpha}_{RL}f(t) = D^{\alpha}_{C}f(t) + \sum_{k=0}^{n-1} \phi_{k-\alpha+1}(t-a) f^{(k)}(a) \tag{4.23}$$

The equation (4.23) represents the relationship between Riemann-Lioville and Caputo derivatives.

4. With $a = 0$, Caputo's derivative (4.11) of a constant is 0 whereas the Riemann-Lioville derivative of a constant is unbounded at $t = 0$. However, if one considers the lower terminal a as $-\infty$ in the Riemann-Lioville derivative definition (4.9), the derivative of a constant is 0.

5. Short Memory Principle [64]: It follows from the coefficients in the Grunwald-Letnikov definition (4.13) that for $t >> a$, the role of the *history* of the behavior of the function $f(t)$ near the lower terminal a can be neglected. This leads to the following *short memory principle* which takes into account the behavior of $f(t)$ only in the recent past, i.e. in the interval $[t-L, t]$ instead of $[a, t]$; where, L is the memory length:

$$D^{\alpha}_{GL}f(t) := {}_{a}D^{\alpha}_{t} \approx {}_{t-L}D^{\alpha}_{t}, \qquad (t < a + L) \tag{4.24}$$

Thus, according to (4.24), the Grunwald-Letnikov fractional derivative with the fixed lower terminal a is approximated by the one with moving lower terminal $t - L$. Due to this, the number of addends in the approximated derivative definition never exceeds $[L/h]$. This simplification, however, leads to some inaccuracy due to loss in information.

4.3 Laplace Transform of Fractional Derivatives

Laplace transform of the function $f(t)$ is a function $F(s)$ of the complex variable s. The $F(s)$ is obtained as:

$$F(s) = \mathcal{L}\{f(t)\} = \int_0^\infty e^{-st} f(t) dt \tag{4.25}$$

The Laplace transform of fractional derivatives (with the lower terminal $a = 0$) are as follows [64]:

1. Laplace Transform of Riemann-Liouville Derivative

$$\mathcal{L}\{D^\alpha_{RL} f(t)\} = s^\alpha F(s) - \sum_{k=0}^{n-1} s^k D^{(\alpha-k-1)}_{RL} f(0) \tag{4.26}$$

   where, $F(s) = \mathcal{L}\{f(t)\}$ and $(n-1) \leq \alpha < n$.

2. Laplace Transform of Caputo Derivative

$$\mathcal{L}\{D^\alpha_{C} f(t)\} = s^\alpha F(s) - \sum_{k=0}^{n-1} s^{\alpha-k-1} f^{(k)}(0) \tag{4.27}$$

   where, $(n-1) \leq \alpha < n$.

3. Laplace Transform of Grunwald-Letnikov Derivative (4.20) with $a = 0$

$$\mathcal{L}\{D^\alpha_{GL} f(t)\} = s^\alpha F(s) \tag{4.28}$$

As seen from (4.26), for calculating Laplace transform of Riemann-Liouville derivative one requires initial conditions $D^{(\alpha-k-1)}_{RL} f(0)$, which are fractional derivatives. On the other hand, the Laplace transform of Caputo derivative (4.27) requires initial conditions $f^{(k)}(0)$, which are IO derivatives. Since such initial conditions can be easily interpreted from physical data and observations, Caputo derivative is a more practical definition than Riemann-Liouville derivative.

4.4 FO Windkessel Models

The Windkessel models presented in section 2.3 do not consider the viscoelastic behavior of the arterial system. To incorporate these behaviors, fractionality is introduced to Windkessel models (Wk2, Wk3 and Wk4). The capacitor which represents the arterial compliance of the blood vessel is modeled using the FO differential equation. Hence, the elastic and viscous nature of the aorta is captured which increases the accuracy of modeling of the arterial system.

By introducing fractionality to the capacitor in the Wk2, equation (2.2) can be rewritten as:

$$\frac{d^{\alpha}P(t)}{dt^{\alpha}} = \frac{1}{C}\left(I(t) - \frac{P(t)}{R}\right) \tag{4.29}$$

where, α is the FO of the differential equation. Similarly, the fractional term (α) is introduced in Wk3 and Wk4 models. The corresponding expressions are written as:

$$\frac{d^{\alpha}P(t)}{dt^{\alpha}} = \frac{1}{C}\left[\left(1 + \frac{r}{R}\right)I(t) + Cr\frac{dI(t)}{dt} - \frac{P(t)}{R}\right] \tag{4.30}$$

$$\frac{d^{\alpha}P(t)}{dt^{\alpha}} = \frac{1}{C}\left[\left(1 + \frac{r}{R}\right)I(t) + \left(Cr + \frac{L}{R}\right)\frac{dI(t)}{dt} + LC\frac{d^2I(t)}{dt^2} - \frac{P(t)}{R}\right] \tag{4.31}$$

4.5 FO Geometric Model

To represent the FO model of CVS, fractionality terms α and β are introduced. Since the geometry of LV, LA and RA are similar, the fractionality α is introduced in (2.11), (2.17) and (2.18) for representing the FO differential equations of CVS. The fractional term β is introduced in (2.15) to represent the FO differential equation of RV. The corresponding FO equations for LV, RV, LA and RA are expressed as:

$$\frac{dr_{lv}^{\alpha}}{dt^{\alpha}} = \frac{3(Q_{mv} - Q_{av})}{4\pi K_{lv} l_{lv}}\left(\frac{6V_{lv}}{4\pi K_{lv} l_{lv}}\right)^{-\frac{1}{2}} \tag{4.32}$$

$$\frac{dr_{rv}^{\beta}}{dt^{\beta}} = \frac{3(Q_{tv} - Q_{pv})}{2\pi K_{rv} l_{rv}}\left(\frac{3V_{rv}}{\pi K_{rv} l_{rv}}\right)^{-\frac{1}{2}} \tag{4.33}$$

$$\frac{dr_{la}^{\alpha}}{dt^{\alpha}} = \frac{3(Q_{mv} - Q_{av})}{4\pi K_{la} l_{la}} \left(\frac{6V_{la}}{4\pi K_{la} l_{la}} \right)^{-\frac{1}{2}} \tag{4.34}$$

$$\frac{dr_{ra}^{\alpha}}{dt^{\alpha}} = \frac{3(Q_{tv} - Q_{pv})}{2\pi K_{ra} l_{ra}} \left(\frac{3V_{ra}}{\pi K_{ra} l_{ra}} \right)^{-\frac{1}{2}} \tag{4.35}$$

The fractional parameters α and β in (4.32) - (4.35) are obtained by formulating an optimization problem solved using CS, FA and APSO algorithms. The fractional derivatives α and β are obtained by minimizing the error index as an objective function with inequality constraints using heuristic algorithms.

4.6 Optimization Problem

The objective function is defined as:

$$J_{min} = \int_0^t e^2 dt \tag{4.36}$$

and is subjected to the following constraints:

$$max(P_{ao}) \leqslant 120mmHg \tag{4.37}$$

$$min(P_{ao}) \geqslant 70mmHg \tag{4.38}$$

where, P_{ao} is the arterial pressure and e is the error between the model output and clinical data of healthy human obtained from literature and physionet [67].

4.6.1 Fmincon() solver

For simulation, the fmincon() solver in MATLAB is used to find the optimized α. Different types of algorithms like Sequential Quadratic Programming (SQP), interior point, active-set, etc., are available in MATLAB. The given optimization problem is solved using SQP based algorithm. The detailed steps for execution of the fmincon() solver are given in Algorithm 4.1.

Algorithm 4.1: Fmincon() solver

Require: Objective function f(x)

Initialize error tolerance (ϵ), minimum and maximum limit of α, maximum iteration (T), select algorithm (SQP);

Generate initial condition, x(0) and Evaluate $f(x(0))$;

$t \leftarrow 0$;

while $t \leq T$ **do**

$t \leftarrow t + 1$;

Find new $x(t)$ and evaluate $f(x(t))$ along with constraints;

if $f(x(t)) < f(x(t-1))$ **then**

Find new $x(t)$ and evaluate $f(x(t))$ along with constraints;

end

if $f(x(t)) - f(x(t-1) < \epsilon$ **then**

Find new $x(t)$ and evaluate $f(x(t))$ along with constraints;

end

$t \leftarrow t + 1$;

end

Get the best solution

4.6.2 Heuristic Methods

In this section, a brief introduction about CS, FA and APSO heuristic algorithms are presented to solve the constrained optimization problem.

4.6.2.1 CS algorithm

The nature-inspired metaheuristic algorithm is used for finding the optimized α and β. This method mimics the breeding behavior of the cuckoo bird which uses the Levy flight mechanism to search nests and spawn. These birds lay eggs on other birds' nests. To increase the probability of their eggs getting hatched, these birds even remove the host eggs from the nest. This algorithm is developed based on the following idealized rules [68].

i At a time, each cuckoo bird lays only one egg and places it randomly in another bird's nest. This mathematically represents a solution

ii The nest with a high-quality egg is termed as the best nest and useful for the future generation. The best nest is replaced by a better solution in the next generation

iii The number of host nests (n) available for each generation is fixed. The probability of the host bird discovering a cuckoo egg is represented as p_a [0, 1]. The egg similar to the host bird only survives and becomes a mature cuckoo

Algorithm 4.2: CS algorithm

Require: Objective function f(x)
Initialize n, p_a and maximum iterations (T);
$t \leftarrow 0$;
for *i=1 to n* **do**
  Generate initial population of n host $x_i(t)$;
  Evaluate fitness $F(x_i(t))$;
end
while $t \leq T$ **do**
  Get a cuckoo randomly by Levy flight;
  Evaluate fitness $F(x_i(t))$ along with constraints;
  Choose a random nest among n (say j);
  if $F(x_i(t)) > F(x_j(t))$ **then**
    Replace j with new solution;
  end
  Worst nest is abondoned with a fraction of P_a ;
  New nests are built;
  Keep the best solutions;
  Rank the solutions;
  $t \leftarrow t + 1$;
end
Get the best solution

The objective function $f(x)$ given in this algorithm is replaced with the error index presented in (4.36). The required constraints given in (4.37) and (4.38) are incorporated in CS algorithm. The new solution is formed using the concept of Levy flight which is given by:

$$x_i(t+1) = x_i(t) + \mu \oplus L\acute{e}vy(\lambda), \tag{4.39}$$

where, μ is the step size, $\oplus$ means entrywise multiplication and λ is Levy distribution parameter. Levy flight simulates random walks where the step sizes follow levy distribution. The pseudo code of CS algorithm is presented in Algorithm 4.2.

4.6.2.2 FA

FA is also a metaheuristic algorithm that is inspired by the flashing behavior of the fireflies. For a particular species, the pattern of flashing is unique. They use this flashing behavior

to attract their mates. When a short, unique and rhythmic flash is identified by a suitable mate, it responds and moves toward each other. Hence, the luminous intensity increases. The inappropriate fireflies will move away resulting in increased distance and decreased attractiveness. This algorithm is developed based on the following idealized rules [4].

i Fireflies are unisex and hence they attract each other irrespective of their sex

ii The brightness between fireflies increases when the distance between them decreases. This is because the attractiveness is directly proportional to the brightness of the flash emitted by fireflies. For example, when we consider two flashing fireflies, the one with lesser brightness will approach the brighter one. However, they move randomly when they have identical brightness

Algorithm 4.3: FA

Require: Objective function f(x)
Initialize number of fireflies(n) μ, β_0, γ and maximum iterations (T);
Generate intial population of n fireflies;
$t \leftarrow 0$;
Evaluate light intensity $f(x_i(t))$ along with constraints;
while $t \leq T$ **do**
  for *i=1 to n* **do**
    for *j=1 to n* **do**
      if $I_j > I_i$ **then**
        Move firefly i towards j;
      end
      Evaluate new solution and update $f(x_i(t))$;
    end
  end
  Rank fireflies and find current best;
  $t \leftarrow t + 1$;
end
Get the best solution

From nature, it is observed that the brightness of a firefly is determined by the objective function $f(x)$. In this algorithm, $f(x)$ is replaced with the error index presented in (4.36). The required constraints given in (4.37) and (4.38) are incorporated in FA. In this process, the movement of i^{th} firefly is attracted by j^{th} brighter firefly and the new position is determined by:

$$x_i(t+1) = x_i(t) + \beta_0 e^{-\gamma r_{ij}^2}(x_j(t) - x_i(t)) + \mu_t \epsilon_i(t), \tag{4.40}$$

where, μ_t is the randomization parameter and $\epsilon_i(t)$ is a vector of random numbers drawn from a Gaussian or uniform distribution at time t. The parameter β_0 is the brightness of the firefly j at $r = 0$ and γ is a light absorption coefficient of the medium. Here, r is the Euclidean distance between fireflies and is given by:

$$r_{ij} = \sqrt{(x_i - x_j)^2}. \tag{4.41}$$

This algorithm is simple and easier to implement which leads to global search outcome. The pseudo code of FA is presented in Algorithm 4.3.

4.6.2.3 APSO algorithm

PSO is inspired by the flock of birds' social behavior of searching for food and the search strategy is to follow the bird which is nearest to the prey. Each particle in search space adjusts its flying according to its own and neighbor birds' flying experience [69]. To increase the diversity in the solutions, the standard PSO uses individual best along with global best. In APSO, only global best is used and the individual best calculation is avoided by introducing randomness in the initial guess. This makes the APSO algorithm more accurate and faster convergence [70].

Algorithm 4.4: APSO algorithm

Require: Objective function f(x);
$n \leftarrow$ population size;
Initialize n, T;
$t \leftarrow 0$;
while $t \leq T$ **do**
  for *i=1 to n* **do**
    Generate new velocity vectors;
    Calculate new position;
    Evaluate $f(x_i(t))$ along with constraints;
    Find current best;
  end
  Find current global best;
  $t \leftarrow t + 1$;
end
Get the best solution

In this algorithm, $f(x)$ is replaced with the error index presented in (4.36). The required constraints given in (4.37) and (4.38) are incorporated in APSO algorithm. Here,

the velocity vector is introduced to increase the speed of convergence toward the optimal solution. The updated velocity vector (v_i) is expressed as:

$$v_i(t+1) = v_i(t) + \lambda(g^* - x_i(t)) + \mu\epsilon_t, \tag{4.42}$$

where, λ and μ are the learning parameters or acceleration constants, g^* is the global best, $x_i(t)$ is the position of i^{th} particle at time t and ϵ_t is drawn from N(0, 1).

Hence the updated position is expressed as:

$$x_i(t+1) = x_i(t) + v_i(t+1). \tag{4.43}$$

The pseudo code of APSO algorithm is presented in Algorithm 4.4.

4.7 Results and Discussion

The detailed simulation is conducted for both IO and FO Windkessel and geometric models. The fractionality is obtained using fmincon() and heuristic methods like CS, FA and APSO algorithms.

4.7.1 Windkessel models

The detailed simulation is conducted for both IO and FO Windkessel models using the clinical data of flow rate as input and arterial pressure as output. The flow rate and pressure profiles of human used for optimization are extracted from the literature [71].

Remarks: In literature, the data shown in Figures 4.1 and 4.2 is acquired in the following procedure (i) eighteen patients are catheterized for various clinical indications. During rest and exercise no cardiovascular disease is found by hemodynamic measurements, left ventricular cine angiography or coronary arteriography and (ii) right and left heart catheterizations are performed using special multisensory catheters. Steady state conditions are determined by a stable heart rate and stable sequential pulmonary artery hemoglobin oxygen saturation measurements. The pressure and flow rate of these 18 patients are averaged and are shown in Figures 4.1 and 4.2 [71].

4.7.1.1 IO model

A detailed simulation is carried out for IO Wk2, Wk3 and Wk4 models. The optimization method in section 4.6 is used for finding the parameters R, C, r and L. The output pressure

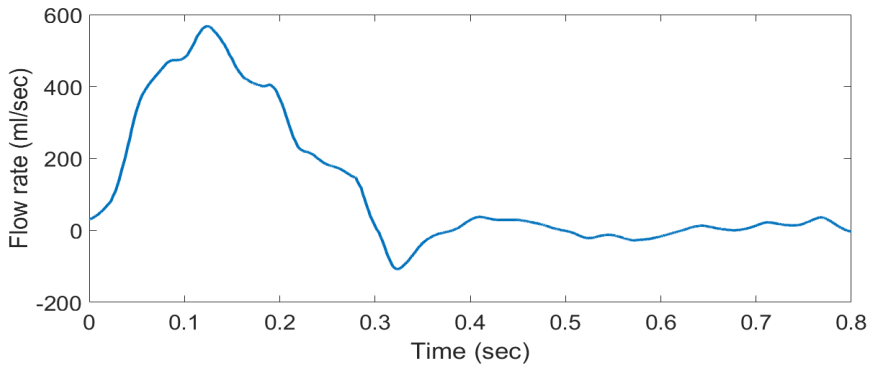

Figure 4.1: Input flow rate response of healthy human [2]

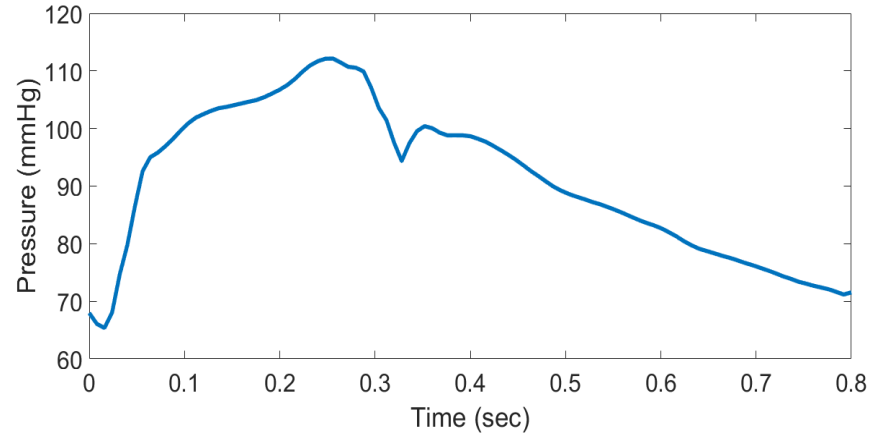

Figure 4.2: Output pressure profile of healthy human [2]

profile of the system is compared with the clinical output under normal conditions shown in Figure 4.2. The system parameters obtained for different Windkessel models are given in Table 4.1. The corresponding pressure profiles are shown in Figure 4.3. From the figure it is observed that the IO Wk4 model has better matching with the clinical data.

Table 4.1: System parameter for IO Windkessel models

Model	R	C	r	L	ISE
WK2	0.8	1.35	–	–	40.8569
WK3	0.79	1.75	0.033	–	15.8791
WK4	0.82	1.6	0.035	0.0005	10.1897

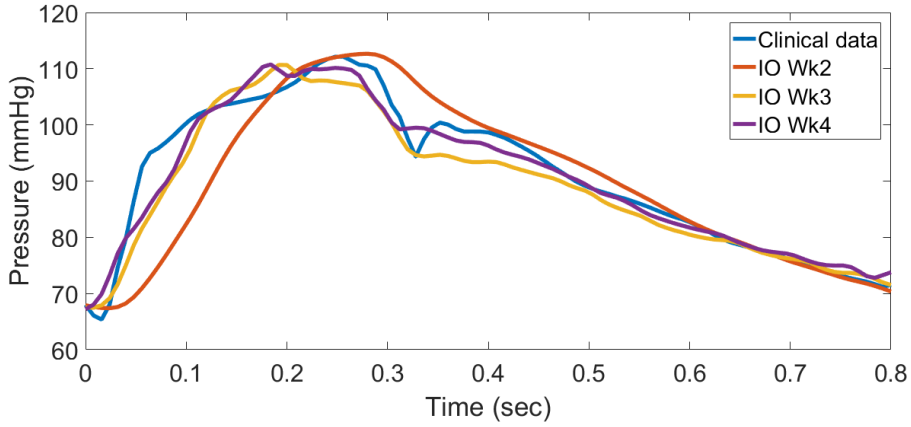

Figure 4.3: Pressure profiles of IO Wk2, Wk3 and Wk4 along with clinical data

4.7.1.2 FO model (Considering Only α)

The fractionality α in 4.29, 4.30 and 4.31 for FO Wk2, Wk3 and Wk4 are obtained using the optimization method. This is performed under the assumption that the system parameters are constant and shown in Table 4.1. Hence only α is the resulting unknown parameter obtained through optimization using the fmincon() solver. For optimization, the bounds for α are selected between 0 – 2. The optimization method provides α = 0.9469 for FO Wk2, α = 0.9880 for FO Wk3 and α = 0.9966 for FO Wk4. The convergence diagram of the α and objective function for the FO Wk2, Wk3 and Wk4 models are shown in Figures 4.4 and 4.5 respectively.

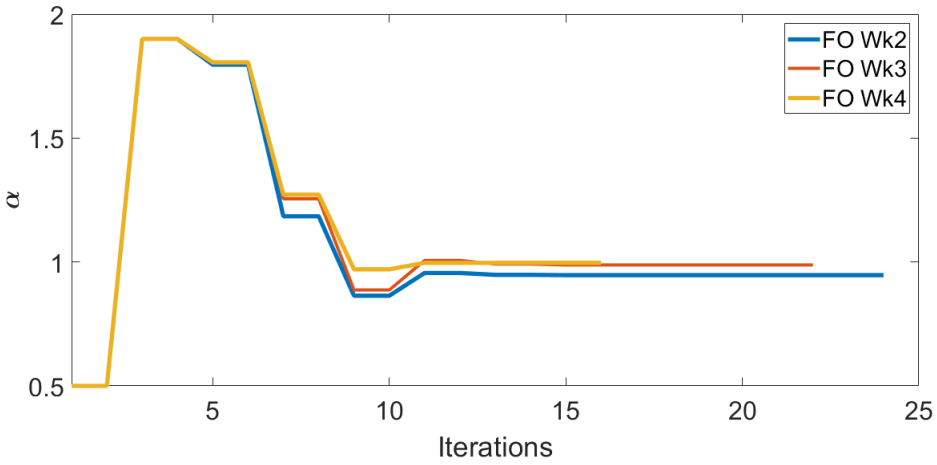

Figure 4.4: Convergence diagram of α for FO Wk2, Wk3 and Wk4 models (considering only α)

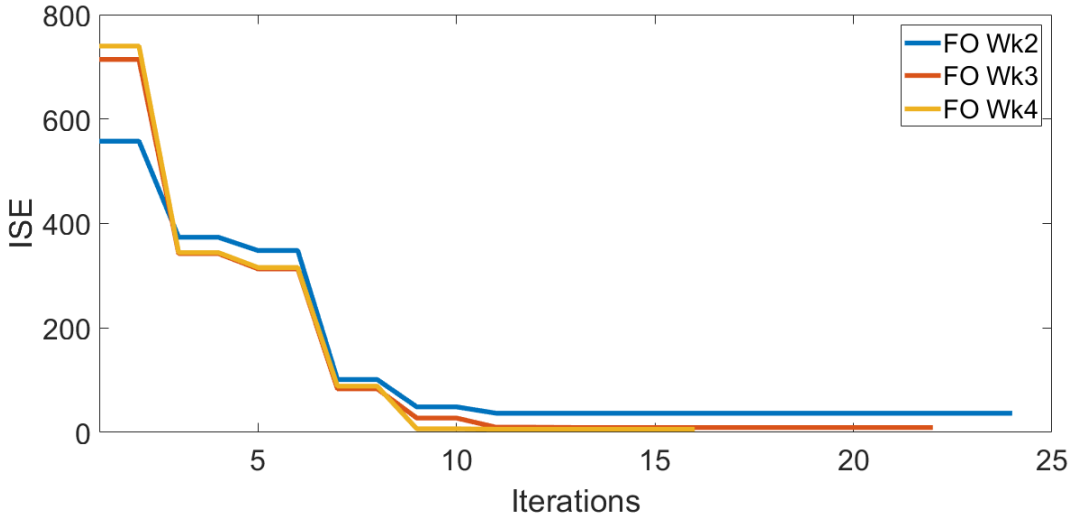

Figure 4.5: Convergence diagram of objective function for FO Wk2, Wk3 and Wk4 models (considering only α)

For FO Wk2, the converged output is observed after 24 iterations whereas the output is converged after 22 and 16 iterations for FO Wk3 and FO Wk4 models respectively. The Integral Square Error (ISE) computation given in Table 4.2 indicates that FO WK4 provides better ISE than FO Wk2 and WK3 models. The corresponding pressure profiles are shown in Figure 4.6 and it is observed that the FO model provides a response close to the IO counterpart.

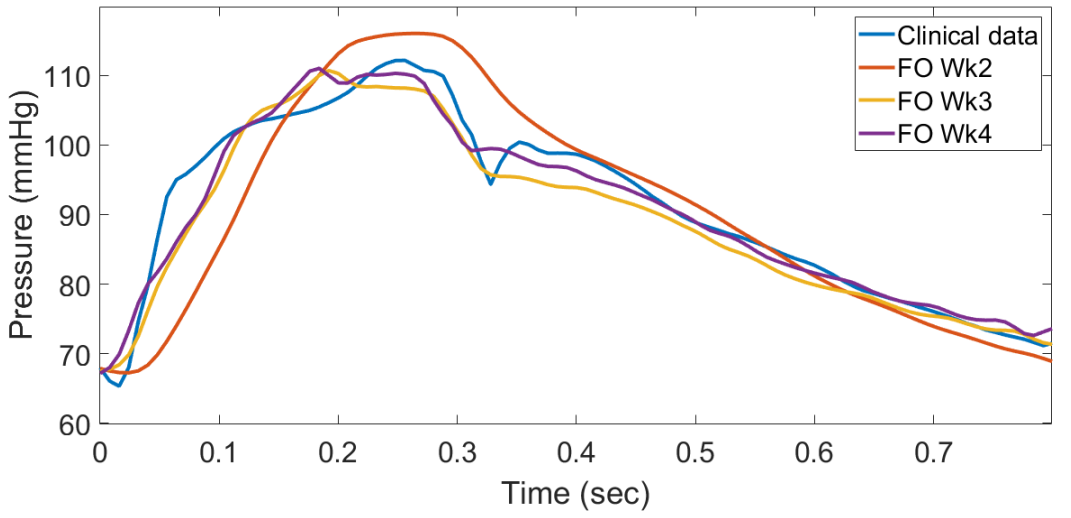

Figure 4.6: Pressure profiles for FO Wk2, Wk3 and Wk4 (considering only α) along with clinical data

Table 4.2: Error analysis for FO Wk2, Wk3 and Wk4 using only α

Model	Optimized α	ISE
FO Wk2	0.9469	36.5519
FO Wk3	0.9880	9.2587
FO Wk4	0.9966	6.0408

4.7.1.3 FO model (considering all parameters and α)

To improve the model accuracy, system parameters along with α are considered for optimization. The range of parameters used for optimization are $0.1 < R < 5$, $0.1 < C < 5$, $0 < r < 5$, $0 < L < 1$ and $0 < \alpha < 2$. The parameters R, C, r, L and α are obtained and listed in Table 4.3.

Table 4.3: Optimized parameters along with ISE for FO Wk2, Wk3 and Wk4 models (considering all parameters and α)

Models	α	R	C	r	L	ISE
FO Wk2	0.6830	1.3325	2.571	–	–	19.7664
FO Wk3	1.1024	0.7162	1.5546	0.0545	–	6.444
FO Wk4	1.2549	0.6114	1.3343	0.0927	0.0018	4.7324

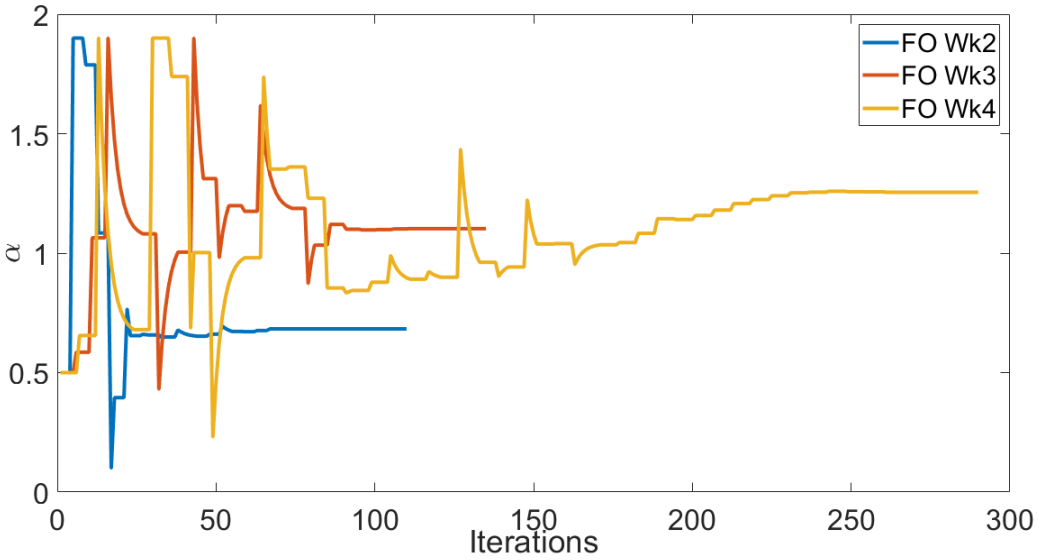

Figure 4.7: Convergence diagram of α for FO Wk2, Wk3 and Wk4 models (considering all parameters and α)

The convergence diagram for J_{min}, α, R and C are shown in Figures 4.7 – 4.10 respectively. For FO Wk2, the output is converged after 110 iterations whereas for FO Wk3 and FO Wk4 models, the output is converged after 140 and 290 iterations respectively. The arterial pressure response of FO Wk2, Wk3 and Wk4 along with clinical data are shown in Figure 4.11. It is observed from the Figure 4.11 and Table 4.3 that FO Wk4 provides the least error among other FO models.

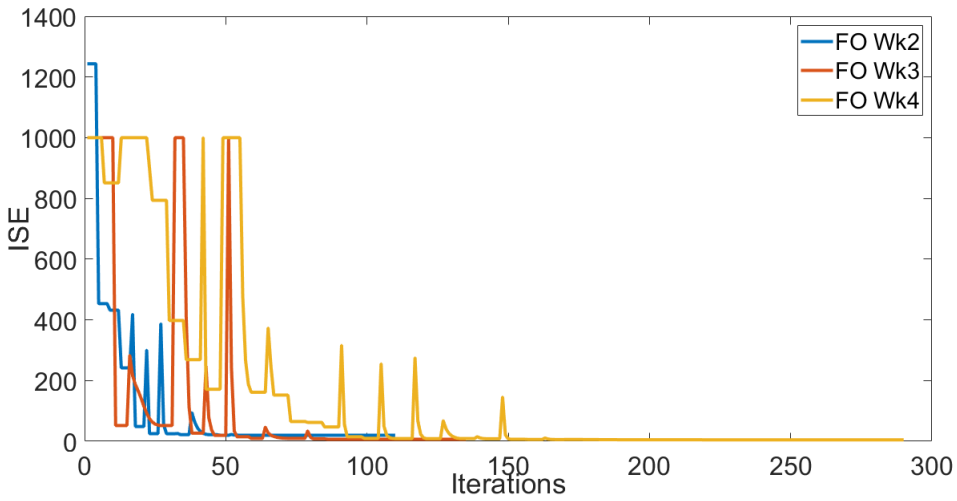

Figure 4.8: Convergence diagram of objective function for FO Wk2, Wk3 and Wk4 (considering all parameters and α)

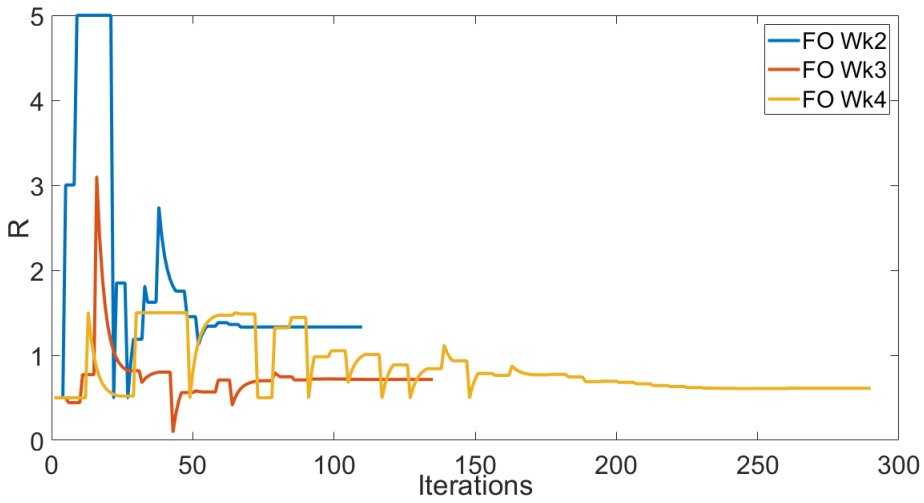

Figure 4.9: Convergence diagram of R for FO Wk2, Wk3 and Wk4 (considering all parameters and α)

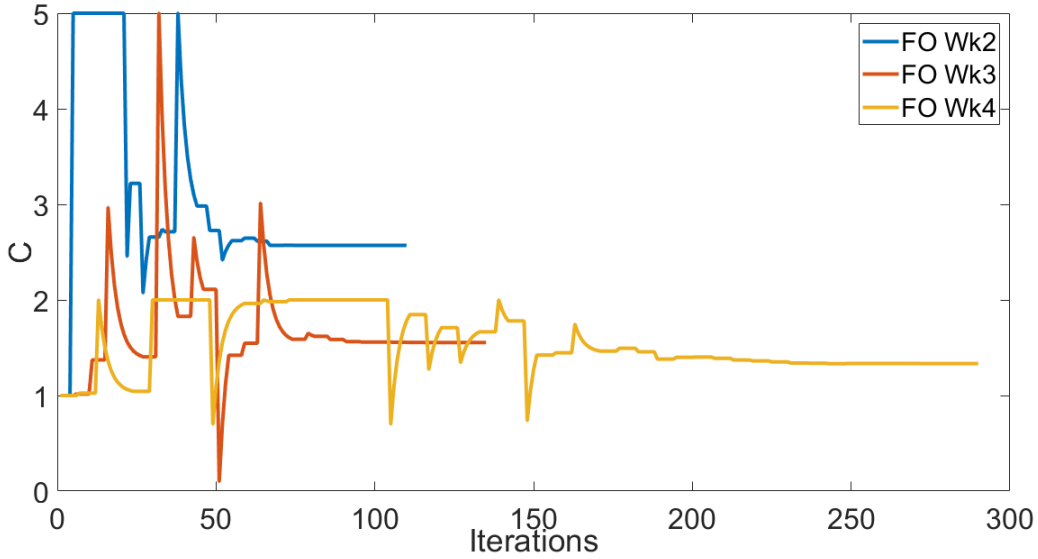

Figure 4.10: Convergence diagram of C for FO Wk2, Wk3 and Wk4 (considering all parameters and α)

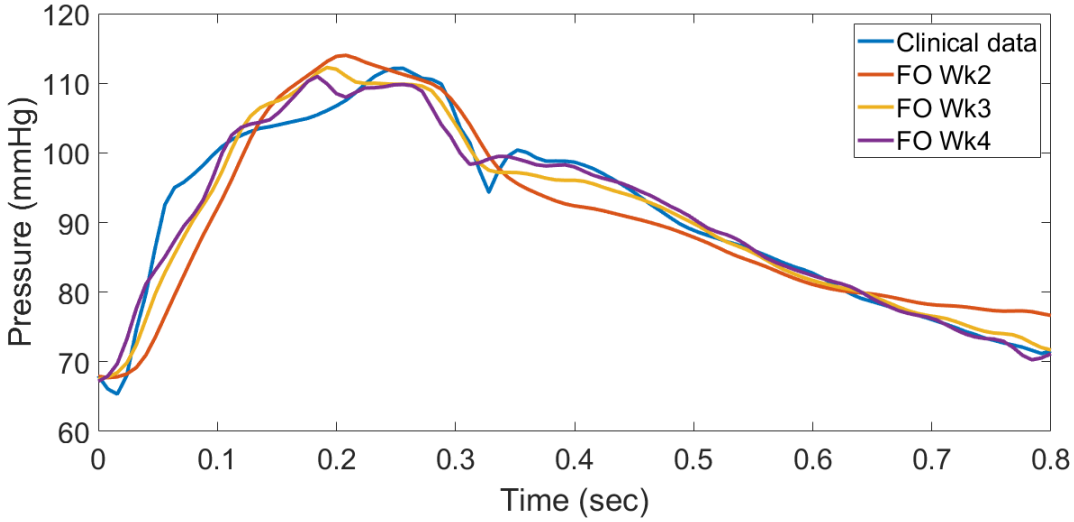

Figure 4.11: Pressure profiles for FO Wk2, Wk3 and Wk4 (considering all parameters and α) along with clinical data

4.7.1.4 Simulation study of abnormalities for Windkessel model

From the previous section, it is noted that the FO Wk4 model gives better closeness to the clinical data. Hence, the FO Wk4 model is further used for simulating diseases like

atherosclerosis and arterial stiffness. Atherosclerosis is the narrowing of arteries caused by cholesterol plaques (fat, calcium) lining the artery over time. This increases the resistance to the blood flow and can put blood flow at risk as arteries become blocked. Atherosclerosis begins with damage to the thin layer (endothelium) on the wall of arteries. This is simulated by changing the resistance in the FO Wk4 model. When the elastic property of the aorta decreases the stiffness of arteries to the blood flow increases. This increases the pressure inside the aorta. This condition is simulated by changing the capacitor of the FO Wk4 model. The corresponding pressure profiles with abnormalities are simulated and shown in Figure 4.12.

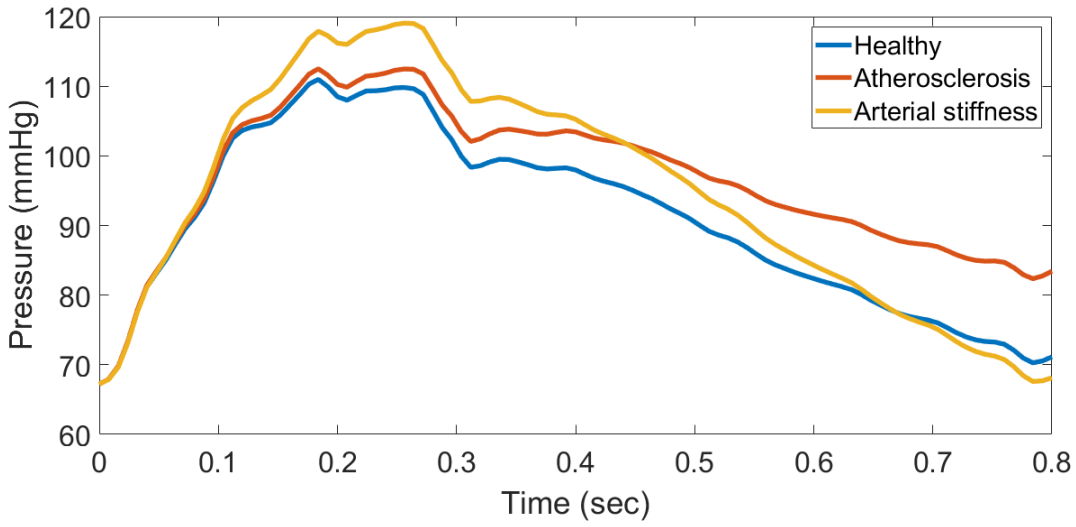

Figure 4.12: Simulated pressure profiles for atherosclerosis and arterial stiffness for FO Wk4 model

4.7.2 Geometric model

This section presents a detailed simulation of the proposed FO geometric model and existing IO geometric models for CVS. The system parameters considered for simulation are given in Table 4.4.

4.7.2.1 Existing IO model

The initial simulation is conducted using the existing IO model [3] under normal human health conditions. The corresponding steady-state pressure responses of four chambers along with aortic pressure are shown in Figure 4.13.

Table 4.4: System parameters for geometric model [3]

Parameter	Heart chambers			
	LV	RV	LA	RA
l(cm)	8	8	5.5	5.5
K	1.15	1.75	1.20	1.20
V_0(ml)	15	40	5	5
E_{es}(mmHg/mL)	2.5	1	-	-
A	1	1	-	-
B	0.02	0.02	-	-
E_{max}(mmHg/mL)	-	-	0.3	0.3
E_{min}(mmHg/mL)	-	-	0.2	0.2
T_1(s)	0.26	0.36	-	-
T_2(s)	0.36	0.36	-	-
T_a(s)	-	-	0.64	0.64
T(s)	0.8	0.8	0.8	0.8
D(s)	-	-	0.04	0.04

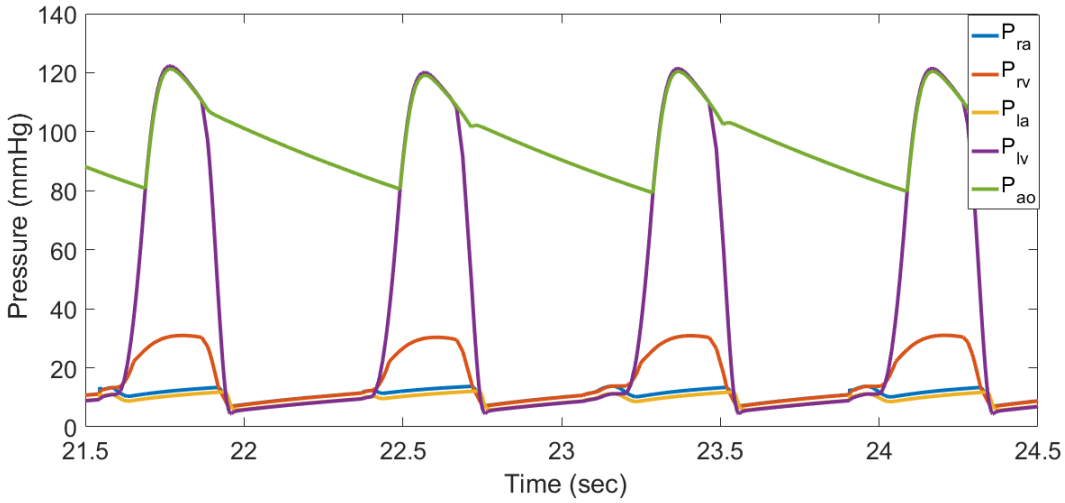

Figure 4.13: Pressure profile of IO model

To validate the model, the arterial pressure is compared with pressure data of healthy human [67] and plotted in Figure 4.14. It is observed that the aortic pressure of the simulated IO model deviates from the clinical data. To obtain better matching, FO models are introduced.

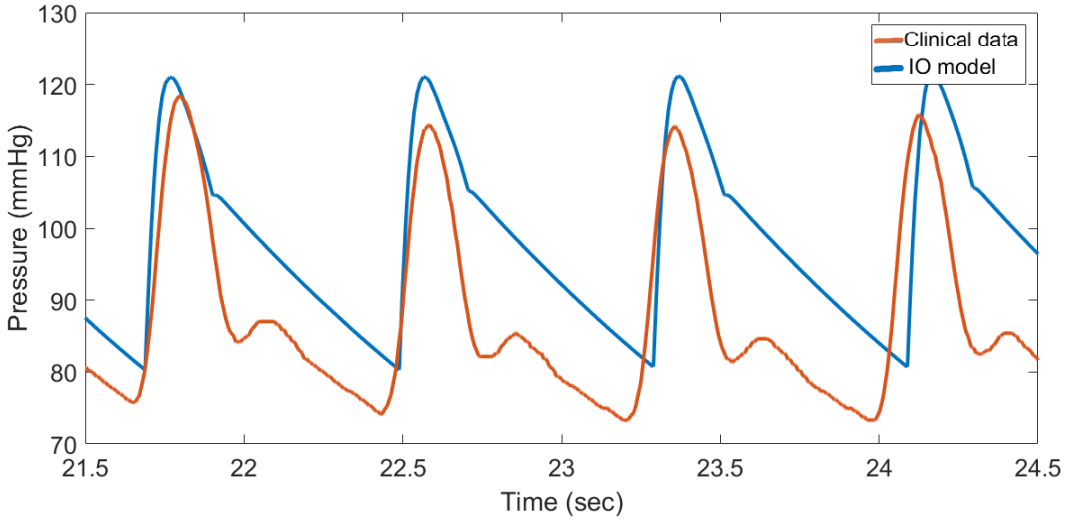

Figure 4.14: Arterial pressure profile of IO model along with clinical data

4.7.2.2 Proposed FO model ($\alpha = \beta$)

The fractional terms α and β are considered to frame the dynamical equation of four chambers. In general, RA, LA and LV have the same geometry and the corresponding differential equations are modeled with the same fractionality 'α'. Since the RV geometry is different from the other three chambers, the fractionality 'β' is used to represent the dynamical equation. During the initial design of the FO model, it is assumed that all the chambers have the same geometry and hence all the dynamical equations have the same fractionality (ie., $\alpha = \beta$).

For simulation, the system parameters presented in Table 4.4 are considered. The proposed optimization problem given in the section 4.6 is solved using heuristic methods for obtaining the fractionality given in (4.32) - (4.35). The fmincon() solver in MATLAB which utilizes the concept of SQP algorithm is used. The bounds for α are selected between 0 to 2 and the unique value of α is obtained through optimization as 0.8920 with ISE as 15.8923. Further CS, FA and APSO algorithms are used to obtain the optimum value of α. The parameter selections for the heuristic algorithms are given in Table 4.5.

4.7.2.2.1 CS algorithm The CS algorithm is used to provide the optimal α that results in minimum ISE. To get the optimal value of α, simulation is conducted for 100 different initial guesses with different p_a. The 10 best and closest minimum ISE along with the obtained optimized α are shown in Table 4.6. It is observed from the table that the value of $\alpha = 0.8970$ (highlighted in red color) provides the minimum ISE compared with other p_a.

Table 4.5: Parameter selection for CS, FA and APSO algorithms [4]

CS	FA	APSO
n=25	n=[1,100]	n=[1,100]
T= 200	T=200	T= 200
p_a = [0,1]	μ=0.3	γ=0.95
	β_0=0.3	
	γ=1	

The convergence diagram for the objective function and optimized α are shown in Figure 4.15.

Table 4.6: Optimized α for different p_a using CS algorithm

T	n	p_a	α	ISE
200	25	0.02	0.8970	15.9015
200	25	0.07	0.8945	16.0373
200	25	0.12	0.8875	16.2623
200	25	0.17	0.8953	16.0631
200	25	0.22	0.8934	15.9730
200	25	0.27	0.8915	16.4332
200	25	0.32	0.8892	16.3566
200	25	0.37	0.8966	15.9661
200	25	0.42	0.8912	16.4793
200	25	0.47	0.8951	15.9857

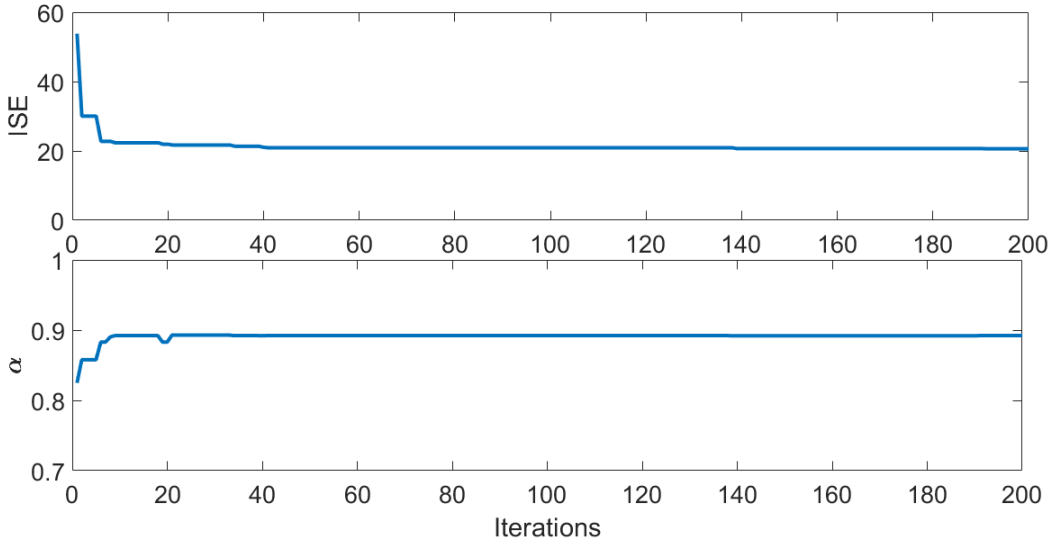

Figure 4.15: Convergence diagram of objective function and α for CS

4.7.2.2.2 FA The simulations are carried out by considering the parameters given in Table 4.5. To obtain the best α, simulation is conducted for 100 different initial guesses with different n. The 10 best and closest minimum ISE along with the obtained optimized α are shown in Table 4.7. It is noted that $\alpha = 0.8956$ (highlighted in red color) provides the least ISE compared with other ISE listed in Table 4.7. The convergence diagram for the objective function and the optimized value of α are shown in Figure 4.16.

Table 4.7: Optimized α for different n using FA

T	n	μ	β_0	γ	α	ISE
200	10	0.3	0.3	1	0.8933	15.7389
200	20	0.3	0.3	1	0.8964	15.7870
200	30	0.3	0.3	1	0.8912	16.0990
200	40	0.3	0.3	1	0.8956	15.5982
200	50	0.3	0.3	1	0.8881	15.9392
200	60	0.3	0.3	1	0.8965	15.7877
200	70	0.3	0.3	1	0.8936	15.9688
200	80	0.3	0.3	1	0.8919	15.9591
200	90	0.3	0.3	1	0.8934	15.5544
200	100	0.3	0.3	1	0.8911	16.0869

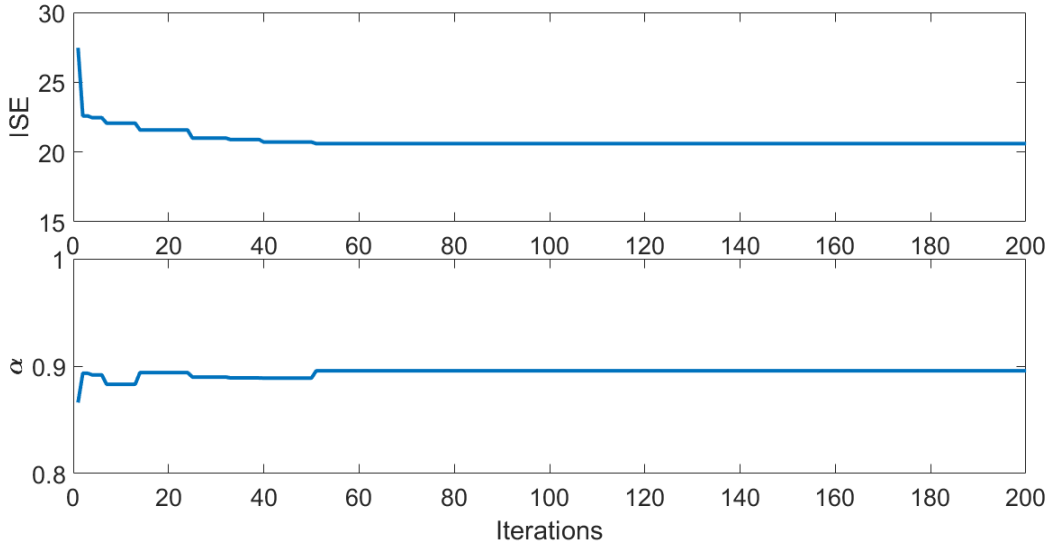

Figure 4.16: Convergence diagram of objective function and α for FA

4.7.2.2.3 APSO algorithm The simulations are performed by considering the APSO parameters given in Table 4.5. To obtain the best α, simulation is conducted for 100 different initial guesses with different n. The 10 best and closest minimum ISE along with the

obtained α are shown in Table 4.8. It is seen that $\alpha = 0.8989$ (highlighted in red color) indicates the least ISE compared with other ISE given in Table 4.8. The convergence diagram for the objective function and the optimized α are shown in Figure 4.17.

Table 4.8: Optimized α for different n using APSO algorithm

T	n	γ	α	ISE
200	10	0.95	0.8971	16.0588
200	20	0.95	0.9056	16.9299
200	30	0.95	0.8886	16.1706
200	40	0.95	0.8926	16.6504
200	50	0.95	0.8909	16.2229
200	60	0.95	0.8966	16.4236
200	70	0.95	0.8935	15.8275
200	80	0.95	0.8973	16.3096
200	90	0.95	0.8989	15.8108
200	100	0.95	0.8972	15.9631

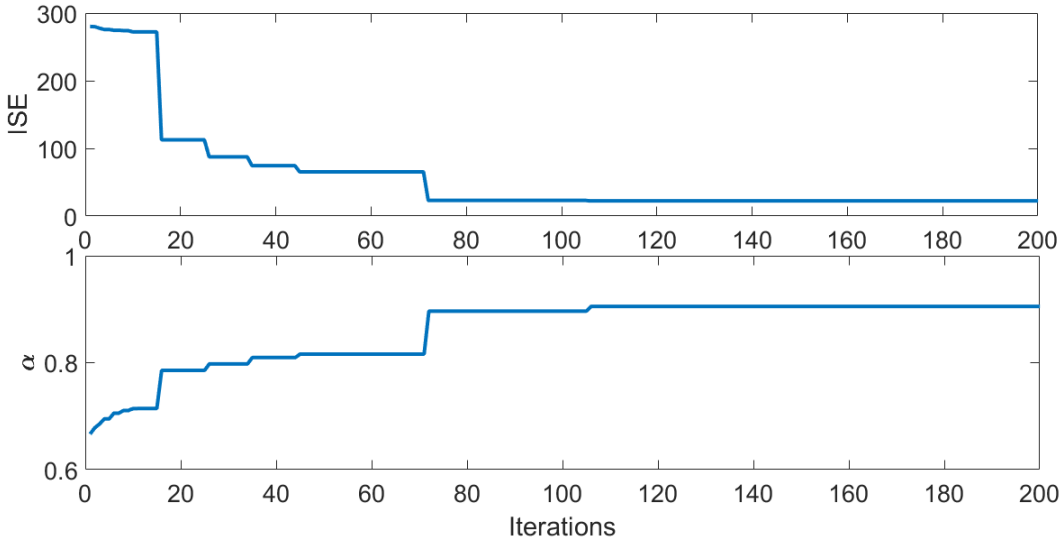

Figure 4.17: Convergence diagram of objective function and α for APSO

4.7.2.3 Comparative Analysis

Further, the comparative analysis is performed with the obtained optimal α using CS, FA, APSO, fmincon() solver and IO models. The corresponding pressure profiles along with clinical data of healthy human are shown in Figure 4.18. For more clarity, one cycle of the pressure profile is extracted from the steady state and shown in Figure 4.19.

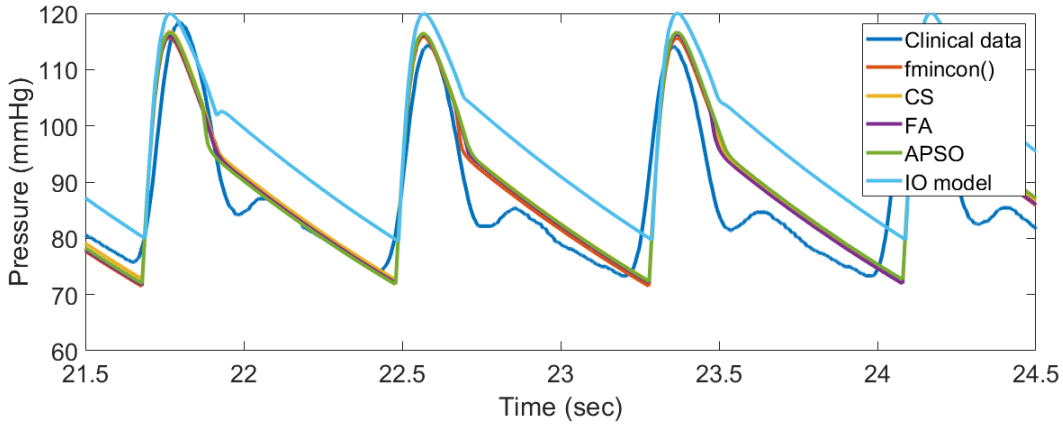

Figure 4.18: Arterial pressure profiles for optimized α using different optimization methods along with IO and clinical data

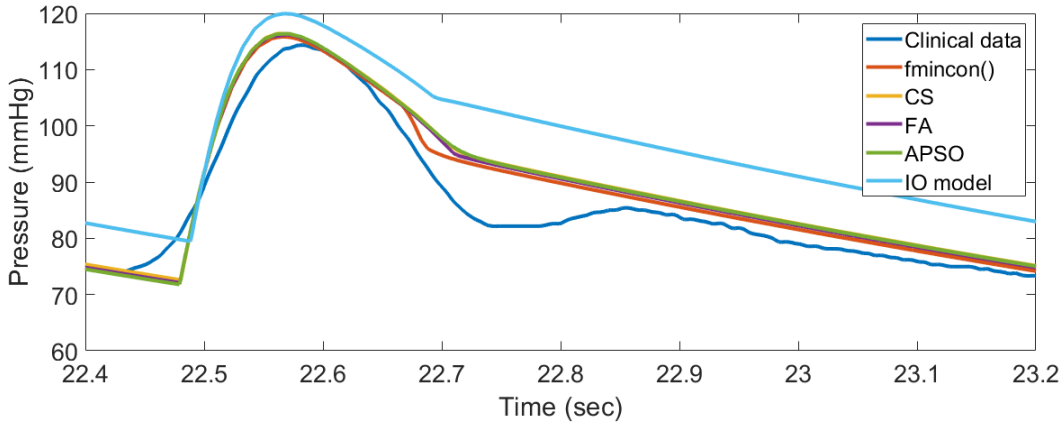

Figure 4.19: Arterial pressure profiles for optimized α using different optimization methods along with IO and clinical data (one cycle at steady state)

It is observed that the responses obtained from CS, FA, APSO and fmincon() are close to each other. Hence to show the best α among these algorithms, the performance index (ISE) and statistical indices [Mean and Standard Deviation (SD)] are computed and shown in Table 4.9. From the table, it is observed that the α obtained using FA algorithm provides 95.768 % reduction in the ISE of FO model compared to IO model. From these results, it is concluded that the fractionality ($\alpha = 0.8956$) obtained using FA provides minimum ISE, Mean and SD than other algorithms.

Table 4.9: Error and statistical analysis for CS, FA and APSO algorithms (considering only α)

Algorithm	α	ISE	Statistical index	
			Mean	SD
IO model	1	368.5730	-	-
CS	0.8970	15.9015	0.8932	0.0030
FA	0.8956	15.5982	0.8931	0.0025
APSO	0.8989	15.8108	0.8958	0.0040

4.7.2.4 FO model (considering both α and β)

As it is indicated in the previous section that RV geometry is different from the other three chambers, the fractionality β is preferred. Hence the simulation is performed with α for LV, LA and RA and β for RV. For this simulation, $\alpha = 0.8956$ is considered from the initial study ($\alpha = \beta$) and hence only β is optimized. The fmincon() solver in MATLAB is used for finding the optimal value of β. The bounds for β are selected between 0 to 2 and the unique value is obtained through optimization as 0.9689 with ISE = 15.8132.

4.7.2.4.1 CS algorithm The CS algorithm is used to provide the optimal β that results in minimum ISE. To get the optimal value of β, simulation is conducted for 100 different initial guesses with different p_a. The 10 best and closest minimum ISE along with the obtained β are shown in Table 4.10. It is noted from the table that the value of $\beta = 0.9633$ (highlighted in red color) provides minimum ISE. The convergence diagram for the objective function and β for the optimized value are shown in Figure 4.20.

Table 4.10: Optimized β for different p_a using CS algorithm

T	n	p_a	β	ISE
200	25	0.1	0.9961	16.0427
200	25	0.2	0.9647	15.8389
200	25	0.3	0.9877	15.9376
200	25	0.4	0.9633	15.7014
200	25	0.5	1.0028	16.0353
200	25	0.6	0.9605	16.8353
200	25	0.7	1.0079	16.4969
200	25	0.8	0.9716	15.7944
200	25	0.9	1.0086	16.1165
200	25	0.99	0.9713	16.2953

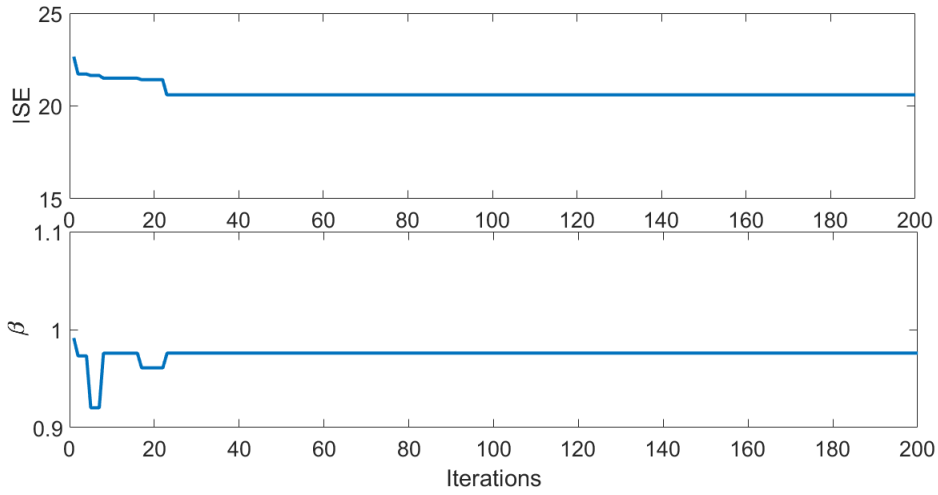

Figure 4.20: Convergence diagram of objective function and β for CS algorithm

4.7.2.4.2 FA The simulations are carried out by considering the parameters given in Table 4.5 for FA. To obtain the best β, simulation is conducted for 100 different initial guesses with different n. The 10 best and closest minimum ISE values along with the obtained β are shown in Table 4.11. It is noted that $\beta = 0.9818$ (highlighted in red color) provides the least ISE compared with other ISE listed in Table 4.11. The convergence diagram for the objective function and β for the optimized value are shown in Figure 4.21.

Table 4.11: Optimized β for different n using FA

T	**n**	μ	β_0	γ	β	**ISE**
200	10	0.3	0.3	1	0.9519	16.1894
200	20	0.3	0.3	1	0.9696	16.0238
200	30	0.3	0.3	1	0.9537	15.7810
200	40	0.3	0.3	1	0.9818	15.3154
200	50	0.3	0.3	1	0.9879	15.7236
200	60	0.3	0.3	1	0.9597	15.6689
200	70	0.3	0.3	1	0.9661	15.5506
200	80	0.3	0.3	1	0.9701	15.5606
200	90	0.3	0.3	1	0.9410	15.9819
200	100	0.3	0.3	1	0.9836	15.3230

4.7.2.4.3 APSO algorithm The simulations are performed by considering the APSO parameters given in Table 4.5. To obtain the best β, simulation is performed for 100 different initial guesses with different n. The 10 best and closest minimum ISE along with the

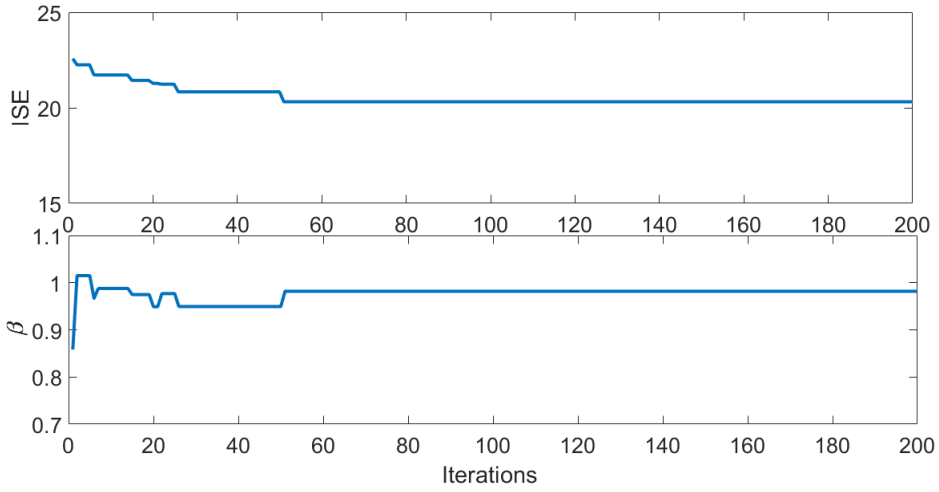

Figure 4.21: Convergence diagram of objective function and β for FA

obtained β are shown in Table 4.12. It is seen that $\beta = 0.9722$ (highlighted in red color) indicates the least ISE compared with other ISE listed in Table 4.12. The convergence diagram for the objective function and β for the optimized value are shown in Figure 4.22.

Table 4.12: Optimized β for different n using APSO algorithm

T	n	γ	β	ISE
200	10	0.95	0.9808	15.5239
200	20	0.95	0.9776	15.5351
200	30	0.95	0.9448	15.6055
200	40	0.95	0.9631	15.5188
200	50	0.95	1.0199	15.9376
200	60	0.95	0.9517	15.5135
200	70	0.95	0.9722	15.3913
200	80	0.95	0.9885	15.8483
200	80	0.95	0.9668	15.5661
200	100	0.95	0.9790	15.6802

4.7.2.5 Comparative analysis

Further, a comparative analysis is performed with the obtained optimal α and β of FO model using CS, FA, APSO, fmincon() algorithms and IO model. The corresponding pressure profiles along with clinical data are shown in Figure 4.23.

For more clarity, one cycle of the pressure profiles are extracted from the steady-state and shown in Figure 4.24. It is observed that the responses obtained from CS, FA, APSO

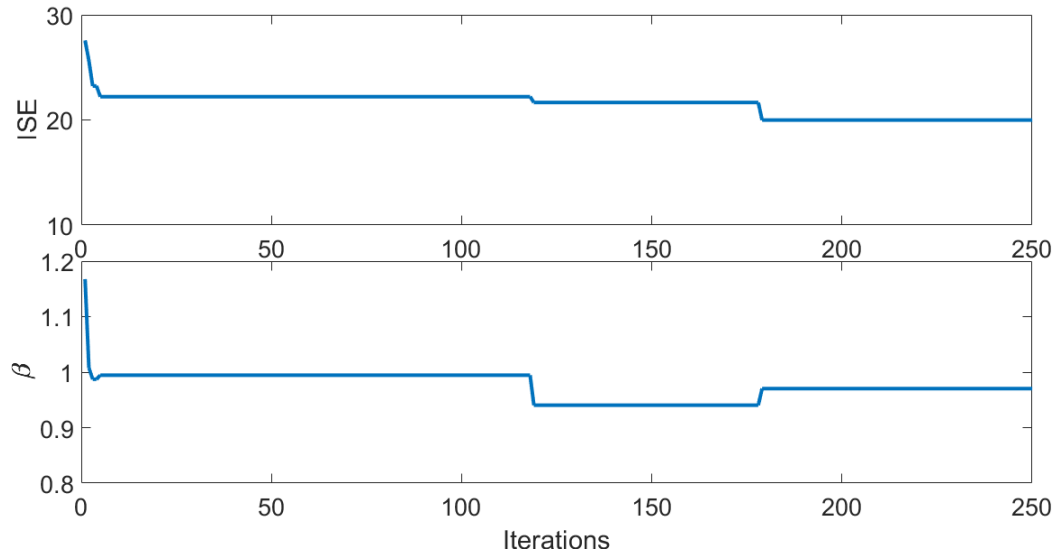

Figure 4.22: Convergence diagram of objective function and β for APSO algorithm

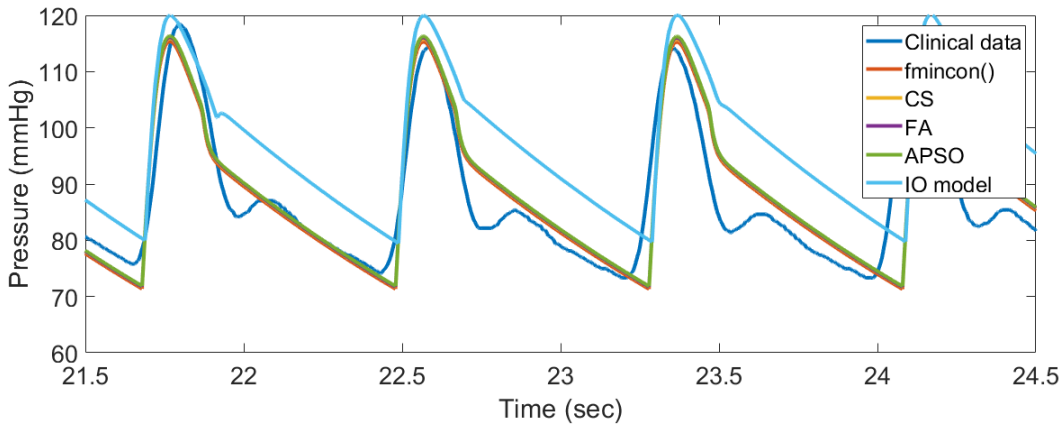

Figure 4.23: Arterial pressure profiles for optimized α and β using different optimization methods along with IO and clinical data

and fmincon() are close to each other. Hence to show the best result among these algorithms, ISE and statistical indices (Mean and SD) are computed and shown in Table 4.13. The results indicate that the fractionality β = 0.9818 (with α = 0.8956) obtained using FA provides minimum ISE, mean and SD than other algorithms. From Table 4.13, it is observed that the α and β obtained using FA algorithm provides 95.845% reduction in the ISE of FO model compared to IO model. Hence, this model is further used for simulating abnormalities like arterial stiffness and atherosclerosis.

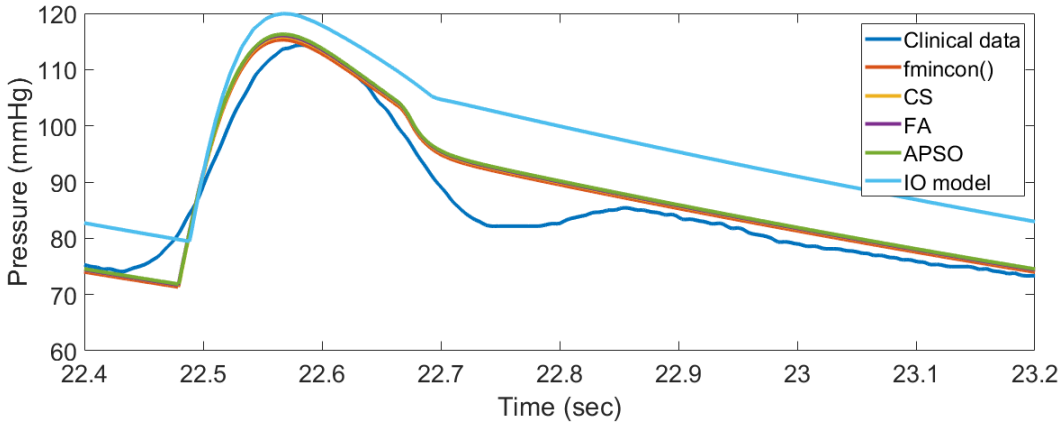

Figure 4.24: Arterial pressure profiles for optimized α and β using different optimization methods along with IO and clinical data (one cycle at steady state)

Table 4.13: Error and statistical analysis for CS, FA and APSO algorithms (considering both α and β)

Algorithm	α	β	**ISE**	**Statistical index**	
				Mean	**SD**
IO model	1	1	368.5730	-	-
CS	0.8970	0.9633	15.7014	0.9890	0.0186
FA	0.8956	0.9818	15.3154	0.9646	0.0146
APSO	0.8989	0.9722	15.3913	0.9744	0.0233

4.7.2.6 Simulation study of abnormalities for geometric model

The heart abnormalities (i) arterial stiffness and (ii) atherosclerosis are simulated and results are compared with the healthy human condition. In general, the gradual fragmentation and loss of elastin fibers and accumulation of stiffer collagen fibers in the arterial wall reduces elasticity and hence increases the stiffness. This leads to hypertension and other closely associated diseases. This condition is simulated by introducing a change in the capacitance of aorta.

On the other hand, atherosclerosis is the buildup of fats, cholesterol and other substances on the artery walls which blocks the blood flow. This abnormality is simulated by increasing the peripheral resistance of the aorta. The corresponding arterial blood pressure responses along with healthy human condition are shown in Figure 4.25. This indicates that the proposed FO model can be useful for simulating various abnormal conditions of

CVS.

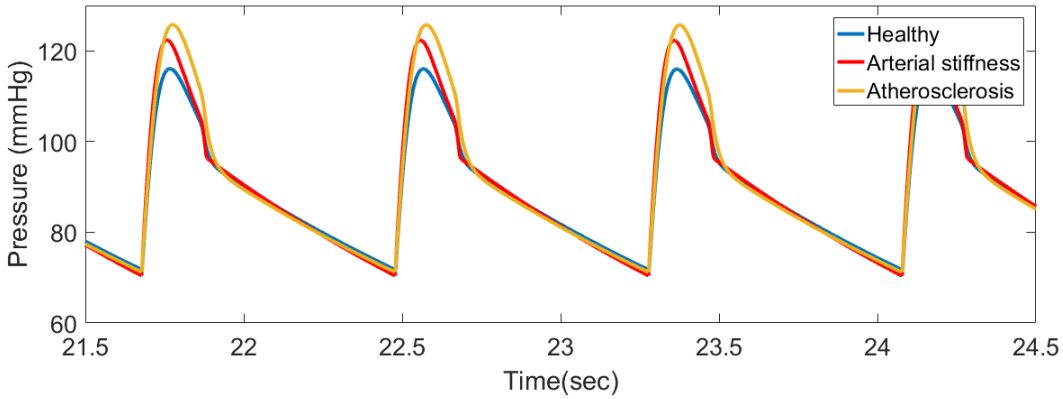

Figure 4.25: Arterial pressure profiles during abnormalities for FO geometric model

4.8 Summary

The FO Windkessel models are presented and the corresponding parameters are obtained using SQP optimization technique. For the initial simulation, only IO Windkessel models are considered. To improve the accuracy, the viscoelasticity property is enhanced by introducing the FO derivative in the existing IO Windkessel models. The simulations are carried out for optimizing (i) only α and (ii) system parameters along with α.

From the results, it is noted that FO Windkessel models provide better accuracy than IO models. In specific, the FO Wk4 model gives better accuracy in comparison with FO Wk2 and Wk3 models. Further FO Wk4 model is used for simulating atherosclerosis and arterial stiffness conditions.

Also, a geometric FO model is developed by introducing fractionality to the dynamical equations to accommodate the viscoelastic property of CVS. A constrained optimization problem is framed to obtain the fractional parameters by minimizing the pressure error between FO model and clinical data of healthy human using CS, FA and APSO and the results are compared with SQP algorithm. Initial simulation is carried out by considering the fractional parameter α for all chambers. The further simulation is performed by considering α for LV, LA, RA and β for RV. The ISE obtained through different optimization algorithms are compared and it is observed that α and β obtained through FA provided the least ISE, mean and SD. The best optimized α and β obtained from FA are further used for simulating the abnormalities (i) arterial stiffness and (ii) atherosclerosis.

Chapter 5

Baroreflex control for FO Geometric model

5.1 Introduction

This chapter deals with the design of the baroreceptor control mechanism for FO geometric model. The baroreflex control system plays a crucial role in responding to acute changes in blood pressure, such as those caused by factors like physical activity, stress, and changes in posture. It ensures that vital organs receive a consistent supply of oxygen and nutrients while adapting to various physiological conditions and external influences. The baroreflex is essential for maintaining overall cardiovascular health and homeostasis. In Chapter 3, the baroreflex control is designed for an extended IO Windkessel model in which both the atria and two valves are neglected. Also, pulmonary and systemic circulations are modeled using a single Windkessel compartment. However, it is essential to have a model which includes all the chambers and valves which mimic the CVS more accurately. Hence, a baroreflex control is designed for the FO geometric model explained in Chapter 4 extends to all the chambers along with more compartments for systemic and pulmonary circulation which in turn increases the accuracy and reliability of the CVS model.

5.2 FO CVS Model

The mathematical model represented in Section 4.5 is used to design the baroreflex control in which the heart chambers are modeled using FO differential equations.

The corresponding FO equations for LV, RV, LA and RA are expressed as:

$$\frac{dr_{lv}^{0.8956}}{dt^{0.8956}} = \frac{3(Q_{mv} - Q_{av})}{4\pi K_{lv} l_{lv}} \left(\frac{6V_{lv}}{4\pi K_{lv} l_{lv}} \right)^{-\frac{1}{2}} \tag{5.1}$$

$$\frac{dr_{rv}^{0.9818}}{dt^{0.9818}} = \frac{3(Q_{tv} - Q_{pv})}{2\pi K_{rv} l_{rv}} \left(\frac{3V_{rv}}{\pi K_{rv} l_{rv}} \right)^{-\frac{1}{2}} \tag{5.2}$$

$$\frac{dr_{la}^{0.8956}}{dt^{0.8956}} = \frac{3(Q_{mv} - Q_{av})}{4\pi K_{la} l_{la}} \left(\frac{6V_{la}}{4\pi K_{la} l_{la}} \right)^{-\frac{1}{2}} \tag{5.3}$$

$$\frac{dr_{ra}^{0.8956}}{dt^{0.8956}} = \frac{3(Q_{tv} - Q_{pv})}{2\pi K_{ra} l_{ra}} \left(\frac{3V_{ra}}{\pi K_{ra} l_{ra}} \right)^{-\frac{1}{2}} \tag{5.4}$$

The pressure volume expressions are same of the FO geometric model in Section 4.5. The relation between pressure and radius of LV is expressed as:

$$\begin{aligned} P_{lv}(t) = E_{es-lv} \left[\frac{2}{3} \pi K_{lv} l_{lv} \left(r_{lv}^2 - r_{lv-0}^2 \right) \right] f_{act-lv}(t) \\ + \left[\left(A e^{\frac{1}{6} B \pi K_{lv} r_{lv}(t)^2 l_{lv}} \right) - 1 \right], \end{aligned} \tag{5.5}$$

where, f_{act-lv} is the sinusoidal activation function for LV.

For IO and FO geometric models, the activation function is independent of heart rate. Hence, the pressure and volume are also independent of heart rate. In the previous simulation studies, due to the absence of baroreflex control, the heart rate is maintained constant. The realistic anatomy of heart shows that the pressure and volume vary with respect to heart rate. This is important when the baroreflex control is introduced to the FO model. The baroreflex control mechanism changes heart rate when there is a change in pressure occurs. To incorporate this, a variable heart rate activation function is used [72]. The activation function is expressed as:

$$f_{act-lv} = \begin{Bmatrix} sin^2 \frac{\pi . T(t)}{T_{sys}(t)} u & 0 \leq u \leq T_{sys}(t) \\ 0 & \frac{T_{sys}(t)}{T} \leq u \leq 1 \end{Bmatrix} \tag{5.6}$$

where, $T_{sys}(t)$ is systolic time, T is the time period and $u = frac(\int \frac{1}{T} dt)$

The activation function is varying with heart rate which is function of time period. The baroreflex control changes the heart rate in turn update the activation function.

5.3 Baroreflex Control Design

The FO CVS model is non linearly controlled by the baroreceptors situated near the sinus node and it consists of afferent dynamics, a processing unit to process firing rate into tones and the efferent dynamics from ANS to the control parameters. The baroreflex regulatory

system is a short term blood pressure control and for long term control hormonal activities are involved. Baroreflex control presented in Chapter 3 is extended to FO geometric model discussed in Chapter 4. Since the number of chambers are more, the control action has to go to the parameter in every chamber. The efferent dynamics refers to how the parameters are controlled by tones chemically [57]. The inotropic and chronotropic effects presented in Chapter 3 are updated and as follows:

$$\frac{d}{dt}H = \frac{1}{\tau_H}\left(-H + \alpha_H T_s - \beta_s T_p + \gamma_H\right) \tag{5.7}$$

$$\frac{d}{dt}E_{lv} = \frac{1}{\tau_{E_{lv}}}\left(-E_{lv} + \alpha_{E_{lv}} T_s + \gamma_{E_{lv}}\right) \tag{5.8}$$

$$\frac{d}{dt}E_{rv} = \frac{1}{\tau_{E_{rv}}}\left(-E_{rv} + \alpha_{E_{rv}} T_s + \gamma_{E_{rv}}\right) \tag{5.9}$$

$$\frac{d}{dt}R_{as} = \frac{1}{\tau_{R_{as}}}\left(-R_{as} + \alpha_{R_{as}} T_s + \gamma_{R_{as}}\right) \tag{5.10}$$

$$\frac{d}{dt}C_{as} = \frac{1}{\tau_{C_{as}}}\left(-C_{as} + \beta_{C_{as}} T_p + \gamma_{C_{as}}\right) \tag{5.11}$$

$$\frac{d}{dt}R_{ao} = \frac{1}{\tau_{R_{ao}}}\left(-R_{ao} + \alpha_{R_{ao}} T_s + \gamma_{R_{ao}}\right) \tag{5.12}$$

$$\frac{d}{dt}C_{ao} = \frac{1}{\tau_{C_{ao}}}\left(-C_{ao} + \beta_{C_{ao}} T_p + \gamma_{C_{ao}}\right) \tag{5.13}$$

where, τ_H, $\tau_{E_{rv}}$, $\tau_{E_{lv}}$, $\tau_{R_{as}}$, $\tau_{C_{as}}$, $\tau_{R_{ao}}$ and $\tau_{C_{ao}}$ are the time constant for the control parameters H, E_{rv}, E_{lv}, R_{as}, C_{as}, R_{ao}, C_{ao} respectively. α_H, $\alpha_{E_{rv}}$, $\alpha_{E_{lv}}$, $\alpha_{R_{as}}$ and $\alpha_{R_{ao}}$ are parameters that determine the amount of control by the sympathetic tones. β_H, $\beta_{C_{as}}$ and $\beta_{C_{ao}}$ are parameters that determine the amount of control by the parasympathetic tones and γ_H, $\gamma_{E_{rv}}$, $\gamma_{E_{lv}}$, $\gamma_{R_{as}}$, $\gamma_{C_{as}}$, $\gamma_{R_{ao}}$ and $\gamma_{C_{ao}}$ are the value of the control parameters under complete denervation.

The heart rate is controlled by both sympathetic and parasympathetic tones. To study the proposed model, a disturbance is introduced to the systemic vein as the positional change from supine to standing.

5.4 Results and Discussion

To show the superiority of the proposed model, simulation is performed for (i) Postural change (ii) orthostatic intolerance (iii) hemorrhage conditions and (iv) atherosclerosis and arterial stiffness.

5.4.1 Postural change

To validate the model, a postural change is introduced at time t=60 sec by adding disturbance to the venous pressure. During the postural change from supine to standing, blood pools to the lower part of the body and as a result the arterial pressure reduces. The venous pressure increases because of the increase in blood volume in the veins due to the effect of gravity which in turn reduces MAP, firing activity and venous compliance. The circulation loop continues to work with the reduced blood pressure in the absence of baroreflex control.

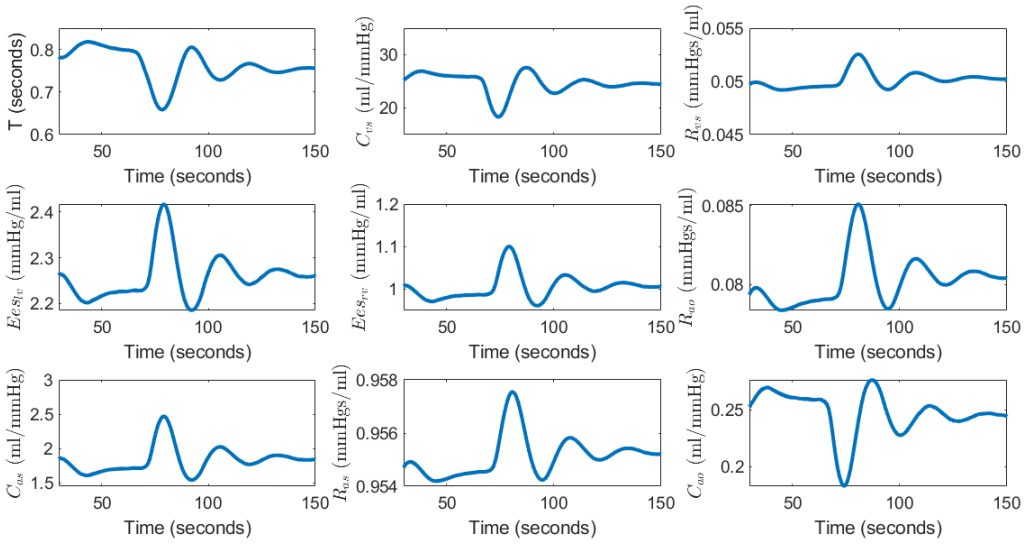

Figure 5.1: Responses of parameter variations with postural change at t=60 sec

The baroreflex control mechanism senses the reduction in pressure and changes the elastance, resistance, compliance and cardiac period. The resistance and elastance of the compartment increase and the compliance and cardiac period decrease as shown in Figure 5.1. As a result the arterial pressure also increases and reaches the nominal value as shown in Figure 5.2.

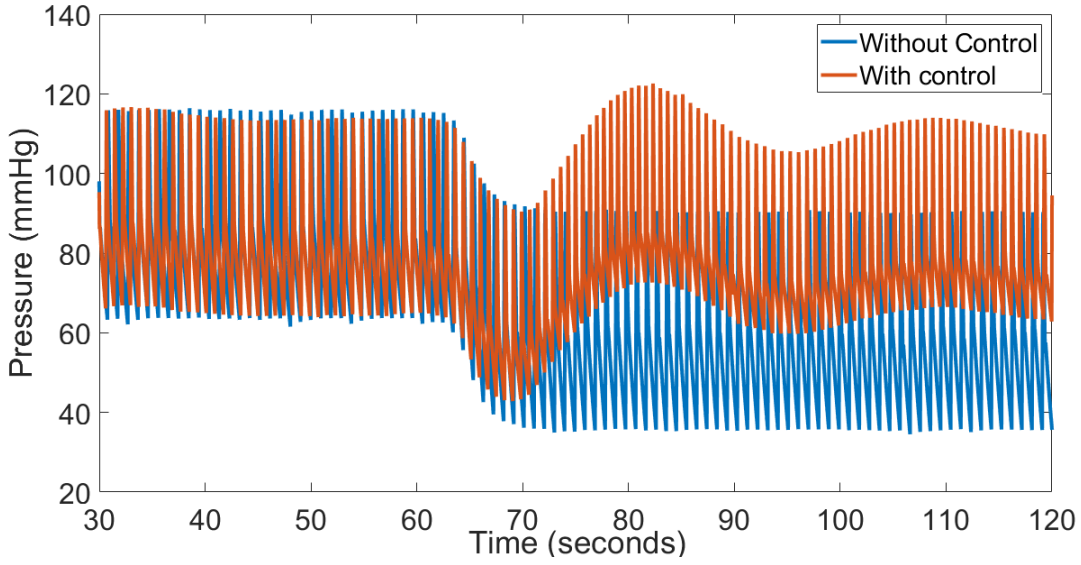

Figure 5.2: Arterial pressure with and without baroreflex control

5.4.2 Hemorrhage

A hemorrhage is a medical condition used to describe the escape of blood from the circulatory system. Hemorrhages can occur in various parts of the body and can vary in severity, ranging from minor, self-limiting to severe and life-threatening. The prognosis for a hemorrhage can vary widely, with minor hemorrhages often resolving on their own and severe hemorrhages requiring immediate medical attention. Timely intervention is crucial to manage and improve the outcome of a hemorrhage.

The FO model with baroreflex control is simulated for the hemorrhage condition by introducing 4%, 8%, 10% and 14% of blood loss in the veins. To understand the requirement of baroreflex control, 4% blood loss is introduced at time t=60 sec in the veins for FO model with/without baroreflex control. It is observed from Figure 5.3 that the pressure is dropped when the volume of blood is reduced from the nominal value. However, arterial pressure is back to steady state value due to baroreflex control. In order to show the limitations of the baroreflex control, the model is simulated for 4%, 8%, 10% and 14% of blood loss. It is noted that till 10% of blood loss, the controller is able to bring back the arterial pressure to the nominal value and beyond this the controller is failed to make appropriate decisions as shown in Figure 5.4.

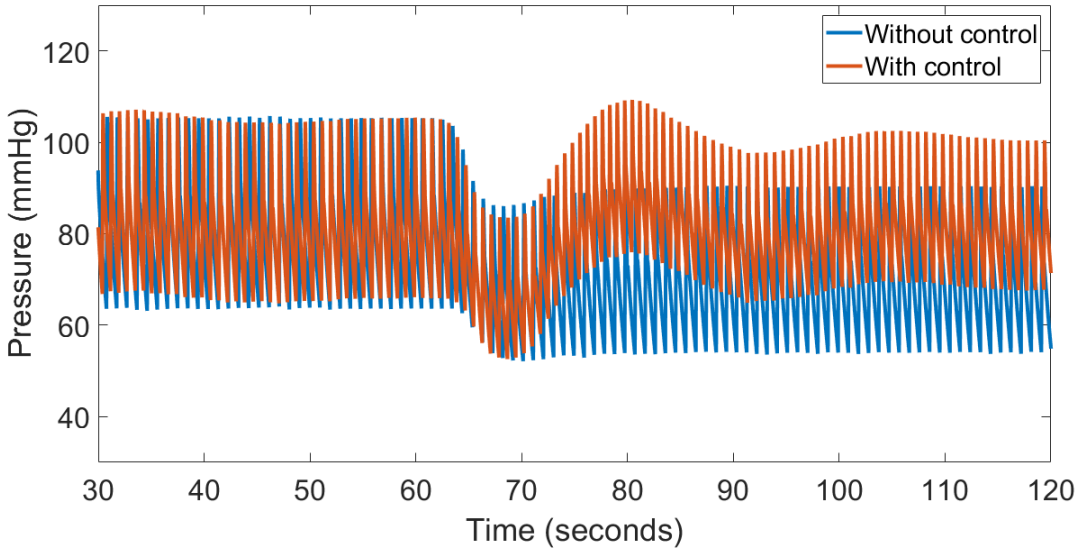

Figure 5.3: Responses of arterial blood pressure with/without baroreflex control under 4% blood loss introduced at time t=60 sec

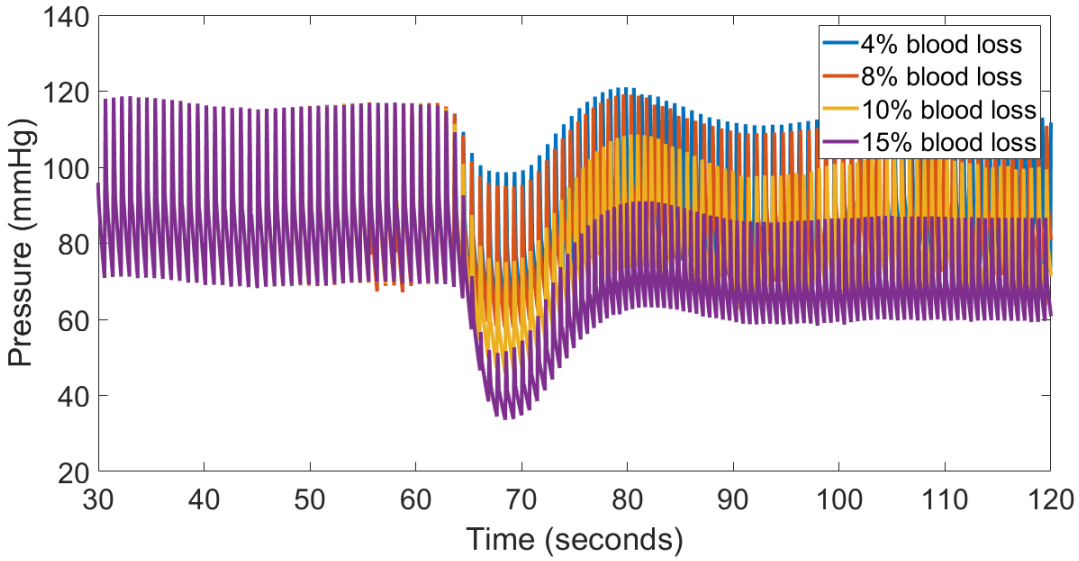

Figure 5.4: Responses of arterial blood pressure with baroreflex control under 4% , 8%, 10% and 14% of blood loss introduced at time t=60 sec

5.4.3 Orthostatic intolerance

OI refers to a medical condition where the HR cannot be controlled by poor baroreflex efferent innervation of the heart. This is observed commonly in the elderly and astronauts.

This is modeled by changing the baroreflex parameter which in turn loses the ability to make the pressure to nominal value. Figure 5.5 shows the simulated results for the effect of orthostatic hypotension condition on MAP. At t=60 sec, a postural change from supine to standing is introduced along with reduced sympathetic gain. Due to the abnormalities in the vascular baroreceptors which happen due to postflight, age, local tumor growth etc., the MAP and HR cannot attain its steady state value which leads to orthostatic hypotension condition as shown in Figure 5.5.

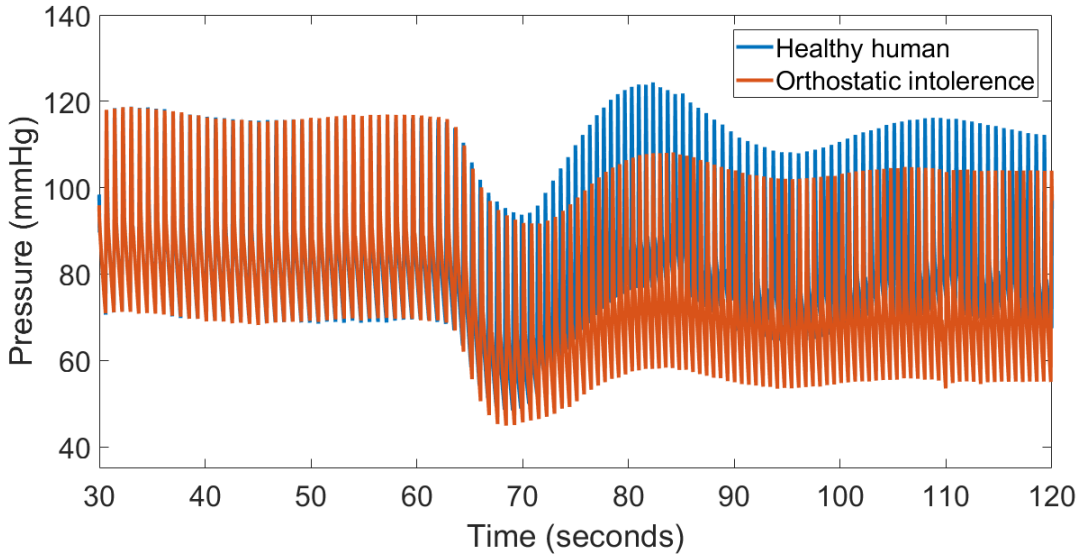

Figure 5.5: Response of arterial pressure with OI at t=60 sec and healthy condition for FO geometric model with baroreflex control

5.4.4 Atherosclerosis and arterial stiffness

Atherosclerosis is a chronic and progressive cardiovascular disease characterized by the accumulation of fatty deposits, cholesterol and other substances in the walls of arteries, forming plaques. These plaques can lead to arterial narrowing and stiffening, reducing blood flow and increasing the risk of various cardiovascular complications. Arterial stiffness refers to the reduced ability of arteries to expand and contract in response to changes in blood pressure. It is a common consequence of aging but can also be exacerbated by various risk factors and diseases. The model is further studied for atherosclerosis and arterial stiffness conditions and the corresponding pressure waveforms are shown in Figure 5.6. From the response, it is noted that these diseases introduce an increase in arterial pressure from the nominal value which needs further attention by medical practitioners.

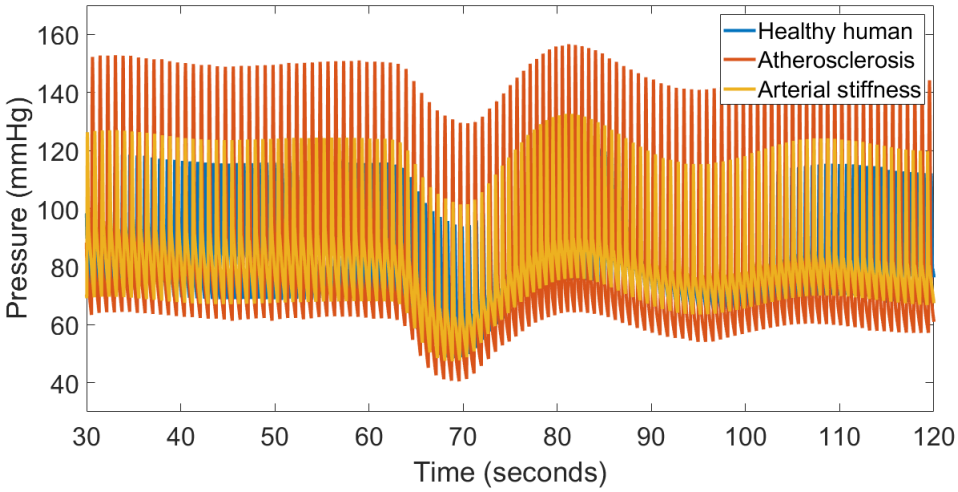

Figure 5.6: Responses of arterial blood pressure with abnormalities and healthy condition FO geometric model with baroreflex control

5.5 Summary

A baroreflex control for FO geometric model is proposed to study the effect of postural changes. It is essential to have an accurate model to study the complex interaction of baroreflex control. Hence a baroreflex control is designed for the FO geometric model. The simulation is carried out for postural change and it is observed that the pressure is coming back to the nominal value after some time with baroreflex control. The model with control is simulated for orthostatic condition by changing the baroreflex gain. The model is studied for hemorrhage conditions in which simulations are carried out for 4%, 8%, 10% and 14% of blood loss and it is observed that above 10% blood loss, the baroreflex fails to bring the pressure back to normal value. Further, abnormalities like arterial stiffness and atherosclerosis are introduced to the model and the results are analyzed.

Chapter 6

Conclusions and Future Scope

A mathematical model of CVS along with the baroreflex control was modeled to study the complex interactions between ANS and CVS for healthy and abnormal conditions. For initial simulation, only lumped IO Windkessel models were considered. To improve the accuracy, the viscoelasticity property was enhanced by introducing FO derivative in the existing 2-element, 3-element and 4-element Windkessel models in which the fractionality of the governing differential equation was obtained using optimization method by minimizing the error between the clinical data and the model output considered as an objective function. The simulation results indicated that FO models provide the least error index than the existing IO Windkessel models. In specific, the FO Wk4 model provided better closeness to the clinical data than other FO Windkessel models. Hence, FO Wk4 model was further used to study the behavior of abnormalities like atherosclerosis and arterial stiffness.

Further, FO modeling was extended to a more complex geometric model which addresses the limitations of Windkessel model by including four chambers of heart, systemic and pulmonary circulation. The heart chambers were modeled based on the geometry and systemic and pulmonary circulation were modeled using Windkessel approach. A constrained optimization problem was framed to obtain the fractionality of the dynamic equation by minimizing the pressure error between FO geometric model and clinical data of healthy human using heuristic methods such as CS, FA and APSO algorithms and the results are compared with conventional SQP algorithm. From the results, it was concluded that FO geometric model provided better accuracy than IO models. Further, FO geometric models were used to demonstrate abnormalities like arterial stiffness and atherosclerosis.

Baroreflex control for CVS was essential for maintaining cardiovascular homeostasis. This ensures efficient blood pressure regulation, optimal perfusion and adaptation to physiological demands. Initially, a baroreflex control was designed for the extended IO Windkessel model and simulated for postural change by modeling afferent, ANS and efferent

dynamics. To show the efficiency of the proposed model, the simulation was carried out further for orthostatic hypotension and hypertension conditions. In order to get a better model which mimics the CVS, a baroreflex control was designed for the proposed FO geometric model and validated for postural changes. Also, the proposed model is studied for different abnormality conditions like orthostatic intolerance, hemorrhage, atherosclerosis and arterial stiffness.

The future directions of the research work carried out in this thesis are as follows:

- The present model do not include the modeling of heart-lung interaction and gas exchange which is one of the important factors. Hence it is necessary to incorporate the effect of chemoreceptor to get a better model
- This proposed baroreflex did not consider the effects of change in gravity as a function of height and time during space travel including environmental effects. The absence introduced can be compensated by designing a baroreflex control which includes the effect of gravity and variation in parameters with respect to time
- The interaction between CVS and other organs like lungs, kidneys, liver, etc., can be modeled and hence will improve the diagnosis/prediction capabilities
- The proposed approach can be extended to identify various diseased models which are further useful to classify diseases with its severity using artificial intelligence/machine learning techniques

Bibliography

[1] N. Stergiopulos, J. J. Meister, and N. Westerhof, "Evaluation of methods for estimation of total arterial compliance," *American Journal of Physiology-Heart and Circulatory Physiology*, vol. 268, no. 4, pp. H1540–H1548, 1995.

[2] N. Stergiopulos, B. E. Westerhof, and N. Westerhof, "Total arterial inertance as the fourth element of the windkessel model," *The American journal of physiology*, vol. 276, no. 1, pp. H81–H88, 1999.

[3] S. Bozkurt, "Mathematical modeling of cardiac function to evaluate clinical cases in adults and children," *PLoS ONE*, vol. 14, no. 10, pp. 1–20, 2019.

[4] X. S. Yang, *Nature-Inspired Metaheuristic Algorithms*. Luniver Press, 2008.

[5] L. J. Westerhof, N. and B. Westerhof, "The arterial windkessel," *Medical Biological Engineering and Computing*, vol. 47, p. 131–141, 2009.

[6] M. Snyder and V. Rideout, "Computer simulation studies of the venous circulation," *IEEE Transactions on Biomedical Engineering*, vol. BME-16, no. 4, pp. 325–334, 1969.

[7] R. Burattini and G. Gnudi, "Computer identification of models for the arterial tree input impedance: Comparison between two new simple models and first experimental results," *Medical and Biological Engineering and Computing*, vol. 20, pp. 134–144, 1982.

[8] B. Lambermont, P. Gérard, O. Detry, P. Kolh, P. Potty, J. Defraigne, V. D'Orio, and R. Marcelle, "Comparison between three- and four-element windkessel models to characterize vascular properties of pulmonary circulation," *Archives of Physiology and Biochemistry*, vol. 105, no. 7, pp. 625–632, 1997.

[9] P. Segers, E. R. Rietzschel, M. L. D. Buyzere, N. Stergiopulos, N. Westerhof, T. Bortel L. M. V., Gillebert, and P. R. Verdonck, "Three and four-element windkessel models: assessment of their fitting performance in a large cohort of healthy middle-aged individuals," *Proccedings of the Institution of Mechanical Engineers Part H, Journal of engineering in medicine*, vol. 224, pp. 417–428, 2008.

[10] A. M. Cook and J. G. Simes, "Simple heart model designed to demonstrate biological system simulation," *IEEE Transactions on biomedical engineering*, vol. 19, pp. 97–100, 1962.

[11] M. F. Snyder and V. C. Rideout, "Computer simulation studies of the venous circulation," *IEEE Transactions on Biomedical Engineering*, vol. 16, pp. 325–334, 1969.

[12] V. C. Rideout and M. F. Snyder, "Computer simulation study of the cardiovascular and related physiological systems," *Mathematics and Computers in Simulation*, vol. 16, pp. 26–34, 1974.

[13] K. Jain, A. Guha, and A. Patra, "A particle filter based framework for the prognosis of atherosclerosis via lumped cardiovascular modeling," *International Journal of Prognostics and Health Management*, vol. 10, pp. 9–13, 2019.

[14] Y. Wang, H. Sun, J. Wei, X. Liu, T. Liu, and Y. Fan, "A mathematical model of a human heart including the effects of heart contractility varying with heart rate changes," *Journal of Biomechanics*, vol. 75, pp. 129–137, 2018.

[15] F. Abboud, S. Geiger, and J. Shepherd, *The Cardiovascular System: Peripheral circulation and organ blood flow. Vol. III*. American Physiological Society, 1983.

[16] N. Solaro, M. Malacarne, M. Pagani, and D. Lucini, "Cardiac baroreflex, hrv, and statistics: an interdisciplinary approach in hypertension," *Frontiers in physiology*, vol. 10, p. 478, 2019.

[17] J. T. Ottesen and M. Danielsen, "Modeling ventricular contraction with heart rate changes," *Journal of theoretical biology*, vol. 222, no. 3, pp. 337–346, 2003.

[18] M. S. Olufsen, J. T. Ottesen, H. T. Tran, L. M. Ellwein, L. A. Lipsitz, and V. Novak, "Blood pressure and blood flow variation during postural change from sitting to standing: Model development and validation," *Journal of Applied Physiology*, vol. 99, no. 4, pp. 1523–1537, 2005.

[19] M. S. Olufsen, H. T. Tran, J. T. Ottesen, O. F. Human, E. Lim, G. S. H. Chan, S. Dokos, S. C. Ng, L. A. Latif, S. Vandenberghe, E. E. Benarroch, K. Sharma, and T. K. Bera, "A Cardiovascular Mathematical Model of Graded Head-Up Tilt A Cardiovascular Mathematical Model of Graded Head- Up Tilt," vol. 4, no. 4, pp. 299–311, 2004.

[20] J. T. Ottesen, "Modelling the dynamical baroreflex-feedback control," *Mathematical and Computer Modelling*, vol. 31, no. 4, pp. 167–173, 2000.

[21] J. Ottesen, "Modelling of the baroreflex-feedback mechanism with time-delay," *Journal of Mathematical Biology*, vol. 36, no. 1, pp. 41–63, 1997.

[22] M. S. Olufsen, H. T. Tran, J. T. Ottesen, L. A. Lipsitz, V. Novak, R. Benim, S. Joyner, E. Tweedy, C. Vogl, and A. Dixon, "Modeling baroreflex regulation of heart rate during orthostatic stress," *American Journal of Physiology - Regulatory Integrative and Comparative Physiology*, vol. 291, no. 5, pp. 1355–1368, 2006.

[23] K. D. Lau and C. A. Figueroa., "Simulation of short-term pressure regulation during the tilt test in a coupled 3d-0d closed-loop model of the circulation." *Biomechanics and modeling in mechanobiology*, vol. 14, pp. 915–929, 2015.

[24] A. S. Karavaev, Y. M. Ishbulatov, A. R. Kiselev, V. I. Ponomarenko, M. D. Prokhorov, S. A. Mironov, V. A. Shvartz, V. I. Gridnev, and B. P. Bezruchko, "Model of human cardiovascular system with a loop of autonomic regulation of the mean arterial pressure," *Journal of the American Society of Hypertension*, vol. 10, pp. 235–43, 2016.

[25] B. Matzuka, J. Mehlsen, H. Tran, and M. S. Olufsen, "Using kalman filtering to predict time-varying parameters in a model predicting baroreflex regulation during head-up tilt," *IEEE Transactions on Biomedical Engineering*, vol. 62, no. 8, pp. 1992–2000, 2015.

[26] K. Barrett, S. Barman, S. Boitano, and H. Brooks, *Ganong's Review of Medical Physiology*. McGraw-Hill Education, 2010.

[27] M. F. Taher, A. B. Cecchini, M. A. Allen, S. R. Gobran, R. C. Gorman, B. L. Guthrie, K. A. Lingenfelter, S. Y. Rabbany, P. M. Rolchigo, J. Melbin, and A. Noordergraaf, "Baroreceptor responses derived from a fundamental concept," *Annals of Biomedical Engineering*, vol. 16, no. 5, pp. 429–443, 1988.

[28] A. Silvani, G. Calandra-Buonaura, B. D. Johnson, N. Van Helmond, G. Barletta, A. G. Cecere, M. J. Joyner, and P. Cortelli, "Physiological mechanisms mediating the coupling between heart period and arterial pressure in response to postural changes in humans," *Frontiers in Physiology*, vol. 8, no. 163, 2017.

[29] S. Gilmore, J. Hart, J. Geddes, H. Olsen, C., J. Mehlsen, P. Gremaud, and M. S. Olufsen, "Classification of orthostatic intolerance through data analytics," *Medical and Biological engineering and computing*, vol. 59, pp. 621–632, 2021.

[30] F. J. Baisch and L. E. J. Beck, "Post-flight orthostatic intolerance," *Anthrorack on the Spacelab D2 Mission*, vol. 1191, pp. 45–48, 1997.

[31] B. J. Yates and I. A. Kerman, "Post-spaceflight orthostatic intolerance: Possible relationship to microgravity-induced plasticity in the vestibular system," *Brain Research Reviews*, vol. 28, no. 1-2, pp. 73–82, 1998.

[32] N. Wessel, A. Gapelyuk, J. Weiß, M. Schmidt, J. F. Kraemer, K. Berg, H. Malberg, H. Stepan, and J. Kurths, "Instantaneous cardiac baroreflex sensitivity: xbrs method quantifies heart rate blood pressure variability ratio at rest and during slow breathing," *Frontiers in Neuroscience*, vol. 14, p. 547, 2020.

[33] S. M. C. Lee, L. C. Ribeiro, S. S. Laurie, A. H. Feiveson, V. V. Kitov, I. S. Kofman, B. R. Macias, M. Rosenberg, I. V. Rukavishnikov, E. S. Tomilovskaya, J. J. Bloomberg, I. B. Kozlovskaya, M. F. Reschke, and M. B. Stenger, "Efficacy of gradient compression garments in the hours after long-duration spaceflight," *Frontiers in Physiology*, vol. 11, p. 784, 2020.

[34] Q. Fu, S. Shibata, J. L. Hastings, S. H. Platts, D. M. Hamilton, M. W. Bungo, M. B. Stenger, C. Ribeiro, B. Adams-Huet, and B. D. Levine, "Impact of Prolonged Spaceflight on Orthostatic Tolerance during Ambulation and Blood Pressure Profiles in Astronauts," *Circulation*, vol. 140, no. 9, pp. 729–738, 2019.

[35] M. D. Rienzo, P. Castiglioni, F. Iellamo, M. Volterrani, M. Pagani, G. Mancia, J. M. Karemaker, and G. Parati, "Dynamic adaptation of cardiac baroreflex sensitivity to prolonged exposure to microgravity: data from a 16-day spaceflight," *the American Physiological Society*, vol. 105, no. 5, pp. 1569–1575, 2008.

[36] O. Defterli, D. Baleanu, A. Jajarmi, S. S. Sajjadi, N. Alshaikh, and J. H. Asad, "Fractional treatment: An accelerated mass-spring system," *Fractional Treatment: An Accelerated Mass-Spring System*, vol. 74, p. 122, 2022.

[37] D. Baleanua, A. Jajarmi, H. Mohammadi, and S. Rezapour, "A new study on the mathematical modelling of human liver with caputo–fabrizio fractional derivative," *Chaos, Solitons and Fractals*, vol. 134, p. 10975, 2020.

[38] M. A. Bahloul, M. Benencase, Z. Belkhatir, and T.-M. Laleg Kirati, "Finite-time simultaneous estimation of aortic blood flow and differentiation order for fractional-order arterial windkessel model calibration," *IFAC-PapersOnLine*, vol. 54, no. 15, pp. 538–543, 2021.

[39] A.-J. Guel-Cortez and E.-j. Kim, "A fractional-order model of the cardiac function," in *13th Chaotic Modeling and Simulation International Conference*. Springer International Publishing, 2021, pp. 273–285.

[40] M. A. Bahloul and T.-M. Laleg Kirati, "Fractional-order modeling of the arterial compliance: An alternative surrogate measure of the arterial stiffness," *arXiv:2010.10058*, 2020.

[41] M. A. Bahloul and T. M. Laleg-Kirati, "Arterial viscoelastic model using lumped parameter circuit with fractional-order capacitor." IEEE, 2018, pp. 53–56.

[42] P. Perdikaris and G. E. Karniadakis, "Fractional-order viscoelasticity in one-dimensional blood flow models," *Annals of Biomedical Engineering*, vol. 42, pp. 1012–1023, 2014.

[43] M. A. Bahloul and T. M. Laleg-Kirati, "Three-element fractional-order viscoelastic arterial windkessel model," *40th Annual International Conference of the IEEE Engineering, in Medicine and Biology Society (EMBC), Honolulu, HI, USA*, pp. 5261–5266, 2018.

[44] S. Das, *Functional Fractional Calculus*. Berlin Heidelberg: Springer-Verlag, 2011.

[45] K. Diethelm, N. J. Ford, and A. D. Freed, "A predictor-corrector approach for the numerical solution of fractional differential equations," *Nonlinear Dynamics*, vol. 29, no. 1, pp. 3–22, 2002.

[46] J. Traver, C. Nuevo-Gallardo, I. Tejado, J. Fernández-Portales, J. Ortega-Morán, J. Pagador, and B. Vinagre, "Cardiovascular circulatory system and left carotid model: A fractional approach to disease modeling," *Fractal and Fractional*, vol. 6, no. 2, pp. 64–68, 2022.

[47] M. C. Tripathy, D. Mondal, K. Biswas, and S. Sen, "Experimental studies on realization of fractional inductors and fractional-order bandpass filters," *International Journal of Circuit Theory and Apploications*, vol. 43, no. 9, pp. 1183–1196, 2015.

[48] T. Sahu, K. Biswal, and M. Tripathy, "Time and frequency domain analysis of a fractional-order all-pass filter," *Advances in Intelligent Computing and Communication*, vol. 430, pp. 263–272, 2022.

[49] L. Majhi, M. Borah, and P. Roy, "Fractional order system identification of maglev model from real-time data," *IEEE International Conference on Advanced Communication Control and Computing Technologies (ICACCCT)*, pp. 210–213, 2014.

[50] R. Shalaby, M. El-Hossainy, and B. Abo-Zalam, "Fractional order modeling and control for under-actuated inverted pendulum," *Communications in Nonlinear Science and Numerical Simulation*, vol. 74, pp. 9–121, 2019.

[51] J. Abdelhamid, J. Khaled, M. Pierre, and J.-C. Trigeassou, "Fractional identification of rotor skin effect in induction machines," *International Journal of Electrical and Computer Engineering (IJECE)*, vol. 8, no. 1, pp. 57–68, 2011.

[52] P. Sathishkumar, "Fractional order controllers for complex valued systems and system with multiple nonlinearities," Ph.D. dissertation, Indian Institute of Space Science and Technology, Trivandrum, 2019.

[53] J. Kennedy, *Particle Swarm Optimization*. Boston, MA: Springer, 2011.

[54] A. Tsipianitis and Y. Tsompanakis, "Improved cuckoo search algorithmic variants for constrained nonlinear optimization," *Advances in Engineering Software*, vol. 149, p. 102865, 2020.

[55] J.-Y. Cao, J. Liang, and B.-G. Cao, "Optimization of fractional order pid controllers based on genetic algorithms," vol. 9. IEEE, 2005, pp. 5686–5689.

[56] M. Danielsen and J. T. Ottesen, "Describing the pumping heart as a pressure source," *Journal of Theoretical Biology*, vol. 212, no. 1, pp. 71–81, 2001.

[57] M. S. Olufsen, A. Nadim, and L. A. Lipsitz, "Dynamics of cerebral blood flow regulation explained using a lumped parameter model." *American journal of physiology. Regulatory, integrative, and comparative physiology*, vol. 282, no. 2, p. R611–R622, 2002.

[58] M. Olufsen and A. Nadim, "On deriving lumped models for blood flow and pressure in the systemic arteries," *Mathematical Biosciences and Engineering*, vol. 1, no. 1, pp. 61–80, 2004.

[59] E. Lim, G. S. H. Chan, S. Dokos, N. S. C, L. A. Latif, and S. Vandenberghe, "A Cardiovascular Mathematical Model of Graded Head-Up Tilt A Cardiovascular Mathematical Model of Graded Head- Up Tilt," vol. 8, no. 10, pp. 1–12, 2013.

[60] L. S. Goldoozian and E. Zahedi, "Mathematical modeling of heart rate and blood pressure variations due to changes in breathing pattern," *20th Iranian Conference on Biomedical Engineering (ICBME)*, pp. 54–58, 2013.

[61] A. Mahdi, J. Sturdy, J. T. Ottesen, and M. S. Olufsen, "Modeling the afferent dynamics of the baroreflex control system," *PLoS Computational Biology*, vol. 9, p. 12, 2013.

[62] A. Loverro, "Fractional calculus: History, definitions and applications for the engineer," Department of Aerospace and Mechanical Engineering, University of Notre Dame, Tech. Rep., 2004.

[63] B. Ross, "A brief history and exposition of the fundamental theory of fractional calculus." Springer, 1975.

[64] I. Podlubny, *An introduction to fractional derivatives, fractional differential equations, to methods of their solution and some of their applications*. San Diego: Academic Press, Inc., 1999.

[65] B. M. Vinagre, C. A. Monje, and A. J. Calderon, "Fractional order systems and fractional order control actions," *IEEE Conference on Decision and Control*, pp. 2550–2554, 2002.

[66] D. Xue, C. Zhao, and Y. Q. Chen, "Fractional order pid control of a dc motor with elastic shaft: a case study," *proceedings of IEEE American control conference*, vol. 7, pp. 3182–3187, 2006.

[67] B. Moody, G. Moody, M. Villarroel, G. D. Clifford, and I. Silva, "Mimic-iii waveform database (version 1.0), physionet."

[68] X. S. Yang and S. Deb, "Cuckoo search via lévy flights," *World Congress on Nature and Biologically Inspired Computing (NaBIC)*, pp. 210–214, 2009.

[69] J. Kennedy and R. Eberhart, "Particle swarm optimization," *International Conference on Neural Networks*, vol. 4, pp. 1942–1948, 1995.

[70] D. S. Yang, X. S. and S. Fong, "Accelerated particle swarm optimization and support vector machine for business optimization and applications, in: Networked digital technologies," *Communications in Computer and Information Science Springer*, vol. 136, pp. 53–66, 2011.

[71] J. P. Murgo, N. Westerhof, J. P. Giolma, and S. Altobelli, "Aortic input impedance in normal man: relationship to pressure wave forms," *Circulation*, vol. 62, pp. 105–116, 1980.

[72] M. Ursino, "Interaction between carotid baroregulation and the pulsating heart: a mathematical model," *American Journal of Physiology-Heart and Circulatory Physiology*, vol. 275, no. 5, pp. H1733–H1747, 1998.

List of Publications

Papers in Refereed International Journals

1. V. L Resmi, R. G Sriya and N. Selvaganesan, "Baroreflex control model for cardiovascular system subjected to postural changes under normal and orthostatic conditions", Computer Methods in Biomechanics and Biomedical Engineering, 26(9), 1034-1043, 2023.

2. V. L Resmi and N. Selvaganesan, "Fractional order model for cardiovascular system using heuristic optimization approach", Journal of Mechanics in Medicine and Biology, May 2023, https://doi.org/10.1142/S0219519423500811.

3. V. L Resmi and N. Selvaganesan, "A Study on Fractional Order Arterial Windkessel Model using Optimization Method", IETE Journal of Education, May 2023, https://doi.org/10.1080/09747338.2023.2210093.

Journal Papers Submitted

1. V. L Resmi and N. Selvaganesan, “Baroreflex Control Design for Fractional Order Cardiovascular System Under Postural Change and Diseased Conditions”, IEEE Journal of Transalational Engineering in Health and Medicine.